Screen Printing and Rheology of Pastes

zur Erlangung des akademischen Grades eines
DOKTORS DER INGENIEURWISSENSCHAFTEN (Dr.-Ing.)

von der KIT-Fakultät für Chemieingenieurwesen und Verfahrenstechnik des
Karlsruher Instituts für Technologie (KIT)
genehmigte

DISSERTATION

von
M.sc. Chenhui Xu
aus Anhui, China

Erstgutachter:	Prof. Dr. Norbert Willenbacher
Zweitgutachter:	Prof. Dr. Gunter Hübner
Tag der mündlichen Prüfung:	28.09.2018

Acknowledgement

Here I would like to thank my supervisor Prof. Dr. Norbert Willenbacher for helping me with advice, not only for the challenging research topic but also for life.

Many thanks to Prof. Dr.-Ing. Gunter Hübner for being the second reviewer of this thesis and valuable comment for the work.

Thanks for the discussion with Ceren Yüce about the research topic and also thanks Annika Völp for supporting me as my lovely officemate. A lot of discussions also took place during the lunch with lovely colleagues, Dr. Claude Oelschlaeger, Dr. Johannes Maurath, Dr. Hongye Sun, Frank Bossler, Moritz Weiss, Ronald Gordon, Walter Oswald, David Menne. Many thanks to them for offering me a lot of happy and encouraging me when I was in a depressed mood. A lot of thanks also to the other colleagues.

Further, I would like to thank BASF SE for offering the opportunity to work within an industrial project. I appreciate the support from Dr. Xuerong Gao, Dr. Markus Fiess and Dr. Herve Dietsch. Many thanks to Michael Machate and Marco Czink and other colleagues for the support in working and living in Germany.

The last but not the least, I would like to thank my wife Yudi Wang and my family for their support and encourage to finish my Ph.D. work.

Abstract

Screen printing is one of the most prominent printing processes with its well-known application in classical fields, e.g., poster or textile printing, but also in all kinds of printed electronic devices. The focus of this thesis is on fine line screen printing in the emerging field of photovoltaics. Essentially all solar cells produced today are contacted using screen printing technology. In this process, silver pastes are used. For reduction of silver consumption together with an increase in solar cell efficiency are a perpetual challenge.

The paste rheological properties are essential for fine line screen printing process. Printing of narrow electrodes with higher aspect ratio challenges the formulation of appropriate pastes. This thesis focuses on the relevance of paste rheology in the screen printing process.

In the first part, the wall slip behavior and rheology of silver pastes, typically used for front-side metallization of Si solar cells is discussed, as well as its impact on printing behavior and cell efficiency. The onset of slip, slip velocity on steel and on capillary film have been determined using rotational rheometry. In both cases, slip velocity v increases linearly with applied stress σ. Its absolute value, the slope v/σ , and the slip layer thickness δ_{slip} vary in a wide range, depending on paste composition. Silver deposit, residual silver on the screen, the geometry of the printed electrodes, and the connections between busbar and fingers have been examined using gravimetric methods and optical microscopy. The silver deposit systematically increases, and accordingly, the residual silver on the screen decreases with increasing slip velocity. The busbar/finger connection area narrows, whereas height and cross-sectional area of the electrodes increase with slip velocity. However, electrode width seems to be related to the pastes' yield stress. Mass deposit, the shape of the busbar/finger connection, and electrode geometry are supposed to have an important impact on cell electrical parameters, e.g., short-circuit current and fill factor. Accordingly, our results suggest that the slip behavior of the paste affects the overall cell efficiency.

The second part of this study focuses on the paste transfer process during screen printing. Based on high-speed video imaging experiment, the rheological parameters relevant to different process steps are discussed. ZnO pastes were used as a model system. These pastes included ethyl cellulose or Thixatrol Max as additive introducing different physical mechanisms of structure and flow control. Yield stress, viscosity and its recovery after high shear were obtained using rotational rheometry. Filament break-up was determined in uniaxial elongational tests. Pastes were printed using a commercial screen designed for Si-solar cell front-side metallization and the process was monitored with high temporal and spatial resolution using a transparent glass substrate and a high-speed imaging set-up. Length of the pre-injection zone ahead of the squeegee scales inversely with yield stress and length of the cling zone behind the squeegee is proportional to filament fracture strain, irrespective of the used additive. Paste spreading observable at the busbar and fine line intersection takes place within 100 ms, irrespective of sample composition, demonstrating that fine line electrode width is determined within the pre-injection zone where the paste is under pressure. A simple flow model is proposed relating electrode width to the reciprocal product of yield stress and high shear viscosity consistent with experimental data including both types of pastes.

Zusammenfassung

Siebdruck ist einer der bekanntesten Druckverfahren mit seiner bekannten Anwendung in klassischen Gebieten, z. B. Plakat- oder Textildruck, aber auch in allen Arten von gedruckten elektronischen Vorrichtungen. Der Schwerpunkt dieser Arbeit liegt auf dem Feinliniensiebdruck in der Photovoltaikindustrie. Im Wesentlichen werden alle heute produzierten Solarzellen im Siebdruckverfahren kontaktiert.Bei diesem Verfahren werden Silberpasten verwendet. Die Reduzierung des Silberverbrauchs und die Steigerung der Solarzelleneffizienz sind eine ständige Herausforderung.

Die rheologischen Eigenschaften der Paste sind essentiell für den Siebdruck in feinen Linien. Das Drucken schmaler Elektroden mit einem höheren Seitenverhältnis stellt die Formulierung geeigneter Pasten in Frage. Diese Arbeit konzentriert sich auf die Relevanz der Pastenrheologie im Siebdruckprozess.

Im ersten Teil wird das Wandschlupfverhalten und die Rheologie von Silberpasten, die typischerweise für die Vorderseitenmetallisierung von Si-Solarzellen verwendet werden, sowie deren Einfluss auf das Druckverhalten und die Zelleffizienz diskutiert. Der Beginn des Schlupfes, die Gleitgeschwindigkeit auf Stahl und auf dem Kapillarfilm wurden unter Verwendung der Rotationsrheometrie bestimmt. In beiden Fällen steigt die Gleitgeschwindigkeit v linear mit der angelegten Spannung σ. Sein absoluter Wert, die Steigung v/σ und die Gleitschichtdicke δ_{slip} variieren in einem weiten Bereich, abhängig von der Pastenzusammensetzung. Silberablagerungen, Restsilber auf dem Sieb, die Geometrie der gedruckten Elektroden und die Verbindungen zwischen Stromschiene und Fingern wurden mit gravimetrischen Methoden und optischer Mikroskopie untersucht. Die Silberablagerung nimmt systematisch zu und dementsprechend nimmt das Restsilber auf dem Sieb mit zunehmender Rutschgeschwindigkeit ab. Die Busbar-/Fingerverbindungsfläche verengt sich, während die Höhe und die Querschnittsfläche der Elektroden mit der Rutschgeschwindigkeit zunehmen. Die Elektrodenbreite scheint jedoch mit der Fließspannung der Pasten in Beziehung zu stehen. Massenablagerung, die Form der Busbar-/Fingerverbindung und die Elektrodengeometrie sollen einen wichtigen Einfluss auf die elektrischen Parameter der Zelle haben, z. B. den Kurzschlussstrom und den Füllfaktor. Dementsprechend legen unsere Ergebnisse nahe, dass das Gleitverhalten der Paste die Gesamtzellwirksamkeit beeinflusst.

Der zweite Teil dieser Studie konzentriert sich auf den Pastentransferprozess beim Siebdruck. Basierend auf einem Hochgeschwindigkeits-Video-Imaging-Experiment werden die fü die verschiedenen Prozessschritte relevanten rheologischen Parameter diskutiert. ZnO-Pasten wurden als Modellsystem verwendet. Diese Pasten enthielten Ethylcellulose oder Thixatrol Max als Additiv, das verschiedene physikalische Mechanismen der Struktur- und Fließkontrolle einführte. Fließgerenze, Viskosität und seine Rückstellung nach hoher Scherung wurden unter Verwendung der Rotationsrheometrie erhalten. Die Zerlegung der Fasern wurde in uniaxialen Dehnungstests bestimmt. Die Pasten wurden unter Verwendung eines kommerziellen Schirms gedruckt, der für die Vorderseitenmetallisierung der Si-Solarzelle ausgelegt war, und der Prozess wurde mit hoher zeitlicher und räumlicher Auflösung unter Verwendung eines transparenten Glassubstrats und eines Hochgeschwindigkeits-Bildgebungsaufbaus überwacht. Die Länge der Pre-injectionzone vor den Abstreifleisten ist umgekehrt proportional zur Fließgerenze und der Länge der Clingzone hinter der Abstreifleiste ist proportional zur Filamentbruchdehnung, unabhängig vom verwendeten Additiv. Pastenausbreitungs-Observable an der Busbar und Feinlinienkreuzung findet innerhalb von 100 ms statt, unabhängig von der Probenzusammensetzung, was zeigt, dass die feine Linienelektrodenbreite innerhalb der Pre-injectionzone bestimmt ist, wo die Paste unter Druck steht. Es wird ein einfaches Strömungsmodell vorgeschlagen, das die Elektrodenbreite mit dem reziproken Produkt aus Fließgerenze und hoher Scherviskosität in Übereinstimmung bringt, übereinstimmend mit experimentellen Daten, die beide Arten von Pasten einschließen.

Contents

List of symbols

EOM	Emulsion Over Mesh	
EC	Ethyl Cellulose	
T-Max	Thixatrol Max	
3ITT	Three Intervals Thixotropic Test	
PCB	Printed Circuit Board	
FPCB	Flexible Printed Circuit Board	
CLSM	Confocal Laser Scanning Microscopy	
α	printing angle	$\circ$
γ	strain	-
$\dot{\gamma}$	shear rate	s^{-1}
δ	phase angle shift	$\circ$
σ	shear force	Pa
σ_y	apparent yield stress	Pa
τ	time constant in 3ITT	s
η	viscosity	$Pa \cdot s$
w	line width	μm
w_s	shaded line width	μm
w_c	conductive line width	μm
t	time	s
ρ	density	g/cm^3
ϕ	volume fraction	%
d	diameter	mm
G	modulus	Pa
h	height	mm
M_w	molecular weight	kg/mol
n	rotation speed	$1/min$
rpm	rounds per minute	$1/min$
v	velocity	mm/s

Chapter 1

Introduction

1.1 Background and motivation

Electronic devices are involved in our daily life ranging from the circuit board in our cellphone to the sensors in the cars or airplanes. Printing, compared with other techniques [1], e.g., physical vapor deposition or photolithography, is inexpensive and efficient due to its smooth transition to large-scale production. The printable electronics market is increasing rapidly with the potential to acheive $70 billion in the next ten years from $29.28 billion reported in 2017 [2].

Various kinds of printing techniques, i.e., screen printing, stencil printing, inkjet printing, dispensing, flexography printing, etc., have been tried, demonstrated or already used to fabricate electronic devices. Screen printing is the method in which the paste or ink is pushed through a partially open stencil, which is formed by a polymer film that is supported by a woven mesh. Stencil printing is the method in which the paste or ink is forced through a metal mask with openings. Inkjet printing is the method in which the ink is deposited on the substrate as micro-sized droplets for fine structure. Dispensing is the method in which the ink or paste is pushed through a nozzle, and the relative movement between nozzle and substrate determines the pattern. In the flexography printing, an anilox roller accepts the ink from a chambered doctor blade and then transfers it to the elevated parts of the printing form. From there it is directly transferred to the substrate

Ink or paste formulations have to meet several requirements, especially rheological specifications, depending on different kinds of printing techniques in the application process. For example, inkjet printing requires low viscosity formulations (0.001 - 0.04 $Pa \cdot s$) while highly viscous formulations are required for screen printing (0.5 - 50 $Pa \cdot s$) [3, 4]. Even for the same technology, different applications demand different rheological properties, e.g., the realized viscosity is lower in thick film screen printing than in fine finger screen printing. Polymer binders provide the cohesion of the printed film and the adhesion force to the substrate after drying, e.g.

ethyl cellulose in screen printable ink. Meanwhile the added polymer binders also adjust the flow behavior of the formulations in the application process. Sometime, the additives could be also inorganic materials, e.g. pyrogen silica as the thickener in ink formulations. Furthermore, the formulations include some other components to avoid sedimentation or agglomeration during storage.

Due to its low cost, high time efficiency and possiblity to achieve high layer thickness, screen printing is the dominating method in some fine line printing applications, e.g., front-side metallization of silicon solar cells [5], It is also a potential alternative to fine finger photolithography in some cases, e.g., microcircuit manufacturing on flexible printed circuit board (FPCB). For fine finger application, the geometry of printed electrode is more sensitive to paste rheological properties compared to thick film screen printing.

Screen printing has been developed for centuries since its prototype, silk printing. Some theoretical analysis has been promoted to relate the screen printing process and flow behavior of pastes since decades [6–8]. Different rheological properties, which influence the printing, are discussed, and some general conclusions are given: higher viscosity reduces the paste spreading during printing, resulting in narrower electrodes; faster recovery after the cessation of high shear, avoids further spreading [9, 10]; higher yield stress also leads to narrower printed electrode width [11].

However, there are also other phenomena during the screen printing process, which remain unexplained. As highly concentrated suspensions, screen printable pastes show wall slip between the sample and adjacent surface of the mesh fabric as well as the walls of the stencil. Although its influence on stencil printing is well known [12, 13], there is no systematic research for wall slip with respect to the screen printing process. The wall slip effect is discussed scientifically and systematically in this study for the first time although the industry has observed the hint for such kind of phenomena [14].

Wetting and flow phenomena potentially occurring during the printing process have been hypothesized based on the analysis of the final printed patterns [15]. However, due to the fast printing speed and the limit of the opaque substrates, there is no direct and real-time observation of the screen printing process so far. In this study, a high-speed camera was inserted into a screen printer. For the first time, the screen printing process has been directly observed with high spatial and temporal resolution through a glass plate. This work fills the gap of direct observation and provides new information relating paste properties, printing parameters and printed structure specifications paving the way for fidgeted development as well as future research.

1.2 Outline of this work

After the brief introduction, given above in section 1.1, this thesis contains the following chapters:

In **chapter 2**, some background about the screen printable pastes and rheological properties will be introduced. It includes an overview of different kinds of printed electrodes, especially the front side metallization of silicon solar cells. The screen printing process is also explained briefly in this chapter. The components in different kinds of screen printed pastes are introduced. Finally, rheological properties of screen printable pastes influenced by the ingredients in the formulations are summarized.

In **chapter 3**, the materials used in this thesis are summarized. There are two kinds of model systems included in this thesis. One is the traditional silver-based paste, which is close to the commercial products for the front side metallization of Si-solar cells. The silver system is used to investigate the influence of wall slip on fine line screen printing. The other one is ZnO-based paste. In this system, type and concentration of rheological controlling agent is varied, resulting in huge variation in the rheological properties. The formulations and preparation procedures are also discussed in detail in this chapter.

Chapter 4 introduces the rheological methods used to characterize the pastes. The new experiment setup used for the high-speed monitoring of the screen printing process is also introduced in this part.

In **chapter 5**, the results of the two series of printing experiments based on different types of pastes are summarized and discussed. The influence of wall slip is discussed. The high-speed camera video gives a clear picture of what happens during the screen printing process. The printed electrode width seems to be controlled by the yield stress and high shear viscosity of respective pastes and a simple model relating line width and rheological quantities is generated based on the video imaging results.

A final discussion and some outlook regarding the screen printing technology and future research that may be stimulated by the work presented here, are given in **chapter 6** and **chapter 7**, respectively.

Chapter 2

State of the art and literature review

2.1 Printed electronics

Different kinds of printing methods, as listed in Chapter 1, can be used to produce different kinds of electrical devices. This is called printed electronics.

Different kinds of electronic devices or part of the devices are manufactured with printing techniques, e.g., front- and rear-contact for solar cell, varistor, conductive electrodes in low/high temperature co-fired ceramics (LTCC/HTCC), (organic) thin film transistors, the conductive circuit in a touch panel, different kinds of sensors, solder joint in printed circuit board (PCB), antennae, electrochromic and electroluminescense, etc.

The shapes of the printed object can be one dimensional, e.g., fine line electrodes for different devices, two dimensional, e.g., ZnO film in varistors, electrodes in solid oxide fuel cells, or three dimensional, e.g., 3D printed structures.

The substrates for the printed object can be metal, e.g., direct copper bonding substrates for power electronics, semiconductor, e.g., the silicon wafer for solar cells, ceramics, e.g., ceramic body in LTCC, plastic, e.g., epoxy for PCB, PET for printed antennae or for sensors.

The printed materials can be organic materials, e.g., adhesives for various devices, different layers (PEDOT:PSS, etc) in organic solar cells, or inorganic materials, e.g., silver, carbon black for electrodes, ZnO for varistor. The formulation usually is ink or paste-like materials.

2.1.1 Fine line electrodes

The miniaturization of the electronic devices demands finer printed patterns for higher device density. For instance, modern smart-phones chase higher screen-to-body ratio [16], requiring finer electrodes at the edge of the display screen. Meanwhile, the chasing of thinner phone body limits the space of PCB although it is more and more complicated. Narrower printed electrodes reduce the shaded area on front-side of silicon solar cells, resulting in higher efficiency [17]. The high-frequency application requires finer printed electrodes in HTCC/LTCC.

Due to its low cost and high throughput, screen printing is an essential step for electrode fabrication in many electronic devices. The printing quality and accurateness have been improved in the last several decades, mainly due to the requirement from finer front-side electrodes in silicon solar cell, which will be introduced in the next section. With the improvement, fine line screen printing nowadays is able to print the current collector fingers on the front side of a Si-solar cell around or even less than 35 μm.

2.1.2 Front-side electrodes for silicon-based solar cells

A solar cell is an electronic device which converts the sunlight into electricity. The classical structure for a silicon-based solar cell is illustrated in Fig. 2.1 [18]. The material (p-doped silicon in Fig. 2.1) absorbs the sunlight and generates electron-hole pairs. Then the electrons go out into the external circuit, release the energy and return to the base.

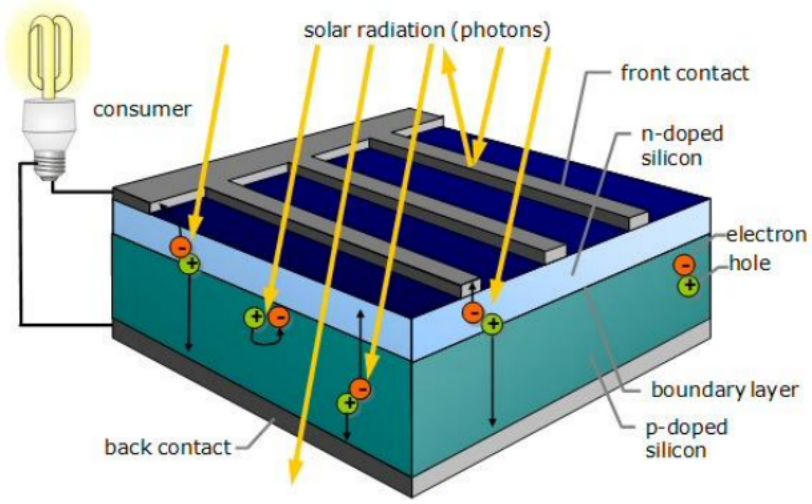

Figure 2.1: Schematic diagram of a silicon solar cell structure.

In this process, the energy released to the external circuit depends on the number of photons entering the base, which is proportional to the area under the light. Therefore, it is crucial to reduce the shaded area covered by the front contact. The rear and front contacts are commonly metallized by screen printing with aluminum and silver pastes, respectively. $A_{met,grid}$, the ratio of the area covered by the front-side metal grid and the total surface area, is used to quantify the rate of grid shading loss. To achieve smaller $A_{met,grid}$, narrower (< 30 μm) front-side silver electrodes are chased [19].

However, only reducing the finger width is not sufficient to increase cell efficiency. A large cross-sectional area is required to maintain an excellent conductivity [20].

To achieve optimized shape, the rheological properties of the formulations should be optimized [9]. Meanwhile, other innovative methods are also suggested, such as double screen printing [19].

2.2 Screen printing process

In this section, some engineering background about screen printing will be introduced, including the screen parameters, the printing cycle, the squeegee and other parameter settings in screen printing.

2.2.1 Screen

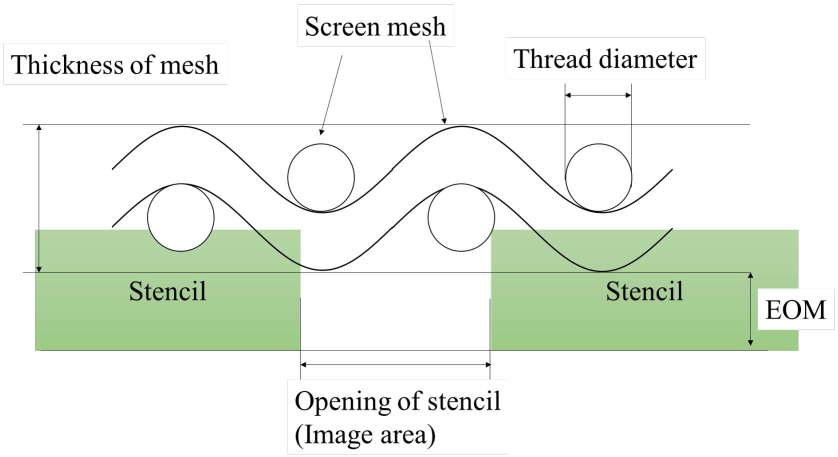

Figure 2.2: Schematic diagram of the screen.

The screen contains a woven mesh, made of stainless steel or Polyester (PET), and a polymer capillary film above the mesh (see Fig. 2.2). The woven mesh could also be Nylon or high performance Polyarylate. The screen mesh determines the tension, which should be suitable for the printing process. The emulsion or capillary film is coated onto the screen fabric and exposed to UV light with the pattern mask. The screen opening is formed by washing the uncured emulsion generally with water. The shape of the screen printed electrodes depends on the screen parameters, i.e. :

- **mesh number**, how many wires in one inch (2.54 cm);
- **wire diameter**, the diameter of the stainless steel or polyester wire;
- **thickness of mesh**. The thickness of mesh depends on the wire diameter and also manufacture method;
- **Emulsion over mesh(EOM)**, the height of the stencil above the mesh indicated in Fig 2.2. Both thickness of mesh and EOM determines the height of printed electrodes in the finer screen printing;
- **mesh tension**. It depends mainly on the forces applied during the stretching process. However, the limit of the tension value depends on on the material

(stainless steel has much higher modulus of elasticity than polymer threads) and on the specific cross section of the mesh, which is the cross section of the threads per cm;

- **opening of stencil**, which determines the printed electrode width mostly;
- **the angle between the woven mesh and opening** which is explained in Fig. 2.3.

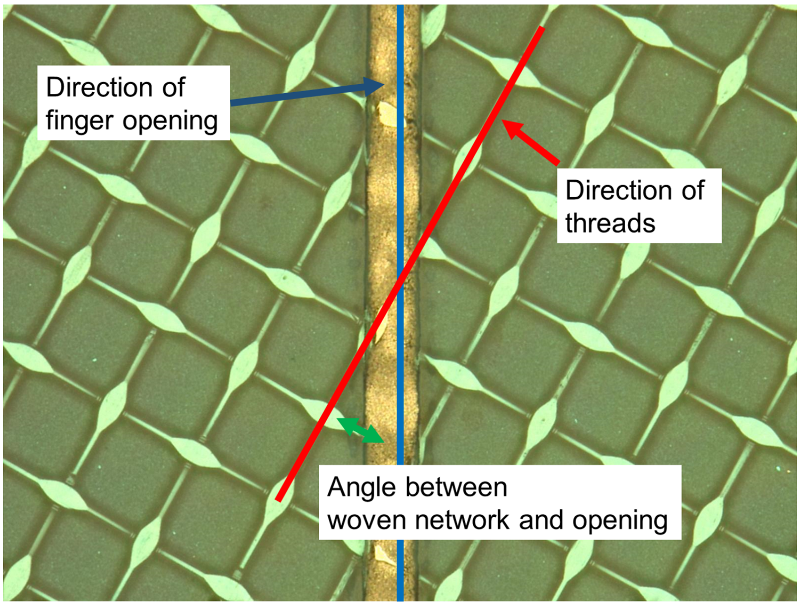

Figure 2.3: The angle between the woven mesh and line opening.

2.2.2 Print cycle

Normally the screen printing process contains two steps, i.e., flooding (F) and printing (P) , in a print cycle. There are also specific print cycles, e.g., FPP or FPFP, which will not be discussed here. In the printing process, the paste is pushed through the screen opening and in the flooding process, the paste is distributed on the screen for next print (see Fig. 2.4).

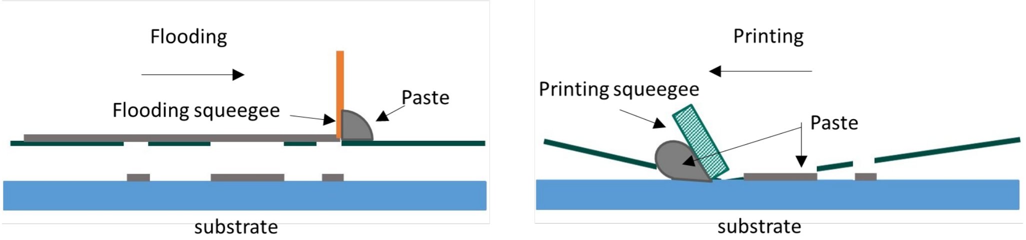

Figure 2.4: Schematic diagram of flooding (left) and printing (right) steps.

2.2.3 Squeegees

In the printing process, a rubber blade, so-called printing squeegee, pushes the screen onto the substrate, forces the paste through the screen opening, and also shears and removes the paste from the screen surface. The shape of the printed electrode also depends on the squeegee parameters, i.e.:

- **squeegee materials**. Some components in the paste, especially solvents, may react with the squeegee, making it softer and expanding, which has to be prevented;
- **squeegee hardness**. Squeegee hardness determines the deformation of the squeegee and screen under pressure during the printing process, which controls the shape of the printed electrodes significantly. The squeegee is with 75 under Shore A used in this study. The squeegee hardness also influences its lifetime. Normally, the softer squeegee exhibits a shorter lifetime under the same printing conditions;
- **the shape of squeegee edge**. Typically, the squeegee is with a right-angle edge. During printing, the screen wears the squeegee and forms a flat contact area between squeegee and screen, resulting in different printing quality [21]. For some special applications, an accurate edge is needed for a higher height of printed film.

In the flooding process, a piece of steel blade, so-called flooding squeegee, distributes the paste uniformly on the screen. The distance between the flooding squeegee and screen determines the paste thickness, which influences the shape of the printed electrodes, but not so significant as the other parameters, i.e., pressure, printing speed or angle between squeegee and screen.

2.2.4 Print parameters

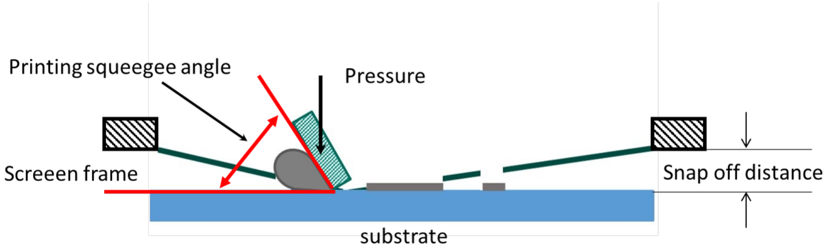

Figure 2.5: Schematic diagram of printing squeegee settings.

Except for the screen parameters, the printing parameters influence the shape of the printed electrodes, i.e.

- **printing speed**. Different printing speeds induce different shear stress profile in the paste roll [8], corresponding to different viscosity of the paste during printing. The state-of-art printing speed reaches $\sim 300\ mm/s$. Different printing speeds result in different squeegee deformation even at the same applied pressure;
- **flooding speed**. Flooding speed influences the paste film thickness above the

screen.

- **squeegee pressure** in force per unit length. The pressure and the squeegee hardness determine the deformation of the screen (see Fig. 2.5). With too low pressure, the squeegee cannot push the paste through the screen opening, resulting in a nonuniform printed electrode or a kind of aquaplanning effect on the substrate. With too high pressure, the height or thickness of printed layer is decreased, and the possibility of paste bleeding is increased.
- **snap-off distance**. The “snap-off" is the word, describing the noise when the screen lifts up from the substrate behind the printing squeegee in the process. The distance or the "printing gap" between the screen and substrate influences printing performance (see Fig. 2.5). Too high or low snap-off reduce the screen lifetime and is not beneficial for designed printing feature. Therefore, the snap-off influences the shape of the printed electrodes, which is essential for the electronic properties, and also the screen lifetime, which is significant from an engineering point of view.
- **printing squeegee angle**. The angle between the squeegee and substrate determines the vertical forces from the squeegee to paste through the screen opening, which influences the shape of printed electrodes (see Fig. 2.5), by altering the actual pressure in the vertical and horizontal directions and the shear profile in the paste roll [8].

Some analytic models correlated the hydrostatic pressure on the squeegee and screen surface as well as the shear profile with the screen printing parameters, assuming different rheological properties of the screen printable pastes.

Riemer presented the first systematic analysis by assuming the paste is a Newtonian fluid [6–8]. He calculated the pressure distribution within the paste roll ahead of the squeegee on the squeegee surface as:

$$p_{squeegee} = \int_0^r dp_{squeegee} = [2\alpha \sin \frac{\alpha}{\alpha^2 - \sin^2 \alpha}] \cdot \eta \cdot V_{print} \cdot (1/r)$$

and on the screen surface is

$$p_{screen} = \int_0^r dp_{screen} = [2 \sin^2 \frac{\alpha}{\alpha^2 - \sin^2 \alpha}] \cdot \eta \cdot V_{print} \cdot (1/r)$$

where r is the distance from the nip-contact point between squeegee and screen, α is the angle between the squeegee and screen, V_{print} is the printing speed, and η is the paste viscosity. Fig. 2.6 shows the calculated hydrostatic pressure on the squeegee and screen surface with constant paste viscosity.

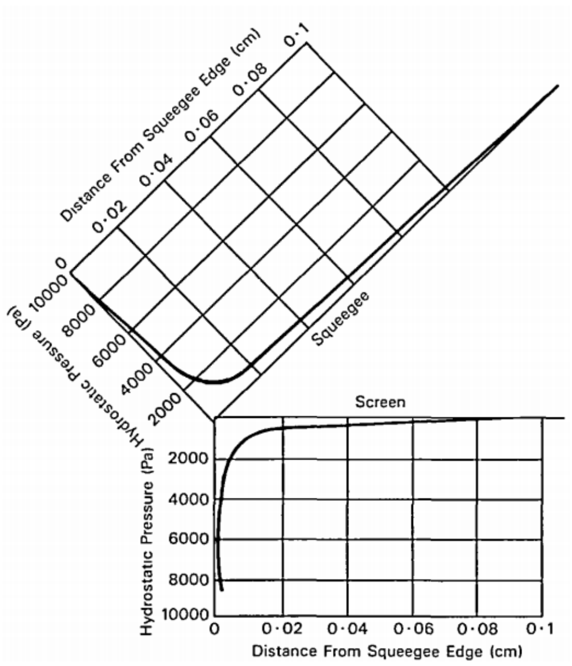

Figure 2.6: Hydrostatic pressure on squeegee and screen surface with ink viscosity η of 1 $Pa \cdot s$ and printing speed V_{print} is 1 cm/s [8].

Glinski *et al.* considered shear thinning properties of solder pastes for stencil printing using the Cross model:

$$\frac{\eta - \eta_\infty}{\eta_0 - \eta_\infty} = \frac{1}{1 + K\dot{\gamma}^m}$$

where $\dot{\gamma}$ is the shear rate, η_0 and η_∞ are the viscosity at zero and infinite shear rate, respectively, K and m are parameters characterizing the shear thinning properties of the fluid [22]. Based on this assumption, the pressure at the stencil surface was calculated via computational fluid dynamics (CFD) method, as shown in Fig. 2.7.

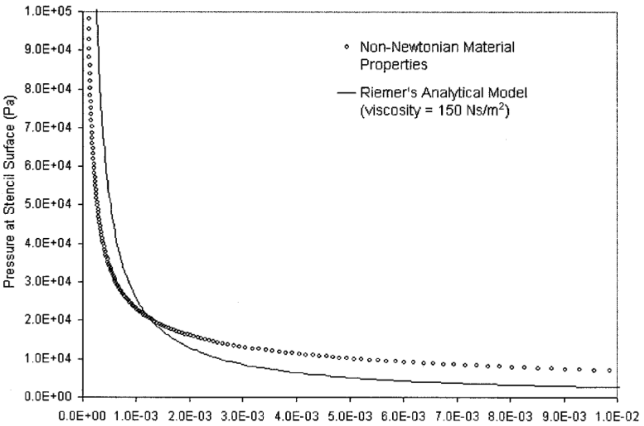

Figure 2.7: Comparison of CFD simulation results for a paste with non-Newtonian properties with Riemer‘s analytical model [22].

Clements *et al.* assumed a power law to describe the flow behavior of the paste $\tau = k\dot{\gamma}^n$ [23] and predicted the pressure distributions (see Fig. 2.8).

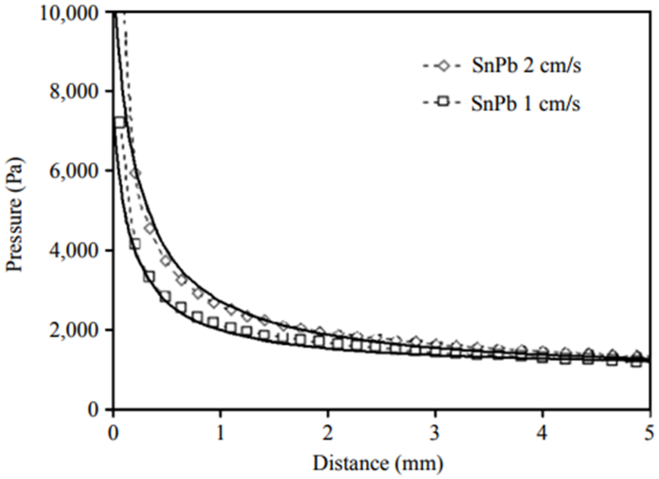

Figure 2.8: Comparison between theoretical (solid lines) and experimental (broken lines) pressure distribution in the paste along the stencil surface concerning the distance from the squeegee tip [23].

All models give a reciprocal or approximately reciprocal relationship between the pressure and the distance from the nip-contact.

2.3 Screen printable pastes

Normally, the screen printing pastes contain

- **Solid particles**, which determines the electronic or other properties of the final printed electrodes;
- **Solvent**, which helps the solid particles form printable pastes;
- **Binder**, which gives cohesion of the printed flims and adhesion force to the substrate;
- **Additive**, which adjusts the other features, especially rheological properties, of the pastes, e.g., dispersants, thixotropic agents, slip agents, etc.

In this section, general requirements of different components will be discussed. The influence of different components on rheological properties will be discussed in detail in the next section.

2.3.1 Solid particles

Depending on the purpose of the printed electrodes, there are different kinds of conductive or non-conductive solid particles for screen-printable pastes. The pastes in some applications, e.g., front-side silver paste for silicon solar cell, contain etching agents (glass frit), forming the ohmic contact between the electrodes and substrates.

Conductive particles

Typical conductive particles, e.g., silver, copper and carbon, are selected based on different requirements of the conductivity.

Silver is mostly used for the devices needing high conductivity, e.g. the conductive finger on solar cells [24], or LTCC and and antennae devices. Silver is more stable considering the oxidation by air, resulting in a longer lifetime of the electronic devices compared to other kinds of metal. Gold and palladium are also suitable as the electrode materials but too expensive.

Copper is cheaper than silver but less stable. However, copper is formulated in screen printable pastes to decrease the cost and to keep the same electronic and chemical properties as silver in some recent research [25].

Carbon is enough to provide the conductivity in some applications, e.g., batteries [26], sensors [27], etc.

Aluminum is also used in silicon solar cells as the rear contact. The holes generated in the silicon wafer move via the aluminum electrode and combine with the electrons in the external circuit.

Non-conductive particles

In some applications, the conductive property is not preferred. For instance, the thermal conductivity but not electronic conductivity of the printed structure is needed. Aluminum oxide, boron nitride, which are non-conductive particle are suitable. Another example is the varistor, which remains ”non-conductive” under low voltage but ”conductive” under high voltage. Therefore, the doping of conductive particles in non-conductive pastes is demanded for this application.

Etching agent

As mentioned above, etching agents (glass frit) form the ohmic contact between the electrodes and substrates in silicon solar cell devices. The "etching" effect of this kind of particle under high temperature is important and strongly depends on its chemical composition.

2.3.2 Solvent

Solvents are used to dissolve the binders and transfer the solid particles to screen-printable formulations.

The selection of the solvent is based on the requirement of the screen-printable pastes. For instance, water is preferred in some application due to environmental reasons, i.e., ink for the T-shirt. Organic solvents are preferred in some applications due to their higher boiling point. In the front-side metallization of silicon solar cells, 500 g silver paste stays on the screen for hours. High boiling point avoids solvent evaporation and keeps the original rheological properties.

The selection of the solvents also depends on the function group of the binder, the requirement of the paste/ink drying properties and the residual chemicals on the solid particles, whether they are hydrophilic or hydrophobic.

Organic solvent

Different kinds of organic solvents are used for screen printable silver paste in printed electronics. Some examples are terpineol, 2,2,4-trimethyl-1,3-pentanediol monoisobutyrate (Texanol), butyl carbitol, butyl carbitol acetate, dimethyl adipate, diethylene glycol dibutyl ether, etc.

2.3.3 Polymer binders

The function of the polymer binder is to increase the cohesion of the printed electrode and adhesion between the printed electrode and substrate. The polymer binder may also influence the rheological properties of the formulations during the screen print process. Ethyl cellulose (EC) is commonly used as polymer binder in screen printable formulations for decades.

2.3.4 Additives

Different kinds of additives, including dispersants, polymer binders, or thixotropic agents, influence the rheological properties of the formulations during the screen printing process as well as mechanical and other features of the printed electrodes.

Dispersant

The function of the dispersant is to stabilize the solid particles and avoid aggregates. The selection of the dispersant depends on the interaction between the dispersant and other components in the formulation, i.e., the surface properties of the solid particles, the polarity of the solvent, polymer as well as the thixotropic agent. Different kinds of dispersants are provided by various suppliers, e.g., Dow, BYK or Lubrizol.

Thixotropic agent

The function of the thixotropic agent is to form a 3D structure throughout the screen printable pastes, stabilizing the solid particles by increasing the yield stress. The selection of the thixotropic agent mainly depends on the type of solvent. Fumed silica, hydrogenated castor oil and diamine based thixotropic agent are commonly used in screen printable formulations.

2.4 Rheological properties and screen printing

As mentioned above, the rheological properties are vital for the process of the screen printing. In this section, some rheological properties will be introduced, including the yield stress, wall slip and thixotropic properties as well as the influence due to solid concentration, dispersants and polymer binders.

2.4.1 Yield stress of screen printable pastes

Yield stress is defined as the stress below which, for a given material, no unrecoverable flow occurs [28]. However, considering the real condition, it seems that most or all materials flow under any stress if the time is long enough [28]. Therefore, the term apparent yield stress seems to be more precise, which is an *engineering* term [29] considering measuring time scale. One could assume that a material has an apparent yield stress when considering it on a reasonable length and time scale comparing the technical application or engineering process.

Screen printable paste needs the apparent yield stress to avoid sedimentation during the shelf life, e.g., at least six months for silver paste as front-side metallization of silicon-based solar cells. More importantly, apparent yield stress is supposed to narrow printed electrode width and increase the aspect ratios of printed features [11].

As for a suspension, the network of particles in screen printable pastes determines their yield stress [30]. Similar to viscosity, the apparent yield stress increases with increasing solid particle volume fraction due to higher number of particle-particle contacts.

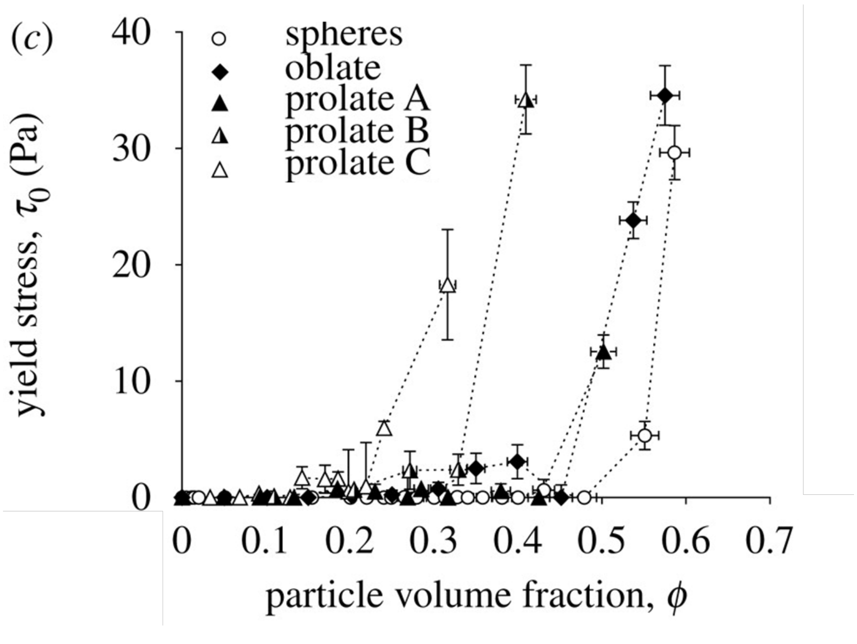

Figure 2.9: Yield stress value as a function of absolute particle volume fraction ϕ but different shapes (aspect ratios) [31].

The apparent yield stress depends on the shape of the particle (see Fig. 2.9) [31], which can be characterized by aspect ratio. Suspensions of particles with high aspect ratio develop a higher yield stress under the same volume fraction, presumably because the particles with higher aspect ratio give larger surface area, resulting in high possibility of interactions among particles.

The additives, e.g., the dispersant, the polymer binder, or the thixotropic agent, can influence the apparent yield stress of the screen-printable paste which will be discussed in the next sections.

2.4.2 Wall slip effect of screen printable pastes

Highly concentrated suspension, whose volume fraction is close to its maximum value, are widely used in different applications, e.g. in fabrication of printed electronics. The increase of the solid volume fraction leads to a rise of the suspension viscosity, which is helpful for printing precise patterns. However, the highly concentrated suspension shows wall slip effect, which has been discussed for decades. Wall slip in suspensions is related to the migration of particles under shear, resulting in a liquid film or a film showing a lower particle concentration than suspension's average particle concentration at the interface.

Wall slip has already been reported to improve the electrode quality in stencil printing [12, 13]. Fewer particles were found adhering to the stencil when the paste showed a higher wall slip, resulting in a perfect shape of printed arrays on the substrate (see Fig. 2.10).

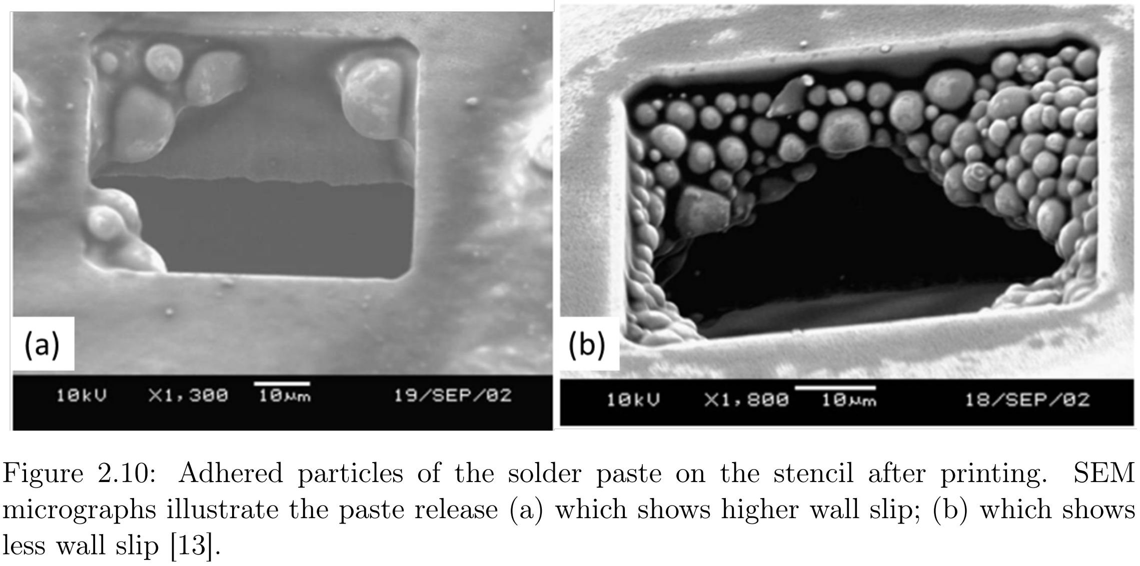

Figure 2.10: Adhered particles of the solder paste on the stencil after printing. SEM micrographs illustrate the paste release (a) which shows higher wall slip; (b) which shows less wall slip [13].

2.4.3 Thixotropic effect of screen printable pastes

Thixotropic behavior means the time-dependent change in viscosity, which is related to the paste structure destruction and recovery in the screen printing process. In the screen printing process, the paste is on the screen after the flooding step. The high shear in the printing process leads the deconstruction of the paste. After laying on the substrate, the paste recovers to the original state (theoretically). Hoornstra *et al.* for the first time simulate the paste behavior during the screen printing with an oscillation measurement, where the paste is under shear in three intervals [9]:

- **I-pre-print**, where the sample is sheared in an oscillatory mode with low amplitude to simulate the paste at rest;
- **II-print**, where the sample is sheared in an oscillatory mode with high amplitude to simulate when the paste is pressed by the printing squeegee through the screen opening;
- **III-post-print**, where the sample is sheared in an oscillatory mode again with low amplitude to simulate the paste's recovery and regain its structure.

This kind of 3 interval test, which is mainly used to represent the thixotropic character after shear, is named as **three intervals thixotropic test (3ITT)**.

Hoornstra *et al.*, as mentioned, did the measurement with an oscillation style. Therefore the storage modulus G' and loss modulus G" are gained, representing the elastic and viscous properties of the paste, respectively. Lower loss modulus is proposed to relate to easier printability and higher storage modulus is proposed to lead to a faster recovery after printing. The phase shift or loss angle δ, i.e. arc tan G"/G', should be closer to 90 ° , i.e., very fluid-like, in the 2nd interval for better printing and reach to lower than 45 °, i.e., very solid-like, in the 3rd interval as soon as possible to stop the paste spreading for an improved aspect ratio (see Fig. 2.11).

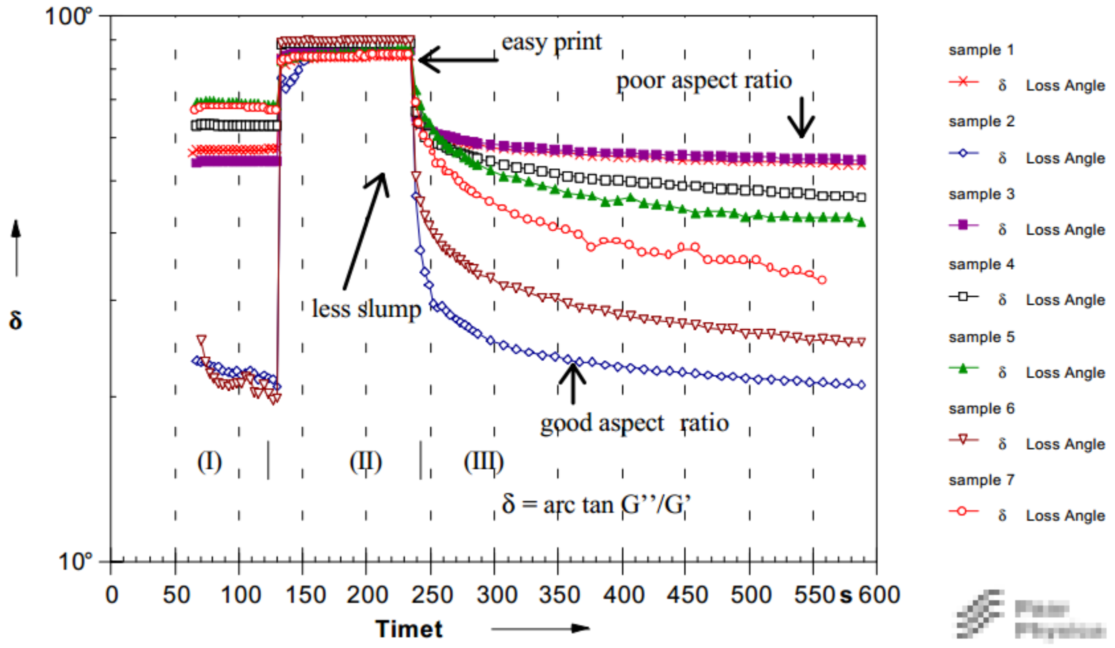

Figure 2.11: Phase shift or loss angle δ of the pastes measured with 3ITT (oscillation) [9]. The higher loss angle in the second interval is proposed to lead to an easier printability. The faster drop of the loss angle indicates the faster recovery of G', leading to a faster stop of the paste spreading and a better aspect ratio.

However, this model is not suitable for modern paste with very high viscosity. This model related the paste spreading to the recovery of the structure tested by the rheometer. However, in this study, combining the high-speed camera and screen printing indicates the spreading happens very fast, which cannot be detected by the traditional rheometer.

Neidert *et al.* simplified the 3ITT with the rotational method and concluded the viscosity recovery, rather than storage and loss modulus change, represents the spreading of the paste after printing [10]. They compared the recovery time of reaching a specific viscosity, 80 $Pa \cdot s$, for different pastes and found the paste, which reached to this value faster, shows a narrower printed electrode.

Qin *et al.* concluded that the rotational 3ITT correlates to printed electrode width in front-side metallization of the silicon-based solar cell [32, 33]. They also indicated that the significantly increased viscosity in the final interval leads to an uniform film. However, the rebuilding of the structure seems to be relatively less important.

2.4.4 Tack or sticky behavior of screen printable pastes

As viscoelastic materials, screen printable pastes often shows tacky or stringy behavior during the process when paste is released from the screen, i.e., snap-off process. The tack behavior has been related to the loss factor $\tan\delta = G"/G'$ [34]. A paste with $\tan\delta = 1$ (G' and $G"$ are with the same value), shows serious tack or stringy behavior. This phenomenon is reduced or even prevented if $\tan\delta$ is produced to be either lower or higher than this intermediate range.

2.4.5 Influence of solid concentration

The effect of particle volume fraction on suspension viscosity is essential to understand the non-Newtonian behavior of screen printable paste. The fluid flow is disturbed by the dispersed particles in the flow field.

Einstein built the classical model for infinitely dilute [35, 36], non-interacting hard spheres, showing increased suspension viscosity as a linear function of the solid volume fraction ϕ:

$$\eta_r = \frac{\eta}{\eta_s} = 1 + 2.5\phi$$

where η is the suspension viscosity, η_s is the viscosity of suspension medium and η_r is the relative viscosity. However, the Einstein equation only applies at very low solid volume fraction $\phi < 0.01$, assuming there is no hydrodynamic interacion among the particles. Normally, the solid volume fraction is much higher than this range for screen-printable pastes. Therefore, hydrodynamic interactions among particles become important and have to be considered. Batchelor calculated the relative viscosity considering the effect of hydrodynamic interactions between solid particles as [37]:

$$\eta_r = \frac{\eta}{\eta_s} = 1 + 2.5\phi + 6.2\phi^2$$

This equation is validated to comparingly higher volume fractions $\phi < 0.1$. For even higher particle volume fractions, it is difficult to analyze the multi-particle interactions theoretically. Several equations are proposed to correlate the suspension viscosity to the particle volume fraction. One of the most used semi-empirical equations was proposed by Krieger and Dougherty [38]:

$$\eta_r = \left(1 - \frac{\phi}{\phi_{max}}\right)^{-2.5\phi_{max}}$$

where ϕ_{max} is the maximum packing fraction for monodisperse hard spheres (0.64). This equation reduces to Einstein relation at low particle concentration. The suspension is blocked and cannot flow when approaching the maximum volume fraction ϕ_{max}. Quemada [39] suggested a similar model to predict η_r:

$$\eta_r = \left(1 - \frac{\phi}{\phi_{max}}\right)^{-2}$$

Fig. 2.12 shows the relative viscosity depending on volume fraction according to different models.

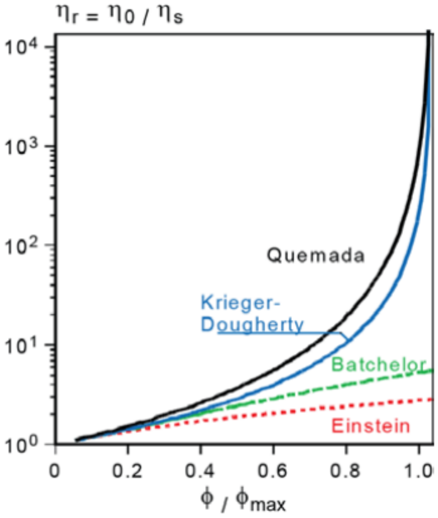

Figure 2.12: The dependence of relative viscosity on volume fraction, according to different models [40].

In the solvent based suspension, the electrostatic forces among particles are very small and can be neglected compared with it in the water based suspension. However, there is always attractive interaction between any pair of moleculars, including non-polar atoms, due to the interaction of instantaneous multipoles, which is named as dispersion force by Frit London [41], which is part of the van der Waals attraction.

Besides, there may be an attractive force among particles except of the ubiquitous van der Waals attraction. When there is macromolecules dissolved in the liquid phase, solid particles are pushed together by the liquid phase no matter whether there is neither direct interaction between two particles nor between particle and macromolecules (in this study, polymer binder) solutions [42]. In the highly concentrated suspension, there is a possibility that the distance between two particles is very small and the dissolved macromolecules cannot enter the gap between the particles, resulting in a pure solvent. In this case, there is a polymer concentration difference between the liquid in the gap and the liquid outside, leading to an osmotic pressure (see Fig. 2.13) and pushing particles together. Therefore, dispersants are necessary to stabilize the highly concentrated suspension in solution of macromolecules.

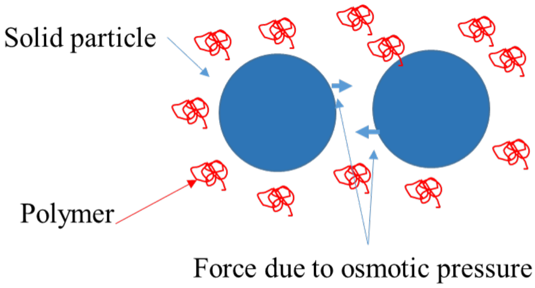

Figure 2.13: Aggregation mechanism of solid particles in the solvent with dissolved macromolecules.

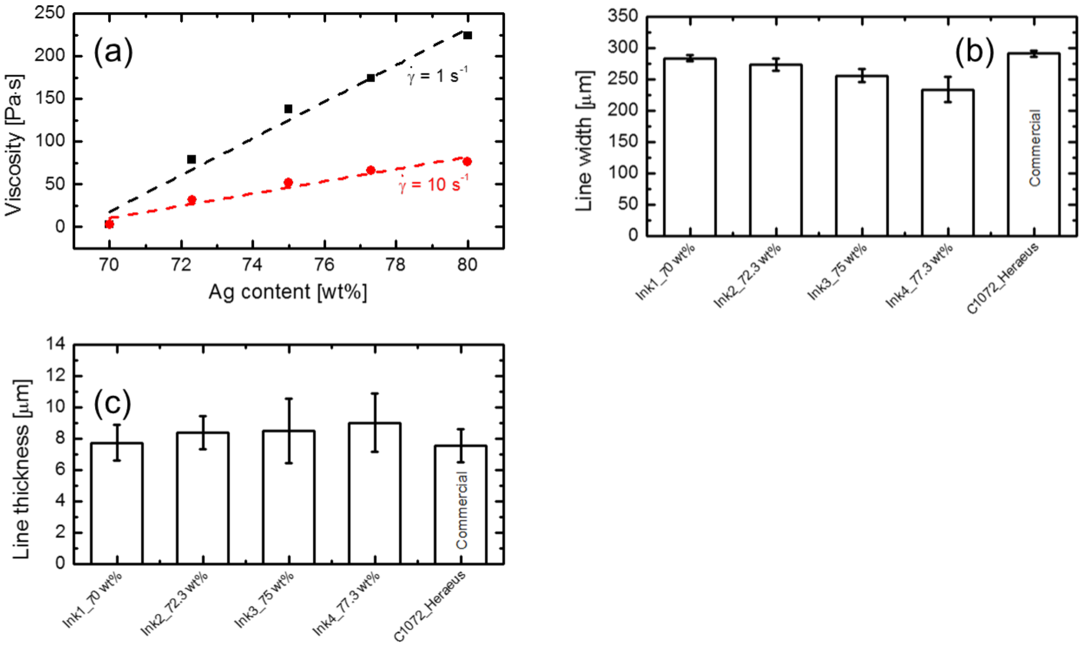

Figure 2.14: The dependence of viscosity under shear rate at 1 and 10 s^{-1}(a), printed line width(b) and printed line thickness(c) on the solid content of water-based silver pastes printed on ceramic taps as described in [43] by Bourel *et al.*.

To avoid spreading, the screen-printable pastes for slender fingers are normally viscous with high particle volume fraction ($\sim 50\%$). Since the particle concentration influences the electronic properties after drying and sintering, it is important to choose a suitable particle volume fraction for this kind of paste. Bourel *et al.* formulated water-based model silver inks for screen printing on ceramic substrates [43]. The silver content effect on rheological and electrical properties of the model pastes was studied. As can be seen in Fig. 2.14, the viscosity increases with silver content (see Fig. 2.14(a)) and the printed line width decreases (see Fig. 2.14(b)) with solid content. However, due to the large variation of the printed line thickness, the influence of the solid content is not significant although there is an increasing trend (see Fig. 2.14(c)).

2.4.6 Influence of dispersant

As mentioned above, there are weak attractive interactions among the solid particles when they are mixed with solution of polymer binders. Therefore, dispersants are added into the formulations to avoid the aggregates. Dispersants do their job when they are absorbed by the solid particles and provide repulsion between particles.

Two kinds of mechanisms provide the repulsion by the dispersants (Fig. 2.15):

- **Electrostatic stabilization**: in this case, all particles carry a charge with the same sign and repel each other due to the coulomb force.
- **Steric stabilization**: in this case, all particles are covered by polymer (surfactant), molecules extending into the solvent. Due to the osmotic pressure created when these layer overlap, the solid particle are repelled.

Both types of repulsion can be inferred when dispersants are added to a paste formulation and adsorb onto the particles.

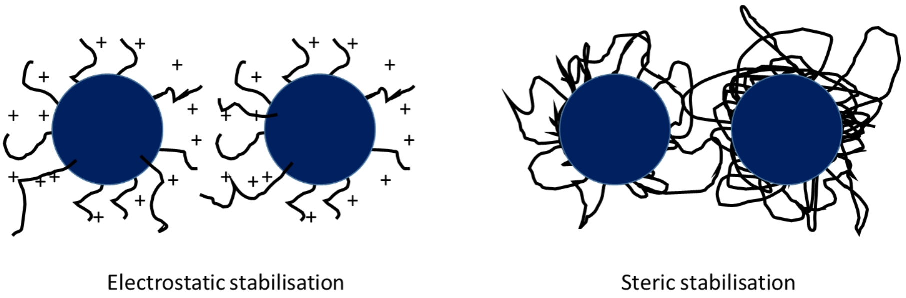

Figure 2.15: Schematic diagram of electrostatic stabilization and steric stabilization.

As mentioned above, the viscosity increases with solids concentration. However, to achieve the electronic or mechanical properties of the final printed electrodes, high solid concentration is important in some screen printable pastes. Due to the printability and device performance, dispersants are added into the formulation to reduce the paste viscosity at high solids content.

Rudez *et al.* prepared screen printable zinc oxide inks for thick film varistors and studied the influence of dispersant on the printed film [44]. They compared the screen printable inks containing 70 $wt\%$ solid, with and without dispersant.

The paste without dispersant (A-70WS in Fig. 2.16) had a high zero shear viscosity of 7710 $Pa \cdot s$, and the printed film had defects, such as missing mesh imprints or stencil clogging, observed under a confocal microscope (A-70WS in Fig. 2.17). By adding the dispersant, the ink viscosity is reduced, and the zero shear viscosity dropped to 1980 $Pa \cdot s$ (A-70S in Fig. 2.16). According to the confocal microscope images, the printing behavior was improved (A-70S in Fig. 2.17).

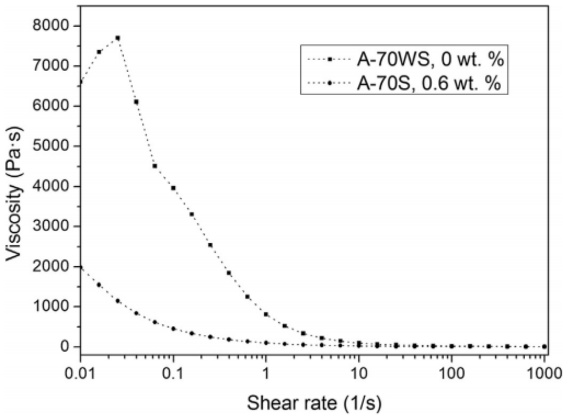

Figure 2.16: Flow curves of ink A-70WS (ZnO ink containing 70 $wt\%$ solid content and without dispersant) and A-70S (ZnO ink containing 70 $wt\%$ solid content and with 0.6 $wt\%$ dispersant). The viscosity is dramatically reduced by adding the dispersant [44].

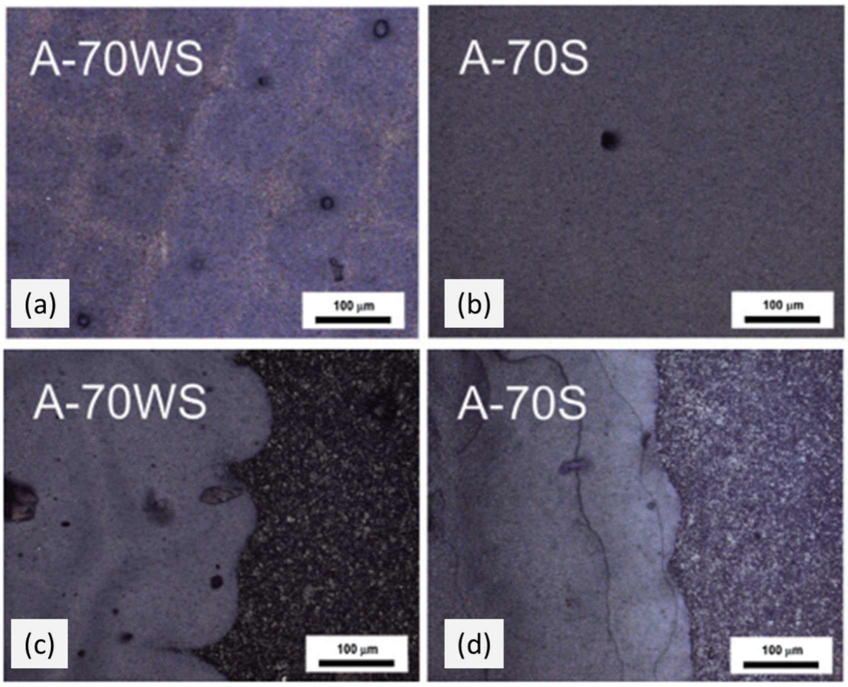

Figure 2.17: Confocal micrographs showing the surface (a, b) and the edge (c, d) of the printed films. The adding of the dispersant reduces the mesh mark (b) and form a smoother edge (d) [44].

2.4.7 Influence of polymer binder

The polymer binder is an important ingredient for screen printable pastes because it influences the viscoelastic properties of the paste during screen printing process and the mechanical strength, density, and porosity of the printed electrodes.

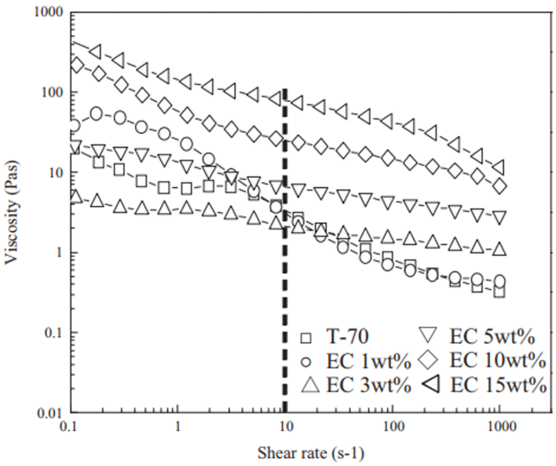

Figure 2.18: Flow curves of the LSTF pastes with different EC content. T-70 is the reference paste with 70 $wt\%$ of solid particles. The high shear viscosity increases monotonically with EC concentration, and the shear thinning behavior gets less pronounced when the concentration is higher than 1 $wt\%$ [45].

The polymer binder concentration should be selected carefully for different formulations. With too low polymer binder concentration, the adhesion of the paste on the substrate is not strong enough and cracking may develop during drying as a result of the reduced network strength among solid particles [45]. With too high polymer binder concentration, the paste viscosity increases too much, and the printing becomes difficult when the solid content (mass fraction) is kept. Except for the absolute viscosity values, the degree of shear thinning of the screen printable paste is also adjusted by the polymer binder.

As described by Murakami *et al.*, the viscosity of LSTF ($La_{0.6}Sr_{0.4}Ti_{0.3}Fe_{0.7}O_{3-\delta}$) for solid oxide fuel cells (SOFCs) increased with ethyl cellulose (EC) concentration and shear thinning was observed when the EC content was low (less than 1 $wt\%$) and particles were not well dispersed [45]. With increasing the EC content, shear thinning became less and less pronounced although the absolute viscosity level increased (Fig. 2.18).

Beside the polymer binder concentration, the molecular weight (see Table 2.1) of the polymer binder (even with the same repeated unit for the polymer) also influences the rheological and hence the properties (morphology and porosity) of the printed flim due to the polymer absorption on the solid particle surface and the thickening of the solvent (Fig. 2.19). Shin *et al.* [46] prepared the LSTF ($La_{0.6}Sr_{0.4}Ti_{0.3}Fe_{0.7}O_{3-\delta}$) pastes with an organic solvent BDGAC (diethylene glycol monobutyl ether acetate) and adjusted the EC concentration as Table 2.1. With

Table 2.1: The molecular weight of different kinds of ethyl cellulose supplied by Dow Chemical [46]. P1-P12 are formulations with the same amount of solid particles (70 $wt\%$), but different type and amount of EC as indicated.

EC	M_n	M_w	EC 1.5 $wt\%$ Pastes	EC 3.0 $wt\%$ Pastes	EC 3.0$wt\%$ Pastes
STD-4	14,000	44,000	P1	P6	P11
STD-10	26,000	73,000	P2	P7	P12
STD-45	49,000	141,000	P3	P8	
STD-100	57,000	179,000	P4	P9	
STD-200	80,000	238,000	P5	P10	

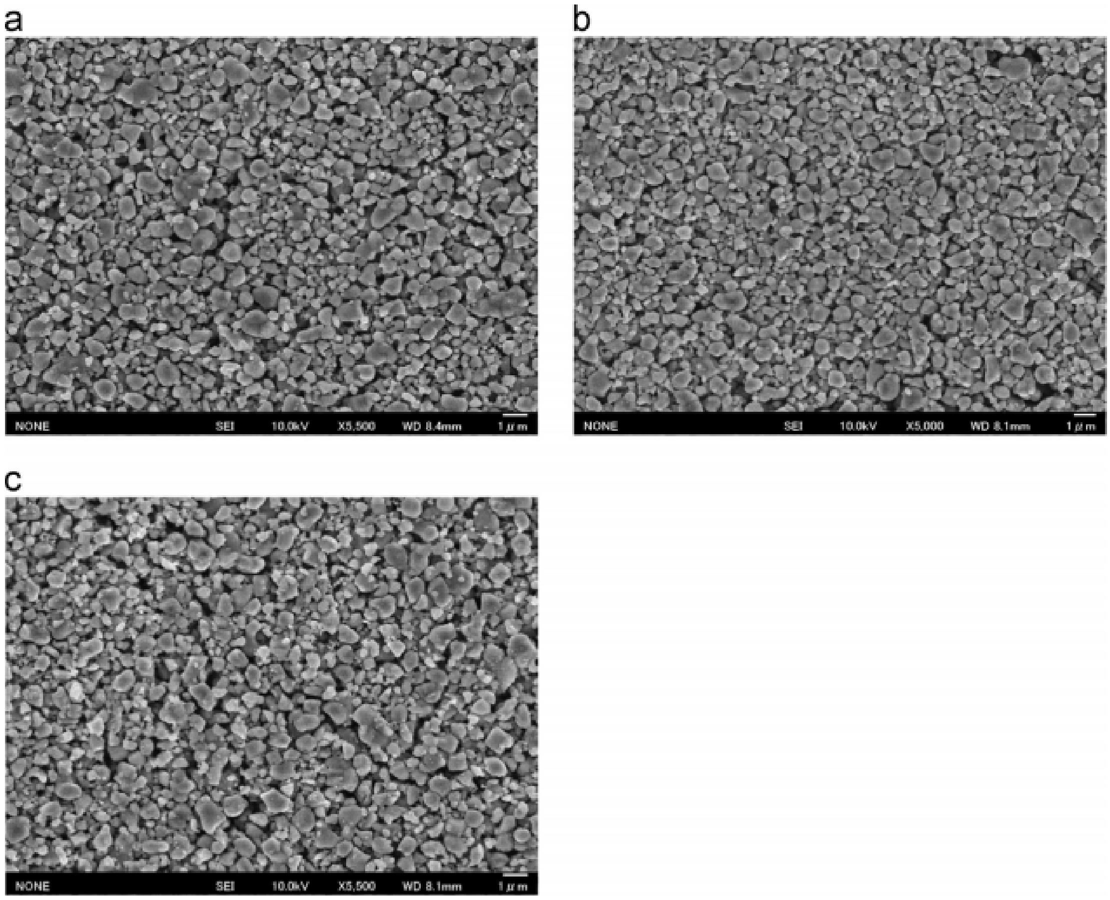

Figure 2.19: SEM images of the (a) P1, (b) P3, and (c) P5 thick films sintered at 1000 °C for 1 h [46].

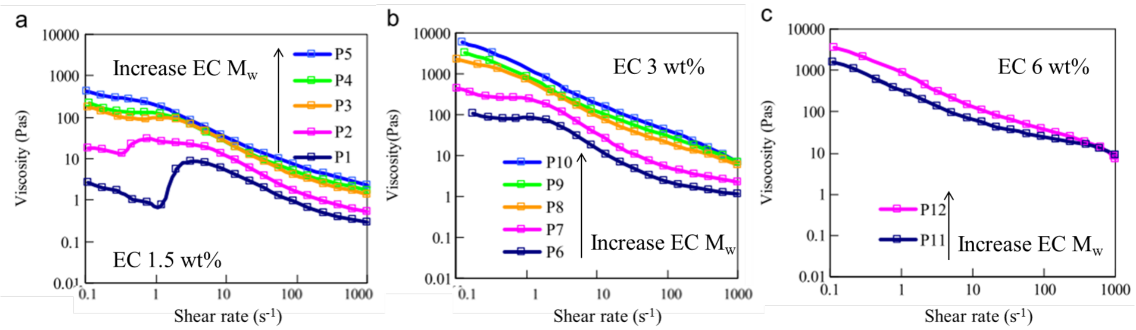

Figure 2.20: Flow curves of the pastes using (a)1.5 $wt\%$ EC, (b)3.0 $wt\%$ EC, and (c) 6.0 $wt\%$ EC. [46].

the same EC concentration, the paste viscosity increases with the polymer molecular weight (see Fig. 2.20). All pastes show shear thinning behavior. Some of the pastes (P1 to P7) show a shear thickening flow behavior, probably due to the weak steric stabilization provided by the low EC content.

Chapter 3

Materials and sample preparation

3.1 Materials

In this section, an overview of different solid particles, rheological additives and solvents used in the experiment will be listed.

3.1.1 Particles

Two kinds of solid particles were used in this study. Silver particles, which are mainly used in the silver paste, are used in the model system for investigation of wall slip. Zinc oxide (ZnO) particles are used in the model system for investigation of screen printing process by a high-speed camera.

Silver particles

Due to its good conductivity, stable chemical properties and suitable price, silver is one of the best choices in the printed electrodes industry. In this study, the Silver Powder Type *AEP-2* was purchased from Ames Goldsmith Corp. USA. The powders are produced during wet-chemical synthesis. Fig 3.1 shows the approximately spherical shape of the particles. According to the supplier, the powders have a particle size distribution characterized by the following quantities:

$$D_{10} = 1.0\ \mu m$$
$$D_{50} = 2.0\ \mu m$$
$$D_{90} = 4.0\ \mu m$$

where D_{10}, D_{50} and D_{90} are the diameters at which 10, 50 and 90 % of the sample's volume compromise particles with a diameter less than that value.

The chemicals used in the preparation step are not disclosed by the supplier. Therefore, the surface properties of the particles is unknown. The surfactant (DISPERBYK-111) used to disperse the silver powders is chosen before this study by the author.

The density of the bulk silver is 10.49 g/cm^3.

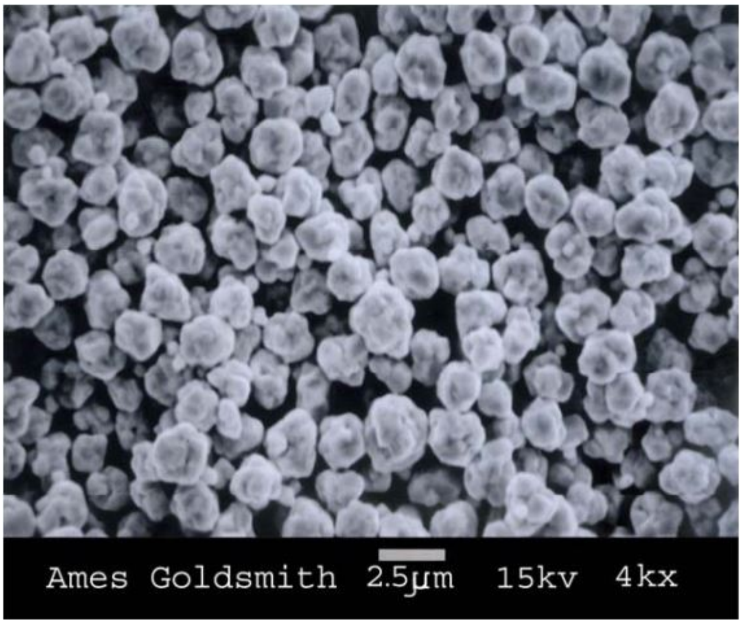

Figure 3.1: SEM pictures of Ames Goldsmith AEP-2 powders

ZnO particles

Zinc oxide (ZnO) powders are commonly used for the screen printable paste for varistors [44, 47–50]. In this study, the ZnO powder is Zinc Oxide *Pharma 4*, which was purchased from Grillo GmbH. The density of the ZnO is 5.61 g/cm^3. According to the supplier, the powders have a particle size distribution characterized by the following parameters:

$$D_{10} = 0.19\ \mu m$$
$$D_{50} = 0.66\ \mu m$$
$$D_{90} = 1.57\ \mu m$$

3.1.2 Additives

As mentioned above, the additives influence the mechanical properties and rheological properties of the screen-printable pastes. Most commonly used additives include:

- **Dispersant**: additive to attach to the solid particle surface and provide steric stabilization among particles;
- **Polymer binders**: additive to increase the viscosity and provide the adhesion force between the printed paste and substrates after drying;
- **Thixotropic agent**: additive to increase the yield stress during the storage for better stabilization. It influences the leveling of the printed film and formation of mesh marking.

Dispersant

There are two kinds of dispersants used in this study. One is DISPERBYK-111 for the silver particle. DISPERBYK-111 is a copolymer with acidic groups, which is purchased from BYK-Chemie GmbH. The density is 1.16 g/cm^3 and boiling point is 135.00 $°C$. The other one is DISPERBYK-108 for the ZnO particles. The chemical composition is a hydroxy-functional carboxylic acid ester with pigment-affinic groups. The density is 0.94 g/cm^3 and boiling point is above 200.00 $°C$. Both of the dispersants are used without further treatment.

Polymer binders

Two kinds of polymer binders are used in this study.

Poly-stearyl methacrylate(PSMA) is supplied by BASF SE. The molecular weight is 41 kg/mol. The PSMA is dissolved in highly isoparaffinic hydrocarbon Nexbase 3030 (Neste Corporation). Fig 3.2 illustrates the chemical structure of PSMA. The thermogravimetric analysis (TGA) of the PSMA solution in Nexbase 3030 illustrates the solvent evaporates between 120 to 230 $°C$ and the polymer burns out near 350 $°C$ according to the differential scanning calorimetry (DSC) curve. There is no residual above 600 $°C$ (Fig 3.3).

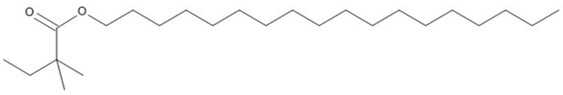

Figure 3.2: The chemical structure of Poly-stearyl methacrylate (PSMA).

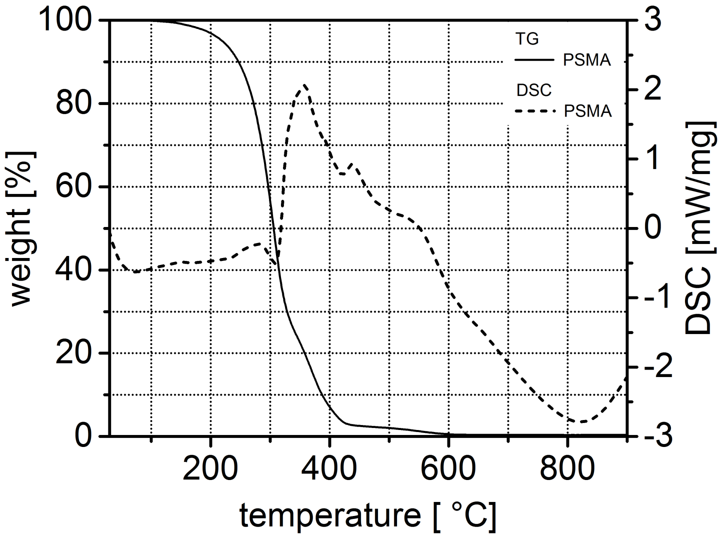

Figure 3.3: The thermal analysis of Poly-stearyl methacrylate (PSMA).

Ethyl cellulose (EC N4) is purchased from Dow Chemical. The molecular weight is 44 kg/mol [46]. Fig 3.4 illustrates the chemical structure of ethyl cellulose. The thermogravimetric analysis (TGA) and the differential scanning calorimetry (DSC) curve demonstrate the burning of EC N4. There is almost no residual above 480 °*C* (Fig 3.5).

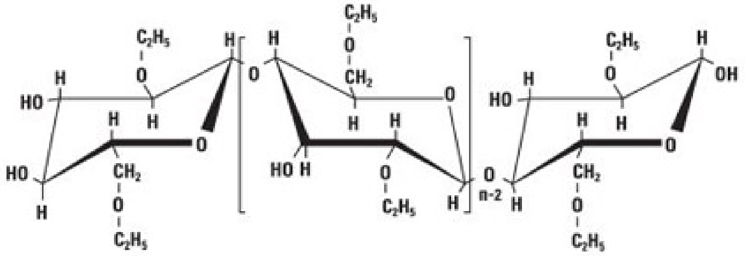

Figure 3.4: The chemical structure of ethyl cellulose.

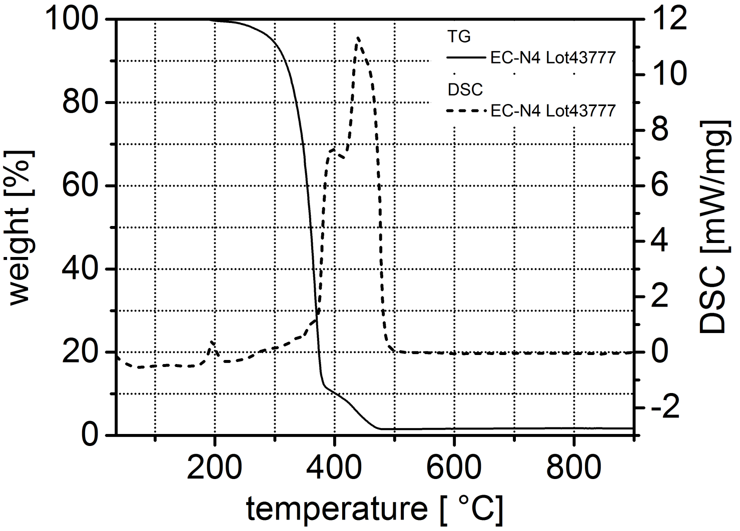

Figure 3.5: The thermal analysis of ethyl cellulose.

Thixotropic agents

There are two kinds of thixotropic agents used in this study. Both of them are purchased from Elementis Specialties. As mentioned above, thixotropic agents for solvent-based formulations are commonly hydrogenated castor oil and diamines. Thixatrol ST is a mixture of these two chemicals while Thixotral Max is pure diamines [34]. TGA results illustrate both of the two kinds of thixotropic agents burns out above 600 °*C* (Fig. 3.6).

3.1.3 Solvents

Solvents are essential to transform the solid particles into paste-like mixtures.

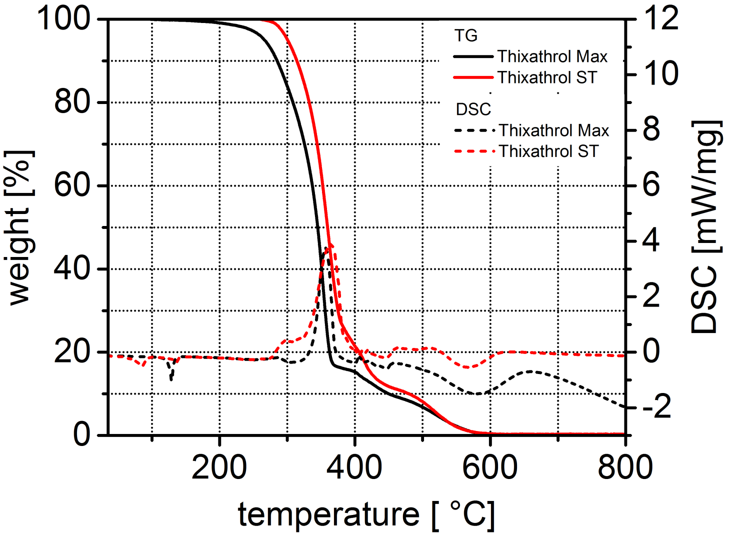

Figure 3.6: The thermal analysis of Thixatrol ST and Thixatrol Max.

Texanol

Texanol (2,2,4-Trimethyl-1,3-pentanediol monoisobutyrate) is commonly used for screen printable pastes, due to its excellent dissolve ability to different kinds of polymer binders. The boiling point is as high as 254 $°C$, which prevents evaporation during the printing process. The low evaporation rate ensures the stability of the paste in the 8 hours printing. Fig 3.7 shows the chemical structure. Texanol is purchased from Sigma-Aldrich, and the density is 0.95 g/cm^3 at 20 $°C$.

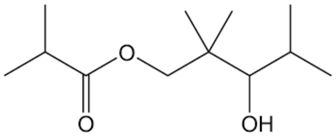

Figure 3.7: The chemical structure of Texanol.

Triacetin

Triacetin is a solvent, which has different polarity compared with Texanol. The miscibility of these two kinds of solvents forms a weak phase separation in the paste, leading to a change in wall slip with different concentrations of triacetin. The boiling point of triacetin is 258 $°C$, and the density is 1.16 g/cm^3. Fig 3.8 shows the chemical structure of triacetin.

3.2 Sample preparation

Normally the pastes contain organic vehicle and solid particles. The rheological properties of the pastes are determined mostly by the organic vehicle when the type

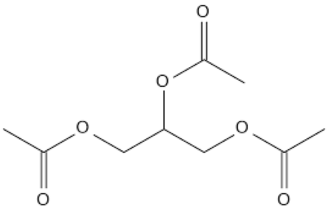

Figure 3.8: The chemical structure of triacetin.

and concentration of the solid particle are fixed. The organic vehicle is prepared firstly, for better mixing of the liquid phase, especially the solvent and dispersant. Afterwards, the solid particles are mixed with the organic vehicle and milled to get a homogeneous paste.

3.2.1 Organic vehicle preparation

Figure 3.9: Dissolver DISPERMAT®

The polymer has to be dissolved in the solvent firstly. High shear and high temperature help the polymer dissolution to some extent. In this study, the temperature is set at 60°C and the time is 30 min for entirely dissolving. Fig. 3.9 shows the dissolver, which provides up to 2000 rpm rotational speed and with an external temperature controlling system.

The dispersant and other rheological agents, e.g.,thixotropic agent, are added to the polymer solution and mixed thoroughly.

As mentioned in the section 3.1.2, the thixotropic agent can form 3D structure through the liquid phase after heat activation [34]. The activation temperature and shear rate should be selected according to the type of thixotropic agent and the solvent. In this study, two kinds of thixotropic agents, i.e., Thixatrol ST and

Thixatrol Max, are used for silver pastes and ZnO pastes, respectively. The only difference for heat activation of these two thixotropic agents is the temperature, and the detailed procedure is as below:

- **Mixing**, the thixotropic agent powders are mixed with the other component at room temperature for 15 *min* and at 200 *rpm* with a dispensing homogenizing blade.
- **Activation**, the mixture is heated to 55 $°C$ for Thixatrol ST and 65 $°C$ for Thixatrol Max for 30 *min* and at 1000 *rpm*.
- **Cooling**, the mixture is cooled down to room temperature while stirring at 200 *rpm*.

3.2.2 Paste preparation

As mentioned above, it is important to break the aggregates among the solid particles and get a well-dispersed homogeneous paste. To break the aggregates, external shear is effective. Three roll mill is a practical and universal machine widely used in paste preparation. The device EXAKT 80 has been used in this study (see Fig. 3.10).

Figure 3.10: Three roll mill EXAKT 80

The velocities of the three rollers are different during the milling, which are represented as v_1, v_2 and v_3, and $v_1 < v_2 < v_3$. The sample is put between the left and middle rollers (see Fig. 3.11). Friction between the rotating rollers and the sample creates a force on the solid particles. Due to the speed differences between two rollers, the force increases from slower to faster roller. Different forces acting on the same agglomerate result in separation.

The force difference depends not only on the roller speed but also on the gap between two rollers. The set gap limits the biggest particle which can pass the gaps. Some of the solid particles are soft and deformable, for example, silver particles. Therefore it is important to reduce the gap step by step. Otherwise, the particles

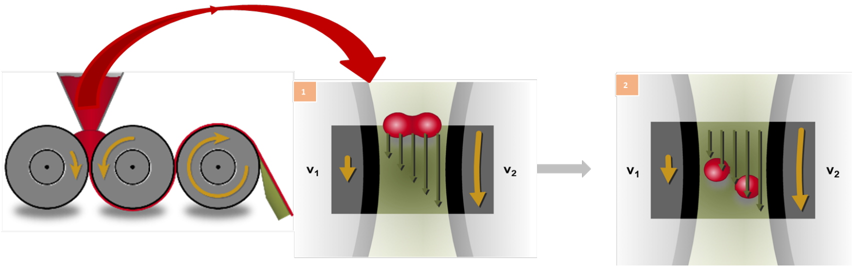

Figure 3.11: Mechanism of three roll mill

may loose the original shape, i.e., from spherical to flake shape. The shape change may influence the rheological properties during the screen printing process and also the final electronic properties of the printed electrodes.

The samples were milled for six times in this experiment, and the detailed parameters are listed in Table 3.1. 1st gap is the gap between left and middle rollers. 2nd gap is the gap between middle and right rollers. The rotational speeds of the three rolls are set as 1:3:9 by the manufacturer. The rotational speed of the right roller is always set to 150 *rpm* in this study.

Table 3.1: Parameters for the three roll mill process. The rotational speed of the right roller is always set to 150 *rpm*.

Round	1st Gap (μm)	2nd Gap (μm)
1	50	40
2	40	30
3	30	20
4	20	10
5	10	5
6	5	5

3.3 Formulations

3.3.1 Silver model pastes for wall slip study

Table 3.2: Formulations of four vehicles for silver model pastes

	V1	V2	V3	V4
PSMA solution [$wt\%$]	41.84	41.84	41.84	41.84
Thixatrol ST [$wt\%$]	5.10	5.10	5.10	5.10
Disperbyk 111 [$wt\%$]	2.04	2.04	2.04	2.04
Texanol [$wt\%$]	51.02	46.94	43.88	40.82
Triacetin [$wt\%$]	0.00	4.08	7.14	10.20

The four organic vehicle formulations for silver model pasts have the same PSMA solution, Thixatrol ST and Disperbyk 111 concentrations as 41.84, 5.10 and 2.04

wt%, respectively, with only different Texanol to triacetin concentrations listed in Fig. 3.2. The vehicles are afterwards mixed with silver particles at a ratio 9.80: 90.20 to prepare the silver pastes for wall slip study.

3.3.2 ZnO model pastes for high-speed camera investigation

Table 3.3 lists the formulations for ZnO model pastes. The contents of solvent, solid particle and dispersant are kept almost constant, and the formulations are varied with different kinds and concentrations of additives, i.e., the polymer binder and the thixotropic agent. As mentioned above, the organic mediums are prepared previously before the paste preparation. Therefore, all pastes in this study are labeled with the additive type and additive concentration in the medium. For instance, EC 5.5 means the pastes with the medium, which contains 5.5 *wt*% EC in the medium.

Table 3.3: Composition of ZnO model pastes for high-speed imaging of the screen printing process.

Lable	EC 9.5	EC 7.5	EC 5.5	T-Max 9.5	T-Max 7.5	T-Max 5.5
Texanol [*wt*%]	9.22	9.24	9.26	9.22	9.24	9.26
EC N4 [*wt*%]	0.97	0.75	0.54	-	-	-
Thixatrol Max [*wt*%]	-	-	-	0.97	0.75	0.54
ZnO [*wt*%]	87.20	87.39	87.58	87.20	87.39	87.58
Disperbyk 180 [*wt*%]	2.61	2.61	2.62	2.61	2.61	2.62

Chapter 4

Methodology

4.1 Rheological measurements

As mentioned above, the rheological properties of the screen printable paste are important for the printing process. Therefore, it is essential to conduct these measurements. In this section, different rheological properties, which have been measured in this study, are described, including yield stress, flow curve, slip velocity, thixotropic, and elongational break-up behavior.

4.1.1 Yield stress measurement

The apparent yield stress σ_y describes the minimum stress needed to force the paste to flow. High solids content pastes typically present wall slip effect when measured with traditional plate-plate, cone-plate and cylinder geometries. Therefore, the *vane-in-cup* geometry has been used to determine the yield stress for such kind of paste [51]. It considers only a "tearing stress" but not viscometric flow when using the vane-in-cup geometry and generally slip at the cup wall can be neglected.

The vane used in this study has a diameter of $d_{vane} = 10\ mm$ with four blades,

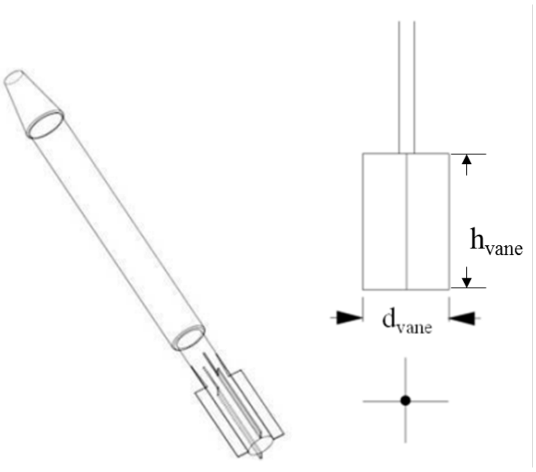

Figure 4.1: Vane used for yield stress measurement in this study [52].

and the blades have a height of $h_{vane} = 20\ mm$(See Fig. 4.1). The cup has a diameter of $d_{cup} = 20\ mm$.

The yield stress is measured using stress-steps, in which the yield stress is found as the point at which the slope of the logarithmic deformation ($\log\gamma$) as a function of the logarithmic shear stress ($\log\sigma$) changes from low value ≈ 1 to a high value $\gg 1$. The choice of the shear stress range depends on the samples. In each decade 10 stress values are selected, and for each point the sampling time is 10 s. The deformation γ is plotted over the shear stress σ, and the point of intersection between two adjusted tangents is determined using the RheoWin software from Thermo Fischer (Fig. 4.2). At least three measurements were done for each sample and the calculated standard deviations are shown as error bars in the figures in the results section.

Theoretically, the slope in the first range should be one because there is only elastic deformation at stresses below the yield stress. Probably, due to irreversible structure changes below the apparent yield stress, a value slightly higher than one is formed in many experiential tests.

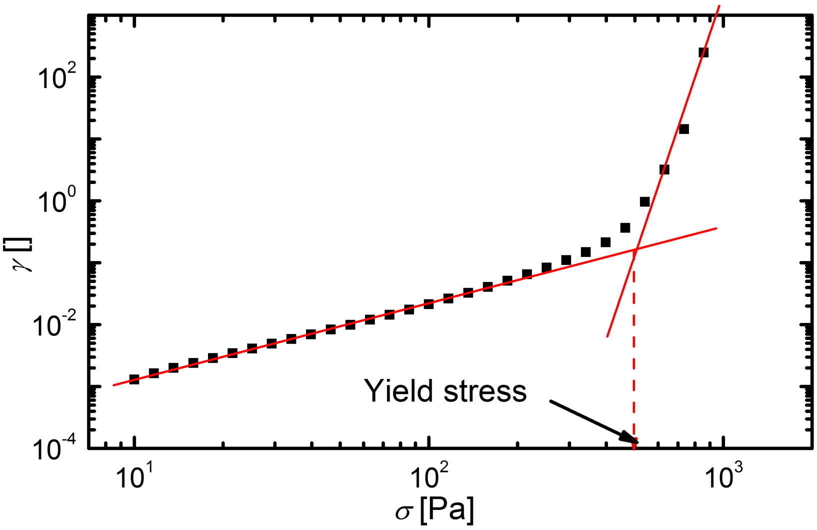

Figure 4.2: Example for yield stress evaluation: ZnO paste with 7.5 T-Max.

4.1.2 Flow curve

Flow curve gives an overview of the viscosity η change with shear rate $\dot{\gamma}$. As mentioned above, most screen printable pastes are shear thinning, i.e., η decreases with increased $\dot{\gamma}$, which is important for the screen printing process. The flow curve measurements in this study were conducted using a rotational rheometer (MCR 302, Anton Paar) with plate-plate geometry (25 mm diameter) and a gap size of 500 μm if not stated otherwise. At least three measurements were done for each sample, and the calculated standard deviations are shown as error bars in the figures.

Fig.4.3 shows a schematic drawing of a plate-plate geometry. In a shear stress controlled mode, the upper plate (with diameter R) is turned under an applied

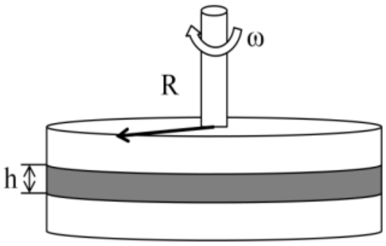

Figure 4.3: Schematic diagram of a plate-plate setup of a rotational rheometer with the gap height h and radius R.

torque T around the axis with a gap size h between it and the bottom plate. Accordingly, the shear stress σ for plate-plate geometry is given by

$$\sigma = \frac{2T}{\pi R^3}$$

The angular frequency ω is detected by the machine. Three premises are assumed: 1.The gap is fully filled with the sample; 2.There is no slip between the sample and the rheometer wall; 3.There is uniform shear within the sample during the experiment. The shear rate $\dot{\gamma}$ at the wall is then defined as

$$\dot{\gamma}(x) = \frac{\omega \cdot x}{h} \quad 0 < x < R$$

and the viscosity η is defined as:

$$\eta = \frac{\sigma}{\dot{\gamma}}$$

The discussion above is suitable for Newtonian fluid. For non-Newtonian fluid, it is more complicated. The torque T is given by

$$T = \frac{2\pi R^3}{\dot{\gamma}_R^3} \int_0^{\dot{\gamma}_R} \dot{\gamma}^2 \sigma(\dot{\gamma}) d\dot{\gamma}$$

and the shear stress is given by:

$$\sigma_R = \frac{\sigma_{R,S}}{4}(3 + \frac{d \ln \sigma_{R,S}}{d \ln \dot{\gamma}_R})$$

and the shear rate is given by:

$$\dot{\gamma}_R = \frac{\dot{\gamma}_a}{4}(3 + \frac{d \ln \dot{\gamma}_a}{d \ln \sigma_R})$$

4.1.3 Slip velocity

Slip velocity measurements were conducted with the plate-plate geometry mentioned above. The shear stress σ increased stepwise and exponentially from 10 to 1000 Pa with 30 points in each decade. A waiting time of 30 s per point was set to get a stable signal. Different measuring gap heights, i.e., 1000, 750, 500 and 500 μm are set for the samples to determine the slip velocity, which will be discussed in the section 5.2.2.

4.1.4 Three intervals thixotropic test (3ITT)

The three intervals thixotropic test (3ITT) is used to determine the thixotropic recovery of the sample. 3ITT is performed using the same rheometer set-up as for the flow curve.

In interval 1, the sample is sheared with low shear rate, 1 s^{-1} in this study, for 120 s to get a stable initial viscosity at the low shear rate.

In interval 2, the shear rate is increased to a high value, 500 s^{-1} in this study, for 1 s to simulate the high shear given by the squeegee in the screen printing process. In this interval, the rest structure of the sample is destroyed, and the viscosity decreases dramatically.

In interval 3, the shear rate is reduced to a low value, which is the same as in interval 1. The paste structure recovers due to the cessation of the high shear and the viscosity increases in this interval, simulating the recovery of the pastes after the printing process. In the end, the viscosity reaches an approximately stable value. In certain cases, this "stable" viscosity is much lower than the value in interval 1 because the structure cannot fully recover after the shear. This is true for silver pastes investigated here, but not in general.

Fig. 4.4 shows a typical viscosity curve of a ZnO paste for 3ITT. In this case the viscosity level reached in interval 3 is close to the value obtained in interval 1. Presumably a longer waiting time is required to observe full structure recovery.

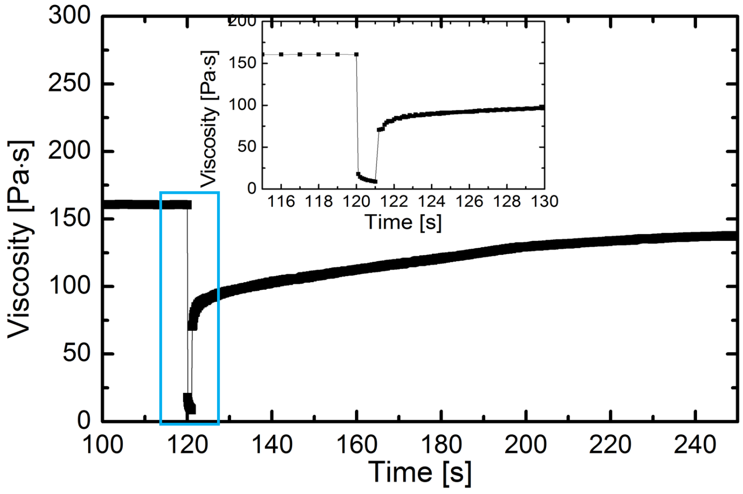

Figure 4.4: Typical viscosity curve in the three intervals thixotropic test with EC 5.5 ZnO model paste.The inserted figure shows the detailed curves in the blue frame. The shear rates are 1, 500 and 1 s^{-1} in the three intervals.

4.1.5 Loss factor $\tan\delta$

Oscillatory measurements were conducted to evaluate the storage modulus G' and loss modulus G'', resulting in the loss factor $\tan\delta = G''/G'$. A small stress amplitude (1 - 100 Pa in this experiment) is applied to the sample with a defined frequency (10 rad/s in this experiment) using a plate-plate geometry ($d_{plate} = 25\,mm$) with a gap of 1 mm at T = 25 °. Within the linear-viscoelastic regime (LVE) storage and loss modulus are independent of the applied oscillation amplitude (either stress or strain). The loss factor $\tan\delta$ in the LVE is compared for different formulations.

4.1.6 Filament stretching test

Filament stretching tests were performed using a Capillary Break-up Elongational Rheometer (CaBER1, Thermo Fisher Scientific) and Fig. 4.5 shows the schematic diagram of this device.

The sample is placed between the upper and bottom plate. Both plates have a diameter of 6 mm. Then the upper plate moves to a specific position, with a pre-set distance from the bottom plate. The distance is named as initial height h_i, which is 1 mm in this experiment The extra sample, which is out of the gap, is trimmed. The sample forms a filament, and it breaks up when the upper plate moves up, with a constant speed of 2 mm/s in this study.

A high-speed camera (Photron FastCam-X1024 PCI) is used to monitor filament deformation and break, with a frame rate of 1000 fps. Fig. 4.6 shows a series of pictures, demonstrating the filament deformation and break-up. The distance between the upper and bottom plates when the break-up happens is determined according to the video/picture taken by the high-speed camera, and the distance is defined as final height h_f. The fracture strain $\varepsilon = (h_f - h_i)/h_i$ is calculated and characterizes the filament stretching property for the pastes.

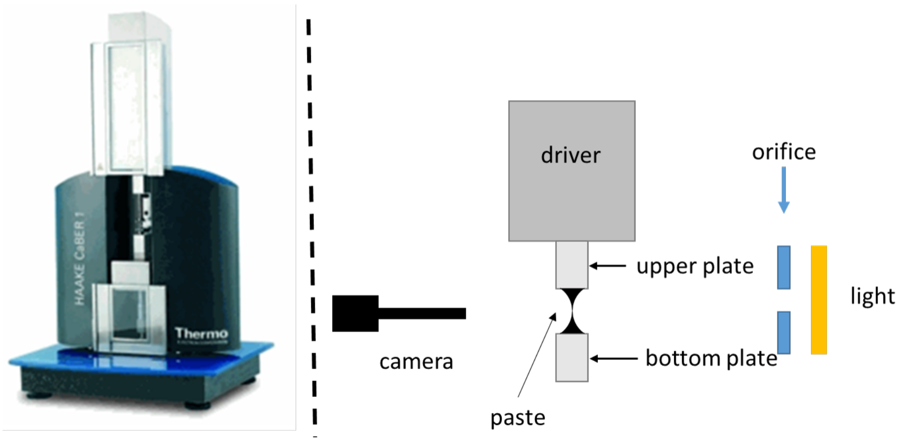

Figure 4.5: Photo (left) and schematic diagram (right) of Capillary Break-up Elongational Rheometer(CaBER).

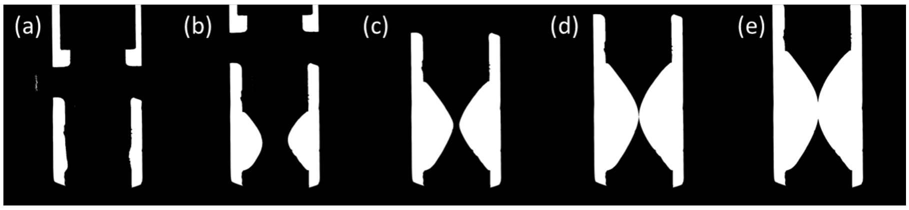

Figure 4.6: The shape change of the sample in the filament stretching test: (a) initial state, (b) and (c) sample stretching and filament deformation, (d) break-up of the filament, (e) after the break-up.

4.2 Screen printing

All pastes in this study were printed with a commercial screen printer (EKRA E2, ASYS Group). Fig. 4.7 schematically shows the printed pattern used in this study. Commercial screens and typical printing parameters were used to simulate the real case, i.e., for front-side silver paste printing.

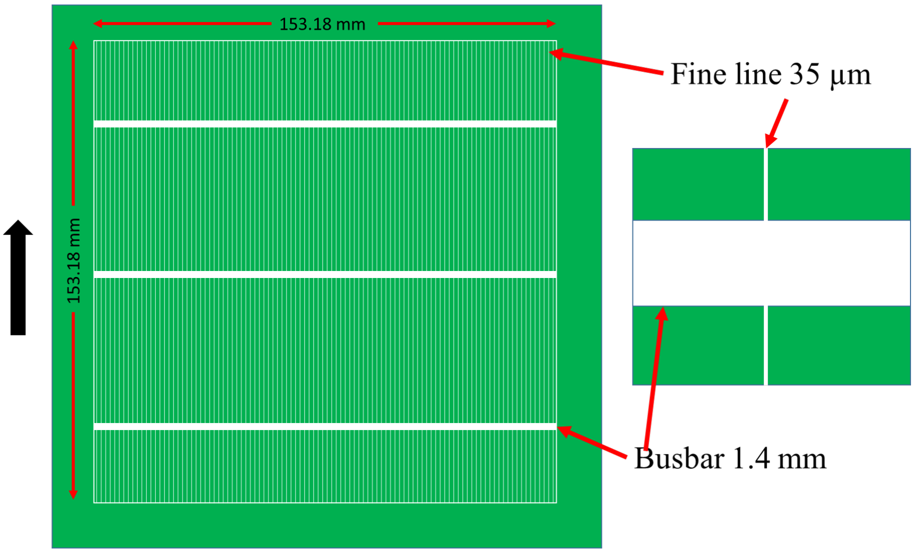

Figure 4.7: Schematic of the screen design. The green part is the area covered by the polymer film and the white area is the screen opening. There are 102 fine lines with constant width of 35 μm and 3 busbars with constant width of 1.4 mm. The black arrow indicates the printing direction. The scheme on the right is a close-up of the intersection between a busbar and a finger line.

Table 4.1: Technical parameters of the screen used in this study

Mesh No.	Thread diameter	Mesh thickness	Mesh tension
360 $l/inch$	16 μm	22 μm	26 $\pm 2N/cm$
EOM	Angle between mesh and fine line opening		
17 μm	30 °		

Table 4.1 to Table 4.3 list the detailed technical parameters of the used screen, the pattern parameters and the printing parameters used in this study. The same

amount of the paste (~150 *g* for silver pastes and ~95 *g* for ZnO pastes) is placed on the screen for each sample.

Table 4.2: Pattern parameters used in this study

Fine line opening	No. of Fine lines	Busbar opening	No. of Busbars
35 μm	102	1.4 mm	3

Table 4.3: Printing parameters used in this study

Printing speed	Flooding speed	Snap-off distance	Pressure	Squeegee angle
300 mm/s	400 mm/s	1.6 mm	75 N/cm	65°

4.3 High-speed camera system

Fig. 4.8(c) illustrates the setup of the screen printing system for high-speed camera investigation. The commercial screen printer was modified by removing the transporting and optical positioning systems and keeping the print head and screen clamping. A high-speed camera (MotionBLITZ EoSens® mini, Mikrotron GmbH) with an objective (Olympus LMPLFLN 10X Objective) was inserted below the substrate to capture motion of the paste, squeegee and screen as well as paste flow at a frame rate of 1,000 fps and resolution of 1,708 × 832 $Pixels$, $\sim$ 0.75 $\mu m/pixel$. The detailed illustration of the set-up is included in the Appendix.

The vacuum table was designed as shown in Fig. 4.8, with an open area in the middle for direct investigation from the bottom. A transparent glass plate (1 mm thickness, window glass), which is strong enough to withstand the squeegee pressure, was placed on the movable substrate table.

The squeegee position was identified by the sharp pattern of the screen on the substrate due to the high pressure acting by the squeegee (see Fig. 4.8(a)). Due to the deformation, the contact between the squeegee and substrate is not a contact line but a contact area with finite width (nip-contact in Fig. 4.8(a)). A similar but less sharp pattern was also observed in the region where the screen was in contact with the substrate due to paste stickiness. The rear end of this pattern is the snap-off point (see Fig. 4.8(b)). The paste was observed by the reflection of the light (black part).

4.3.1 Pre-injection zone and cling zone determination

With the positions of the paste and the squeegee (see Fig. 4.9), the pre-injection zone is determined: the area ahead of the squeegee where the paste is already pushed

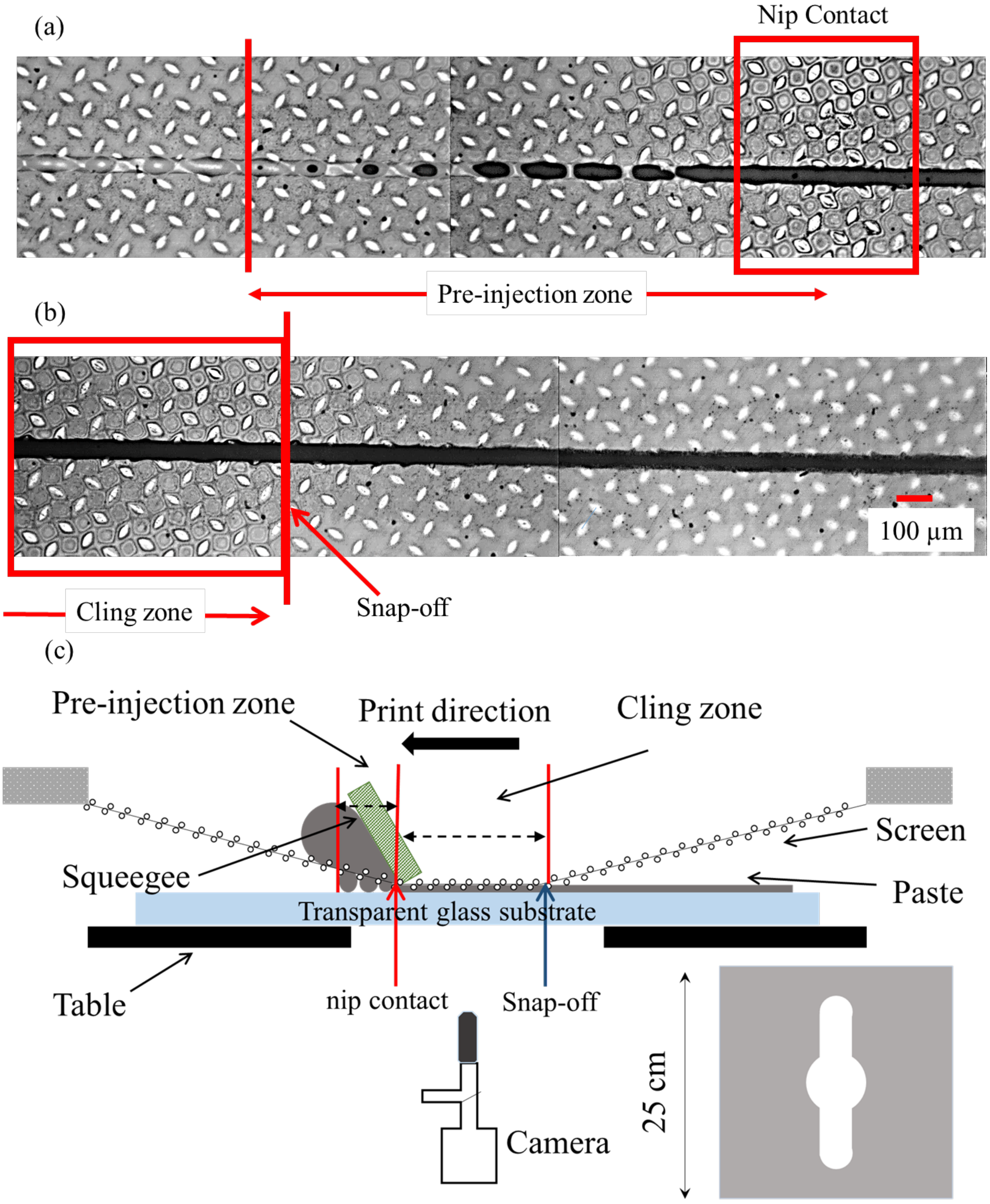

Figure 4.8: . (a) Image of nip-contact and pre-injection zone. The nip-contact (the contact area between the squeegee and screen) is indicated by the pattern in the rectangle. This kind of the pattern is not visible in the left part of the picture. Two pictures have been combined together to show the pre-injection zone. (b) Image of snap-off point. The rectangle indicates the less sharp pattern designating the region were the mesh sticks to the substrate. This kind of the pattern is not visible in the right of the picture. Two pictures have been put together to exemplarily show the difference between the area where the screen contacts the substrate and where the screen has left from the substrate. The boundary indicates the point where the screen loses the contact with the screen. The scale bar applies to both pictures. Both figures (a) and (b) have been processed to increase contrast and sharpness for better visibility. More information (high-speed video imaging series) can be found in the supplementary material. (c) The schematic of the equipment and the design of the vacuum table.

through the screen opening due to the shear stress in the paste roll on the screen p_{screen}. The length of the pre-injection zone is determined by the distance between the 1st paste dot on the substrate and contact point between squeegee and screen (nip-contact). Residual paste remains on the screen after the first printing cycle and deteriorates the determination of the pre-injection zone length. Therefore, only the data observed in the 1st print cycle is collected with a clean screen. With the nip-contact and snap-off point, the cling zone is determined (see Fig. 4.10).

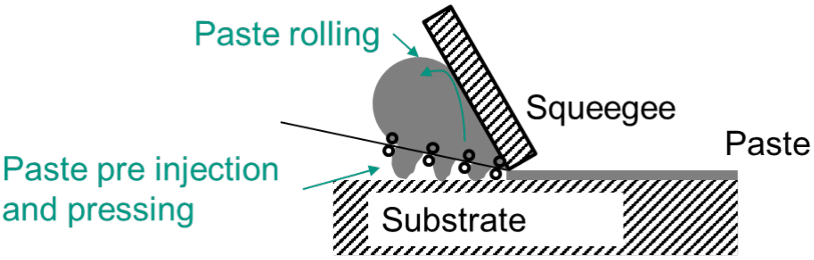

Figure 4.9: Schematic diagram of pre-injection zone.

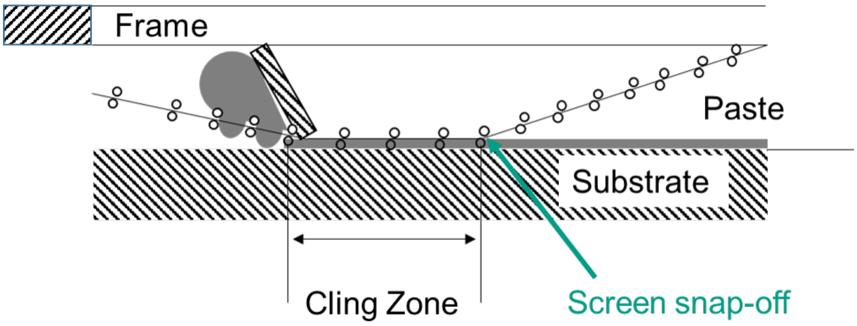

Figure 4.10: Schematic diagram of cling zone.

4.3.2 Paste spreading determination

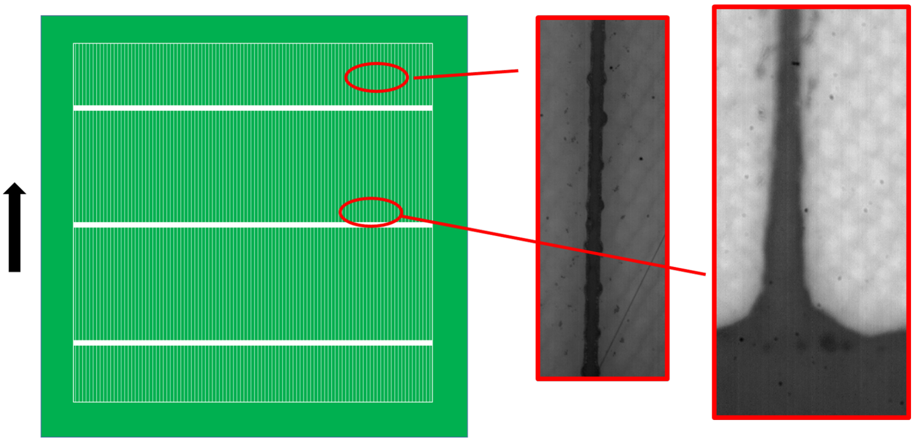

Figure 4.11: Two kinds of positions for the high-speed camera observation:(a) fine line area, (b) connection point between fine line and busbar.

Paste spreading has been investigated by observing paste covered areas over time. The printed electrode geometry is influenced by the screen opening direction [53]. Therefore, two different positions were observed (see Fig. 4.11): the busbar/finger connection area, with screen opening perpendicular to the printing direction, and a fine line area, with screen opening parallel to the printing direction.

After the investigation of the printing process using the high-speed camera, the pastes were screen printed onto monocrystalline silicon wafers, for printed electrode width determination using a 3D light microscope (VHX-600, Keyence Corp., Neu-Isenburg, Germany).

Chapter 5

Results and discussion

5.1 Heat activation of thixotropic agent

As mentioned above, the thixotropic agent forms 3D structure in the formulation after the activation at high shear and high temperature.

Fig. 5.1 shows a CLSM picture of a sample with incomplete activation. The black part is the solvent and the red part is the thixotropic agent fiber. According to the picture, the shape of the particles is still kept. The incomplete activation due to the low temperature allows a thixotropic agent particle swelling but not interact with the other particles to form the 3D structure through the sample.

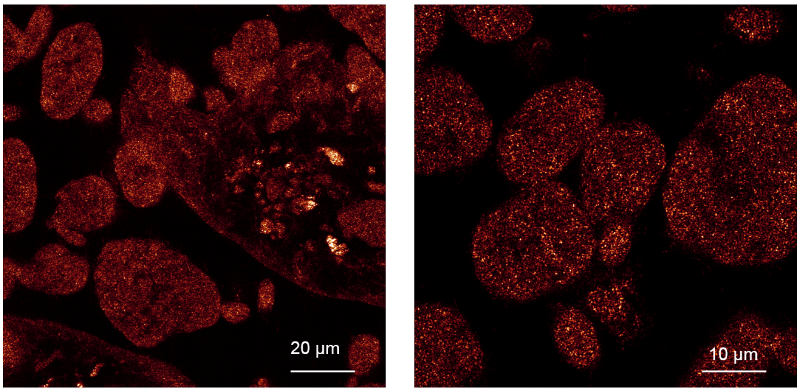

Figure 5.1: CLSM picture of activated Thixatrol Max in Texanol (8 $wt\%$) at $50°C$.

Fig. 5.2 shows a CLSM picture of a sample with a better activation. Although there is still some aggregates, there is no obvious boundary among the particles. All particles swell and overlap with the other particles, forming a continuous 3D structure through the sample.

With higher activation temperature, there are some needle-like structures (see Fig. 5.3). Excessively high activation temperature causes partial solubilization and precipitation after cooling. The precipitation leads to some small particles, resulting in the loss of the 3D structure.

The flow curve indicates with the same concentration, good activation results in

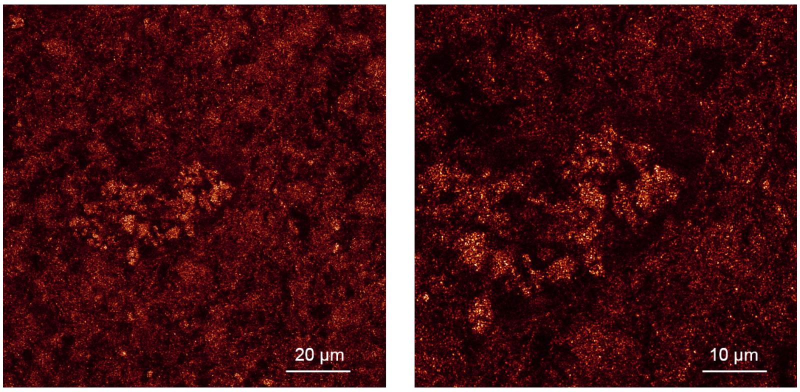

Figure 5.2: CLSM picture of activated Thixatrol Max in Texanol (8 $wt\%$) at $65°C$.

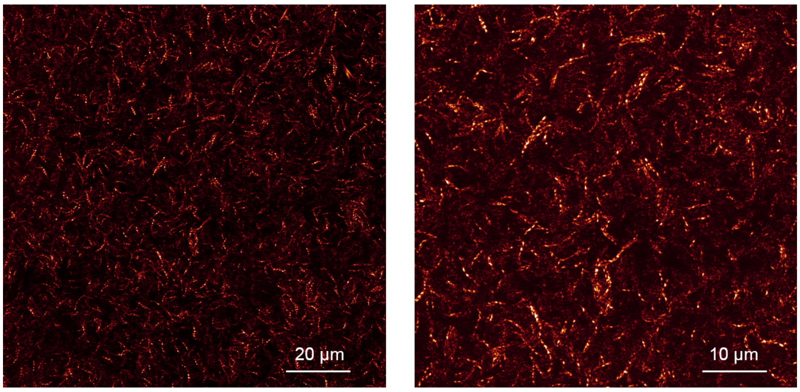

Figure 5.3: CLSM picture of activated Thixatrol Max in Texanol (8 $wt\%$) at $75°C$.

a higher viscosity, due to the strong 3D network formed through the liquid phase (see Fig. 5.4). Therefore, with the optimized activation parameters, it is able to achieve the required performance, i.e., higher absolute viscosity and faster recovery, with minimum concentration of thixotropic agent, leaving the space for the other additives in the formulation. According to the flow curves, the optimal temperature for Thixatrol Max and Thixatrol ST in Texanol are fixed at 65 and 55 $°C$, respectively.

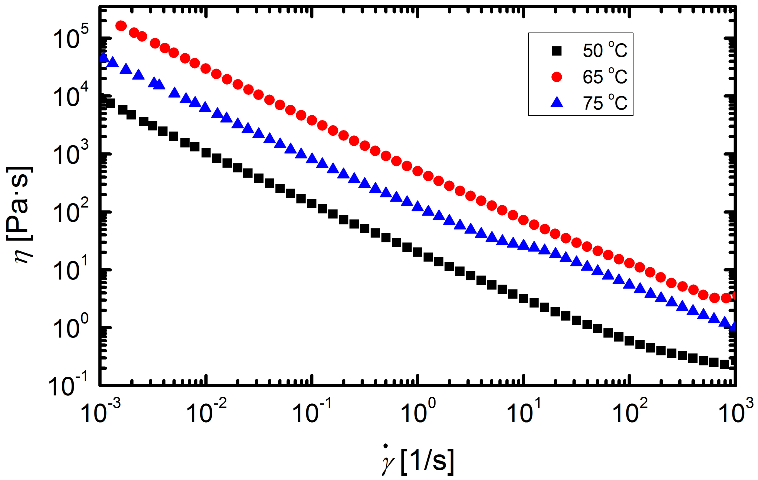

Figure 5.4: Flow curves of 3 activated Thixatrol Max in Texanol (8 $wt\%$) gels.

5.2 Wall slip investigation with silver pastes

The following section focuses on the influence of wall slip effect on screen printing process. The model system used for this part is silver paste without glass frits. Glass frits form the electric contact between the electrodes and the wafers during firing [24, 54, 55]. The reason why the glass frit is not included in the model system is that compared with the silver particles, the volume fraction of the glass frit is very low, about 5%. Meanwhile, the particle size of the glass frit is normally similar to the silver particle in commercial formulations.

In this study, only the rheological properties rather than the chemical properties of the model system are discussed. Therefore, the missing of the glass frit is negligible. The wall slip effect is varied by replacing the solvent Texanol by triacetin, the slip agent. The rheological characterization is discussed in section 5.2.2 and followed by the influence on the geometry of printed electrodes in section 5.2.3. This part described in the following sections has been published in *IEEE Journal of Photovoltaics* [56].

5.2.1 Solvents immiscibility

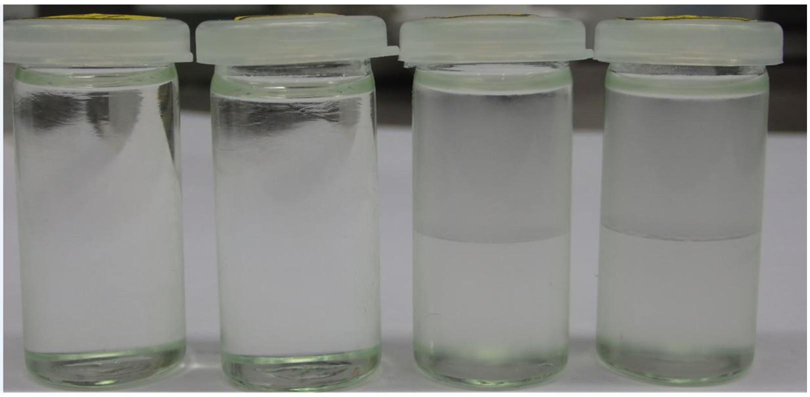

	Mixture 1	Mixture 2	Mixture 3	Mixture 4
PSMA Solution [*wt%*]	4.10	4.10	4.10	4.10
Texanol [*wt%*]	5.00	4.60	4.30	4.00
Triacetin [*wt%*]	0.00	0.40	0.70	1.00

Figure 5.5: Phase separation of the liquid mixture. The weight concentrations of the ingredients are the absolute value in the paste formulation. Therefore the sum of the values is not 100 %. Mixture 3 and Mixture 4 show clear two phases.

The triacetin is introduced to change wall slip behavior significantly. According to Fig. 5.5, the mixtures are homogeneous with the triacetin concentration lower than 0.4 $wt\%$. Phase separation occurs above a triacetin concentration of 0.7 $wt\%$. This phase separation indicates the instability of the mixture system and also the paste. This kind of instability will influence the storage stability which is important for commercial applications. However, this is out of the target of this work.

5.2.2 Rheological characterization

Viscosity of Vehicles

Both of the viscosities of Texanol (13.5 $mPas$) and triacetin (23 $mPas$) are very low compared with the PSMA solutions. Therefore, although with different formulations, all vehicles show the same viscosity $\eta = 0.13$ Pas in the high shear stress range $\sigma\ > 350$ Pa (Fig. 5.6). This data is used to calculate the slip layer thickness.

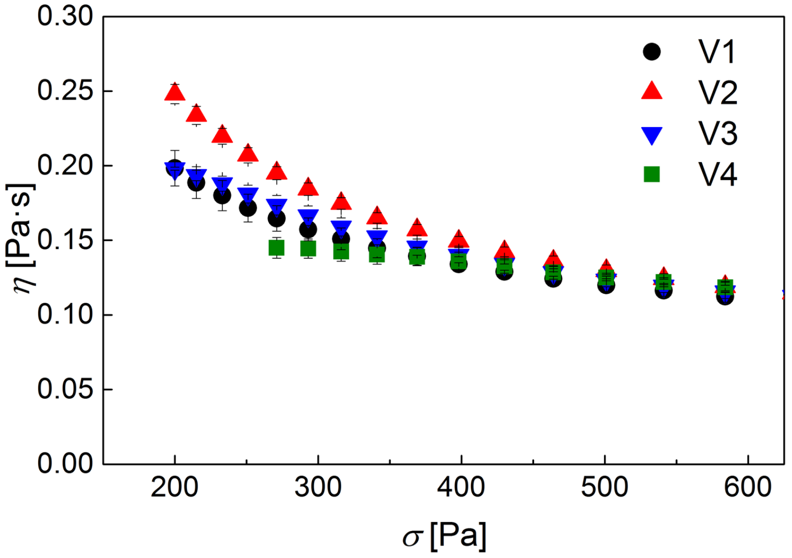

Figure 5.6: The viscosity of vehicles for all pastes.

Yield stress

The yield stresses of the pastes are measured with vane-in-cup geometry as described above in Section 4.1.1. The pastes P1 - P3 have similar yield stress ~ 450 Pa. In contrast, P4 with V4 exhibits a higher value. Table 5.1 lists the detailed yield stress data for all pastes.

Table 5.1: Yield stress of the four pastes

	P1	**P2**	**P3**	**P4**
σ_y [Pa]	474±18	430±34	452±8	588±23

Slip velocity

Slip velocity measurements were conducted as described in Section 5.2.2. Fig. 5.7 shows the change of rotation speed n with increasing shear stress σ for sample P4 at a gap size of 1000 μm using a stainless steel plate and a capillary film covered plate.

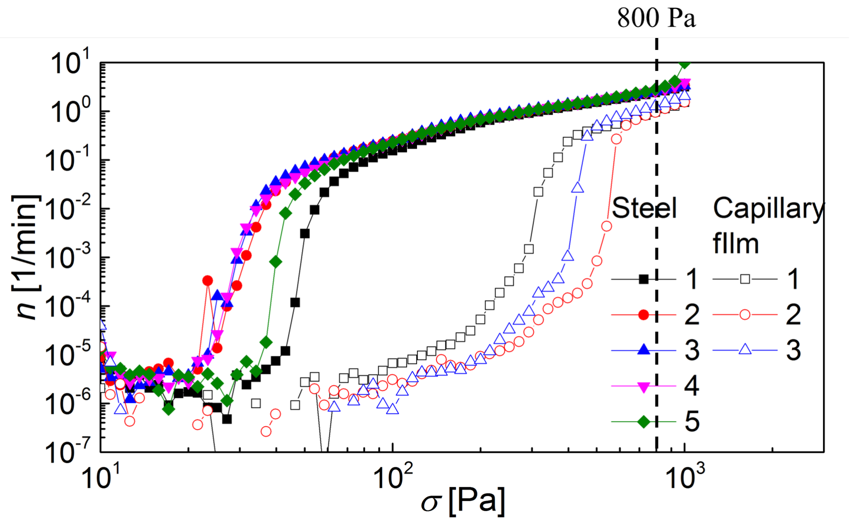

Figure 5.7: Rotation speed versus shear stress for paste P4 measured with plate-plate geometry (stainless steel plate (solid points) and a capillary film (cutted from the original screen) covered plate (open points) at a gap size of 1 mm [56]. Different symbols refer to different measurements using a fresh gap filling. Similar results were obtained for the other pastes.

With the stainless steel plate, the rotation speed n increased by several orders of magnitude between 20 and 80 Pa and then almost linearly between 80 and 800 Pa. For $\sigma > 800$ Pa, n increased dramatically due to spillage.

The onset of the initial steep increase in rotation speed n is poorly reproducible with substantial scatter between different measurements, which may be related to inhomogeneity of the interface between sample and plate and depend on sample filling into the gap. However, this aspect is out of the scope of this study. Afterward, n increases linearly in a reproducible manner.

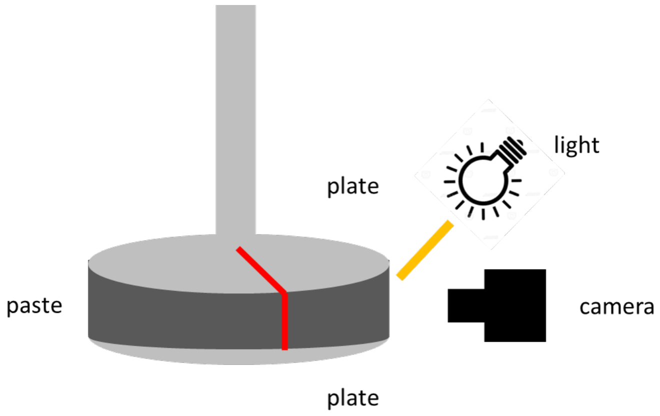

Figure 5.8: The experiment setting for observation of the wall slip phenomena and the shear profile of the sample between plates.

The video snapshots (see Fig. 5.9), taken using the setting shown in Fig. 5.8, reveal the movement of P4 referring to test 1 with steel plate (black solid dots) in Fig. 5.7. By comparing the position of the red line, no movement of the upper plate was visible below 50 Pa. The sharp increase of the rotation speed set in at a critical slip stress $\sigma_s \approx 50$ Pa. Above this value, the upper plate was moving. However, the 1000-μm-thick paste layer was essentially not deformed. Between 50 and 600 Pa, only a thin paste layer adjacent to the smooth upper plate was sheared. Similar observations have been reported earlier for microgel paste [57, 58]. Between 600 and 800 Pa, a second thin layer was sheared next to the lower plate but with much lower speed than at the upper interface. For $\sigma > 800$ Pa, the sample was ejected from the gap.

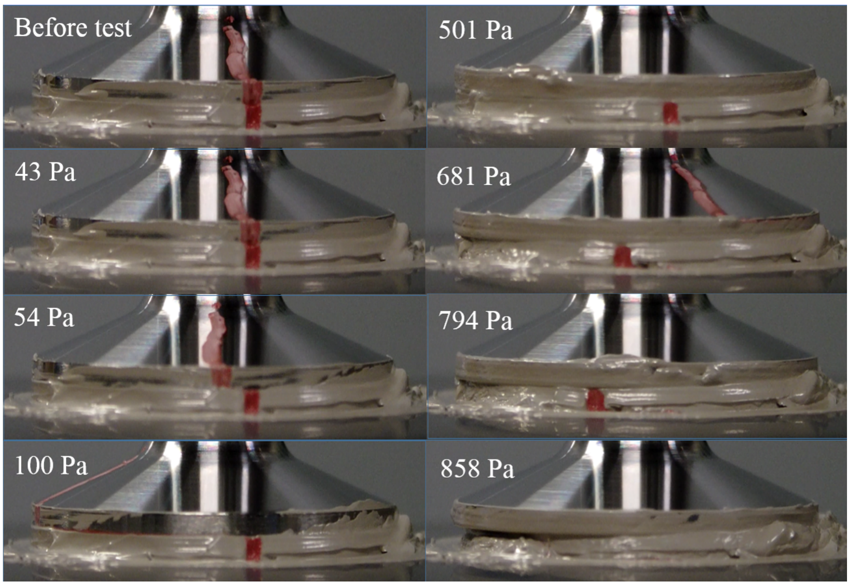

Figure 5.9: Video snapshots of silver paste P4 in the gap during the measurement with plate-plate geometry and a gap size of 1 mm [56].

Hence, the following discussion will be restricted to the shear stress range between 200 and 600 Pa, in which only a thin layer at the interface between the sample and the upper plate is sheared.

Based on the observation in Fig. 5.9, the slip velocity v at the rim of the plate is given by the rotation speed n and the plate radius R:

$$v = 2n\pi R$$

According to the video snapshots, slip dominates the deformation between 200 and 600 Pa, before paste spillage. For all pastes, the slip velocity increases linearly with shear stress, but it is independent of the gap in the investigated range between 0.25 and 1.00 mm. Fig 5.10 shows the slip velocity v versus shear stress σ in different gaps for all four pastes. Almost all data points overlap with each other for specific paste under specific shear stress. This phenomenon confirms that the wall slip dominates the shear profile inside the measuring gaps .

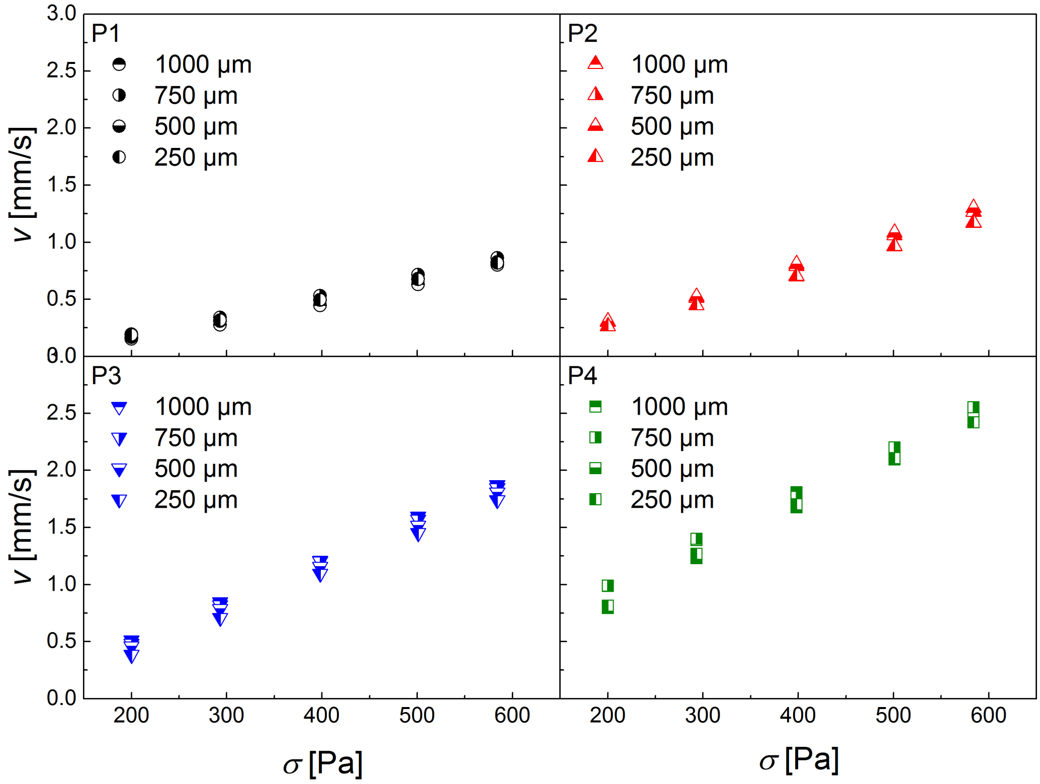

Figure 5.10: Slip velocity measured with gaps between 0.25 to 1 mm for all pastes. For all four pastes, the slip velocity is linearly increased with shear stress but almost independent of the gap size.

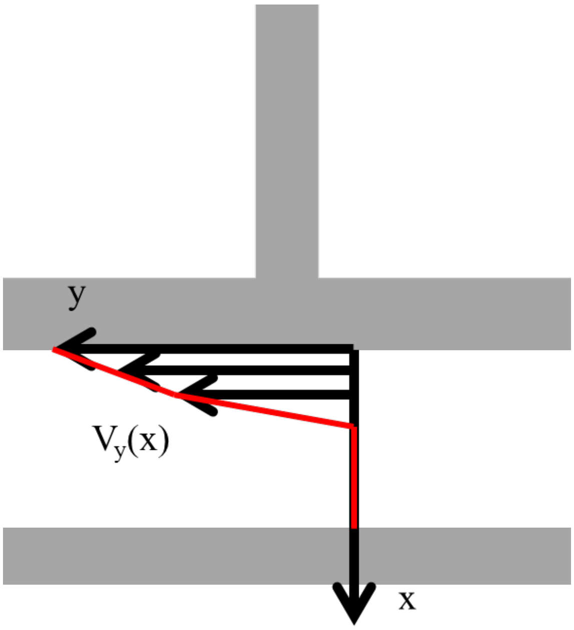

Figure 5.11: Schematic shear profile in the gap when there is wall slip. x indicates the distance from the upper plate, where $0 < x < H$, H is the gap size. The $v_y(x)$ indicates paste movement velocity to the y direction where $0 < v_y(x) < v_{upper\ plate}$. When the wall slip happens, only a few layer of the paste next to the upper plate moves but the rest paste remains stationary.

At given stress, the slip velocity increases from P1 to P4 by about a factor of 4, apparently due to the variation in solvent composition (Fig. 5.12).

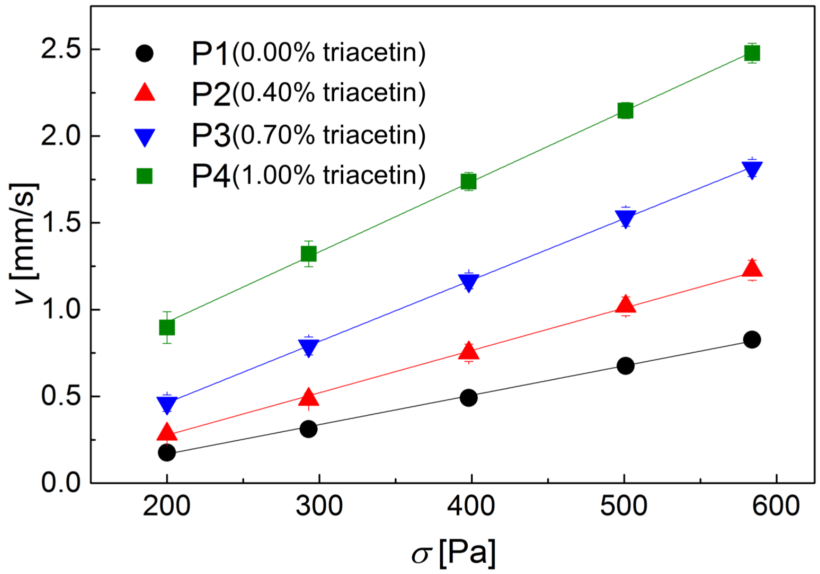

Figure 5.12: Average slip velocities for P1 - P4 with different concentration of triacetin calculated from measurements at different gap sizes between 0.25 and 1 mm. Lines are indicated to guide the eyes.

Wall slip in suspensions is related to solid migration and a thin liquid film forms between the solids and adjacent wall [59–61]. The thickness of the corresponding slip layer δ_{slip} depleted by particles can be calculated as $\delta_{slip} = \eta_s \cdot v(\sigma)/\sigma$, where η_s is the viscosity of solvent (here, the viscosity of the vehicle should be used), $v(\sigma)$ is the slip velocity, and σ is the applied shear stress [62]. Due to the linear relation between $v(\sigma)$ and σ and similar viscosity η_s for the used vehicles, the slip layer thickness increases by a factor of 4 from P1 to P4 (see Fig. 5.13). Typical values are between 0.1 and 1 μm, which is less than the diameter of the used silver particles.

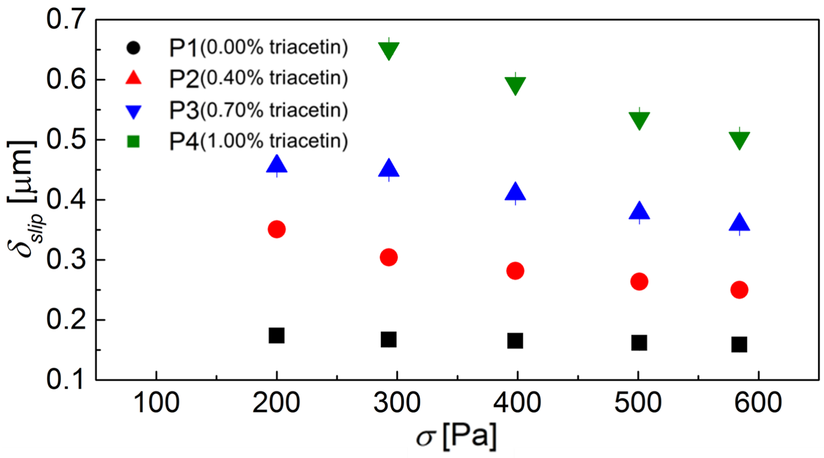

Figure 5.13: Calculated slip layer thickness for P1 to P4.

As mentioned above, the screen includes the steel mesh and the polymer capillary film. Therefore, it is essential to consider the contact between the paste and the mentioned two components during the screen printing process. Slip measurements were performed with a capillary film covered plate in order to mimic this process. The capillary film was attached to the rheometer plate using a double-sided adhesive tape. The capillary film roughness is about 0.5 μm, which is much smaller than the selected gap size. Zero position calibration is done before each measurement. Thus, the systematic error inferred from the capillary film attachment is similar for all measurements. Finally, the slip velocity is independent of gap size, as shown in Fig. 5.12. Hence, the uncertainty brought about by the capillary film attachment seems to be negligible. Rotation speed data exemplarily demonstrated for sample P4 in Fig. 5.7 reveals that the critical stress for the onset of slip σ_s shifts to higher values by about one order of magnitude. Similar results have been observed for the other three pastes, as shown in Table 5.2.

Table 5.2: Critical stresses for onset of slip on steel and capillary film covered plates

σ_s [Pa]	**P1**	**P2**	**P3**	**P4**
Steel	26±5	22±1	30±7	41±20
Capillary film	227±26	244±11	258±31	369±29

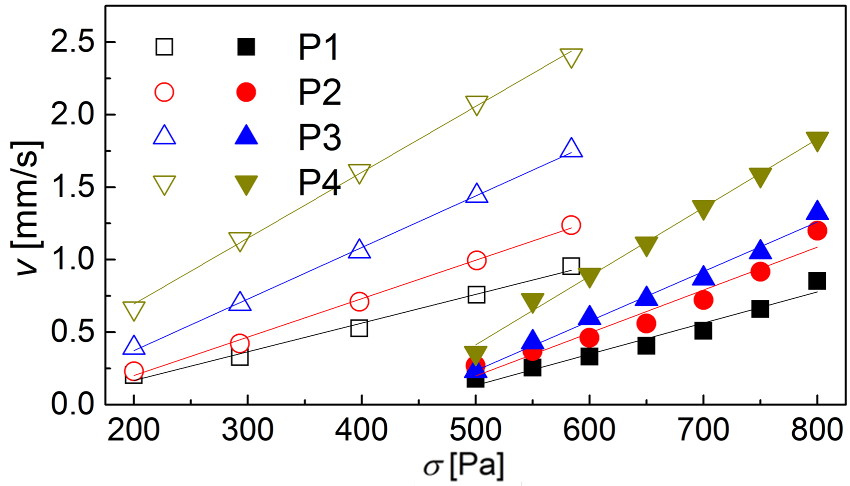

Figure 5.14: Slip velocities for all four pastes measured with the stainless steel plate (open points) and the capillary film covered plate (solid point) at a gap size of 0.05 mm. The lines are to guide the eyes.[56]

The screen opening for front-side silver paste is less than 50 μm in the up-to-date manufacturing process. Hence, slip velocities were measured at 50 μm gap size, as shown in Fig. 5.14. The results agree with those shown in Fig. 5.12, confirming that the slip occurs irrespective of gap size. With the capillary film covered plate, the slip velocity is substantially reduced compared with the smooth plate, but again increases linearly with σ . This reduction is not related to the roughness of the surfaces, which is about 0.5 μm in both cases. Therefore, the observed difference is supposed to attributed by the different wetting behavior similar as discussed in [63].

Both Texanol and triacetin wet the steel surface almost completely (stable contact angle $\theta < 5°$), whereas the stable contact angle on the capillary film surface is $\theta \approx 15°$. With better wetting, it is easier to form thin liquid film at the interface. For a given paste, the slope v/σ keeps the same in contact with capillary film as well as steel. At a given stress σ, the slip velocity increases from P1 to P4, similar as found in contact with the steel plate. Apparently, the variation of the solvent mixture determines the formation of the slip layer depleted from particles. It is probably due to the changing of steric stabilization of the particles when two kinds of immiscible solvents exist.

5.2.3 Printed electrode geometry

Silver deposits

Each paste was continuously printed with 13 polycrystalline silicon (poly-Si) wafers, provided by Haocheng Ltd. (Changzhou, China) to reach stable conditions on the screen. The 14th poly-Si wafer was weighed before and after printing to get the deposit on the wafer. The 15th poly-Si wafer was dried after printing for geometry characterization. The 16th and 17th wafers were monocrystalline silicon (mono-Si) wafers. The next mono-Si wafer (18th) was also weighed to get the deposit. The last mono-Si wafer (19th) was dried after printing for geometry characterization.

The deposit reflects the interaction/adhesion between the paste and screen. Less adhesion reduces the resistance when the paste is pushed through the screen opening, resulting in a higher deposit. With increasing amount of triacetin, the silver deposit increases by about 30 % from P1 to P4, on both poly- and mono- silicon wafers (Table 5.3). Although with different solvents components, the densities keep almost the same value (Table 5.3). Therefore, the change of the deposits corresponds to the increased volume of pastes, responding reduced adhesion between paste and screen. Similar results have been obtained for solder pastes [12, 13]. For these pastes higher slip velocity between the solder paste and stencil reduced the residual paste on the stencil and improved the deposits.

Table 5.3: Silver deposits on mono- and poly- silicon wafers

	P1	**P2**	**P3**	**P4**
Deposit on Mono- silicon wafer (mg)	104	108	116	131
Deposit on Poly- silicon wafer (mg)	102	109	115	134
Density (g/cm^3)	5.11	5.08	5.10	5.09

Optical image of screens after printing

The reason for higher deposit discussed above is confirmed by visual inspection of the screen after printing. By comparing the clean screen and screen after printing, the stuck residual pastes is reflected by the different diameters of the steel wires in the busbar area. The amount of paste sticking to the screen decreases from P1 to P4, and there is almost no paste sticking after printing with paste P4, which can be qualitatively revealed by the images shown in Fig. 5.15. Ekere *et al.* found similar differences among solder pastes during stencil printing [12, 13].

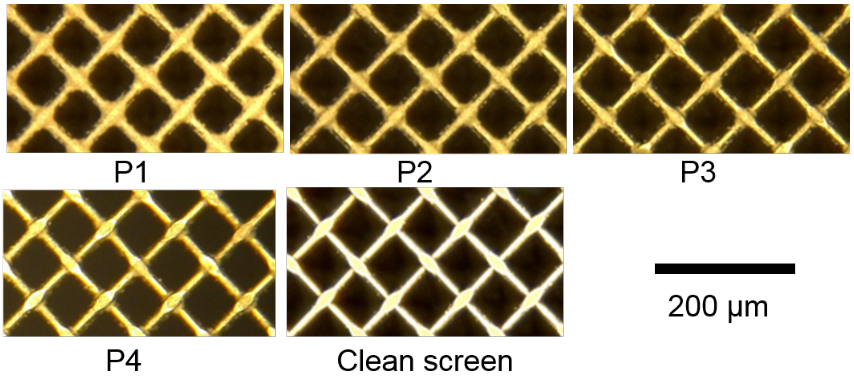

Figure 5.15: The pictures of the screen after printing with different pastes.

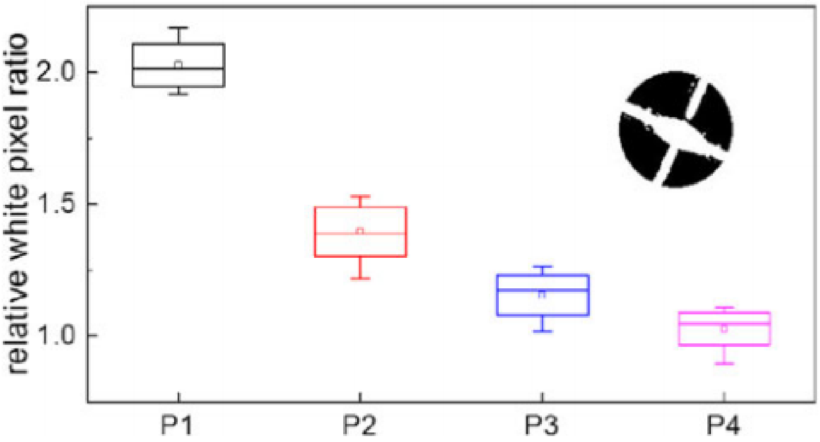

Figure 5.16: Relative white pixel ratio analysis of the pastes stuck on the screen. The inserted picture illustrates the conversion of a microscopic view of a wire crossover into a binary picture for pixel counting.

For quantitative analysis, the color pictures were transferred to binary data using the commercial software ImageJ [64, 65]. The white areas shown in the insert of Fig. 5.16 correspond to the cross point of steel wires with the adhering paste. 20 pictures like the circle in Fig. 5.16 were chosen from the binary pictures, and the white pixels in the circle were counted.

Relative white pixel ratio is calculated by the white pixels counted from the screen printed with pastes over the white pixels counted from the clean screen. It indicates that paste was adhering on screen dramatically reduces from P1 to P4. The authors attributes the increasing silver deposit and corresponding decrease of the paste residual on the screen to the rising slip velocity.

Optical image of connections between fingers and busbar

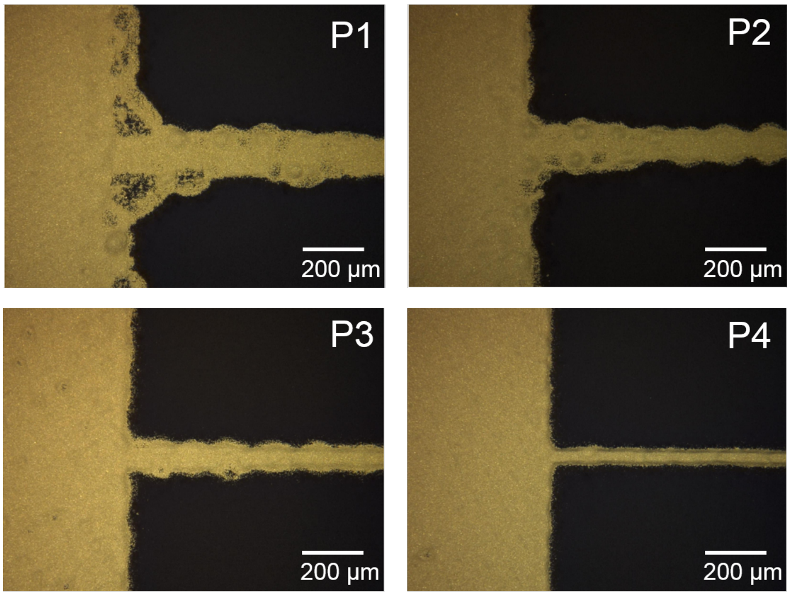

Figure 5.17: Connections between fingers and busbar on mono-crystalline wafers for P1-P4. The print direction is from left to right [56].

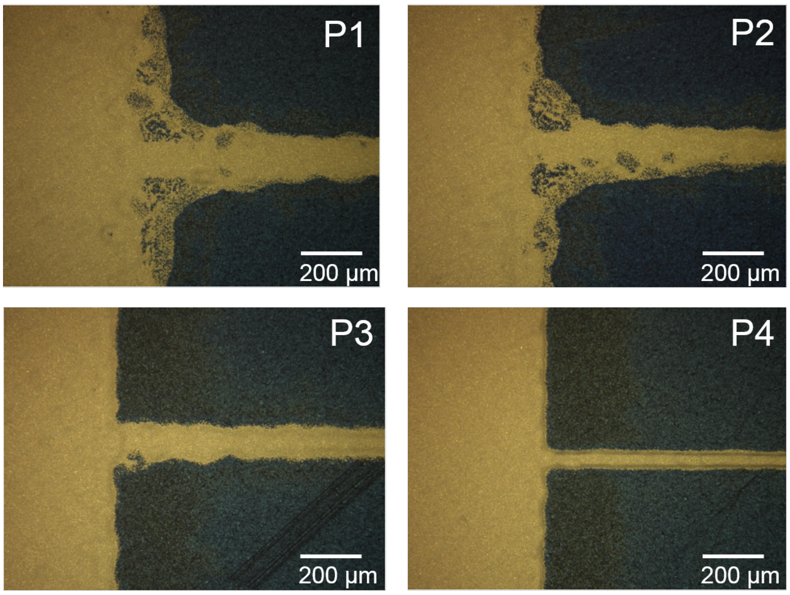

Figure 5.18: Connections between fingers and busbar on poly-crystalline wafers for P1-P4. The print direction is from left to right.

The orientation of the busbars is perpendicular to the printing direction. The paste spreads and forms different patterns due to this perpendicular alignment [53].

The quality of connections between the fingers and busbar affects the cell efficiency by influencing the short-circuit current j_{SC} and fill factor FF [66].

Fig. 5.17 and Fig. 5.18 illustrate the connection quality between fine electrodes and busbars on mono- and poly-Si wafers, respectively. Quality and shape accuracy improve from P1 to P4 and seem to relate to the adhering paste on the screen. With less adhering paste on the screen, the boundary of the connections point is cleaner, i.e., less smeared area. The reduced smeared area facilitates sunlight reception and should result in an increased short-circuit current j_{SC}.

Line width, height and cross section

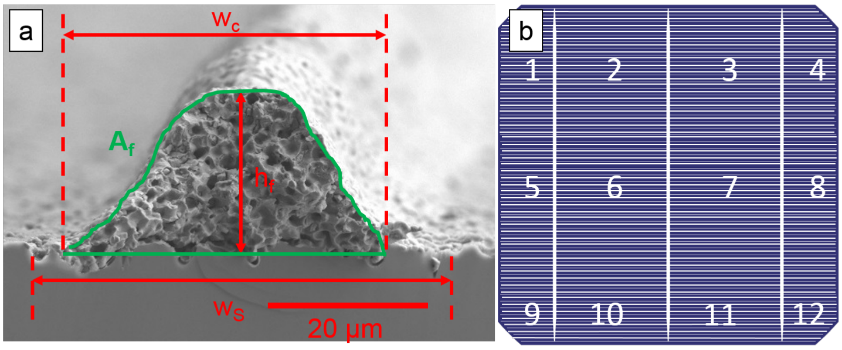

Figure 5.19: (a) Description of parameters of printed electrode geometry. (b) Positions of the recorded electrode geometry on the wafer surface [56].

Several parameters of printed electrode geometry are compared for the four pastes, including shaded electrode width w_S, conductive electrode width w_C, electrode height h_f, electrode cross section A_f, and aspect ratio AR, defined as described in [66]. A typical electrode-cross section is shown in Fig. 5.19(a). Electrode geometry at 12 different positions, as indicated in Fig. 5.19(b), was measured. Because the pressure distribution and screen tension force are different due to the different location of the printing squeegee, the selected points were distributed on the whole wafer guarantee the results statistically. Six pictures per position of adjacent electrode sections with an area of 260 $\mu m \times 331$ μm were taken.

For each picture, two kinds of modes are taken. The 3-D information of a height profile (see Fig. 5.20(a)) is formed by scanning the sample layer by layer. The 2-D information of a reflection profile (see Fig. 5.20(b)) is formed by collecting the light reflected by silver particles. The resolution is 0.48 μm on the $x-$ and $y-$ scales. As analyzed by the software, the data points were filtered and used for w_s , w_c, h_f, A_f, and AR for the next steps.

The conductive electrode width w_C represents the part of a printed electrode with higher height than the surface roughness of the substrate. This part of the electrode contributes to the electrical conductivity. The shaded electrode width w_S represents the area covered by the electrodes. The analysis software converts

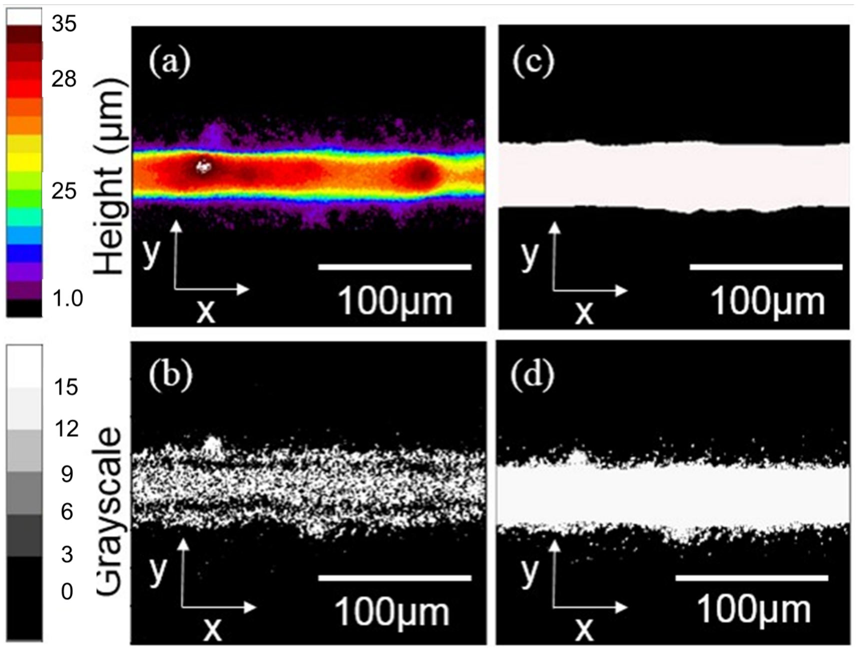

Figure 5.20: (a) Original height profile data, (b) original data of reflected light in grayscale, (c) height data filtered by software for calculation of conductive line width w_c, and (d) grayscale data filtered for calculation of shaded line width w_s of one line section of a wafer printed with paste P4 [56].

the original data into binary data as illustrated in Fig. 5.20 for calculation. The electrode height h_f is detected from the height scan mode pictures by selecting the highest point for each cross section. The cross-section A_f is also calculated based on the height scan mode pictures by integrating the area between the baseline and the height profile as indicated in Fig. 5.19(a). AR is calculated as h_f/w_C using their average values from the boxplot in Fig. 5.22.

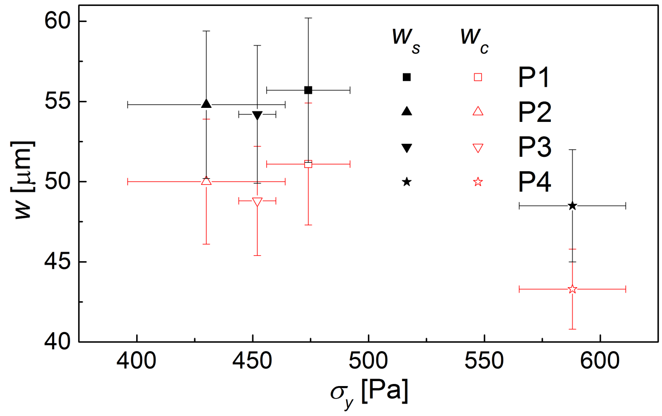

Figure 5.21: Relation between electrodes widths (w_S and w_C) and yield stress. [56].

The parameters w_S and w_C are depicted in Fig. 5.21. P4 shows narrowest w_S and w_C , whereas these values are very similar for the other three pastes. This indicates that electrode width is tightly related to the yield stress of the corresponding paste, since the yield stress of paste P4 is significantly higher than that of the other three pastes.

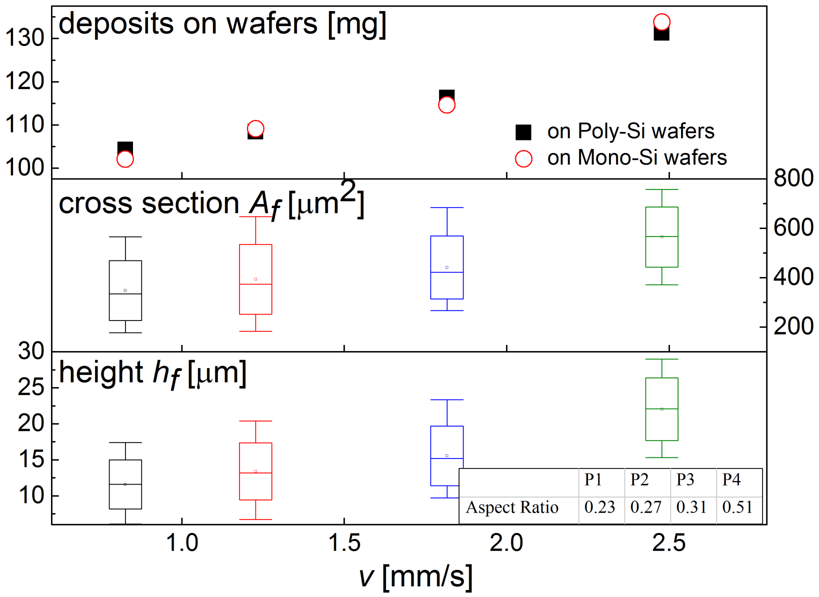

Figure 5.22: Deposit, electrode cross section, height, and aspect ratio versus characteristic slip velocity. The slip velocity was measured with a steel plate at the shear stress of 598 Pa. Corresponding data are shown in Fig. 5.12 [56].

The values for the parameters h_f, A_f, and AR of the investigated electrodes are shown in Fig. 5.22. h_f and A_f increase with slip velocity (from P1 to P4), mainly due to higher deposits. Higher h_f and A_f should enable lower series resistance when printing with narrower screen opening. Finally, high h_f and low w_C result in a higher ratio AR, and accordingly, this parameter increases substantially from P1 to P4.

In summary, the characterization of the screen-printed electrode geometry revealed significant differences concerning electrode widths w_S and w_C, height h_f, cross-sectional area A_f, and aspect ratio AR. These parameters are directly related to the pastes' yield stress (w_S, w_C) and particularly to the adhesion or slip in contact with the screen (h_f, A_f) controlling the paste deposit. Consequently, AR is related to yield stress as well as slip.

5.2.4 Theoretical calculation of the relative impact of the parameters

The short-circuit current j_{SC} and the fill factor FF are influenced by the shaded area and grid resistance. The influence of these two parameters can be estimated based on the corresponding values for the shaded electrode width and cross section with the equations mentioned in [66]. The properties of the busbars (width, height, and specific resistance) are assumed equal for all pastes.

The metallized fraction on the wafer, $A_{met,grid}$, can be calculated using the shaded electrode width w_S along the finger direction:

$$A_{met,grid}[\%] = A_{met,f}[\%] + A_{met,BB}[\%] = ((\frac{w_s}{P} - \frac{w_s \cdot n_{BB} \cdot w_{BB}}{w_{wafer} \cdot P}) + (\frac{w_{BB} \cdot n_{BB}}{l_{wafer}})) \cdot 100$$

where $A_{met,f}$ and $A_{met,BB}$ are the metallized fraction on the wafer covered by fingers and busbars, respectively. w_{wafer} and l_{wafer} are the width and length of the silicon wafers, i.e., 156 mm in this study. P is the distance between two parallel fingers, which can be calculated by the size of the wafer and the finger numbers listed in Table 4.2. n_{BB} and w_{BB} are the number and width of busbars which are also listed in Table 4.2.

Table 5.4: Theoretical calculation of the relative impact due to the geometrical parameters

	P1	**P2**	**P3**	**P4**
w_s $[\mu m[$	55.74	54.81	54.24	48.48
A_f $[\mu m^2[$	347.86	393.83	441.51	564.94
h_f $[\mu m[$	11.59	13.41	15.55	22.03
AR	0.23	0.27	0.31	0.51
$A_{met,grid}$ $[\%[$	5.59	5.53	5.49	5.11
$\Delta j_{sc,grid}$ $[mA/cm^2[$	2.24	2.21	2.20	2.05
R_L $[\Omega/m[$	81.82	72.95	61.95	47.04
$\Delta r_{s,grid}$ $[\Omega \cdot cm^2[$	0.27	0.24	0.20	0.15
ΔFF_{grid} $[\%abs[$	1.52	1.36	1.15	0.88

Total current density loss due to the grid, $\Delta j_{sc,grid} = j_{ph} \cdot A_{met,grid}$, is estimated assuming the photon-generated current j_{ph} is 40 mA/cm^2.

Assuming a specific line resistance $\rho = 2.5$ $\mu\Omega{\cdot}cm$, the line resistance $R_L = \rho/A_f$ is calculated, using original cross-sectional data varying along the line direction. Series resistance $\Delta r_{s,grid} = 1/3 \cdot R_L \cdot l_{wafer} \cdot (l_{wafer} + 0.5 \cdot w_{BB}) \cdot P$ and fill factor loss $\Delta FF_{grid} = 5.7 \cdot \Delta r_{s,grid}[\%]$ are also calculated correspondingly.

All the data are summarized in Table 5.4.

In conclusion, the calculated $\Delta j_{sc,grid}$ is lower for a wafer metallized with paste P4 than for a wafer with paste P1 - P3, and this is attributed to P4's higher yield stress. The calculated loss in fill factor ΔFF_{grid} decreases monotonically from P1 to P4, *i.e.*, with increasing slip velocity of the pastes. The lower loss of these two parameters indicates a higher efficiency when printing with P4.

This study proves the adding of a kind of solvent, which is partially immiscible with the main solvent in the formulation, could reduce the amount of adherent paste on the screen after printing process. Relevant rheolgoical item, slip velocity, can be measured with rotational rheometer. This study provides a strategy of formulation design for the industry. A solvent/liquid with lower surface tension could reduce the adherent phenomena further theoretically. Therefore, silicon oil could be tested in the next step.

5.3 High-speed camera investigation with ZnO pastes

The following section focuses on the influence of rheological properties on screen printing process, investigated by a high-speed camera. The model system used in this section is ZnO pastes.

ZnO pastes have been selected here not only because of their technical relevance in printed electronics. These pastes also have well-defined, conventionally accessible rheological properties, enabling straightforward correlating to printing performance. In contrast, rheological characterization of silver pastes, e.g., used for front side metallization of Si-solar cells, can be very challenging due to wall slip and spillage phenomena occurring during the rheological testing [67]. Moreover, wall slip can play a critical role in screen printing , i.e., increase the deposit, depending on continuous phase composition subtly. And wetting phenomena on different kinds of substrate could determine the paste spreading. The model ZnO pastes prepared here are not prone to wall slip on the investigated length scale, eliminating the discussion of the complexity brought by wall slip. This part described in the following sections has been published in *Journal of Coating Technology and Research* [68].

5.3.1 Rheological characterization

Yield stress

All investigated pastes exhibit an apparent yield stress σ_y, i.e., the minimum stress required to force the pastes to flow. Stress ramp experiment covering the shear stress range from 10 to 10,000 Pa was employed, and the tangent method was applied to determine σ_y from the corresponding deformation γ vs shear stress σ data. σ_y are plotted versus additive concentration in the mediums ($C_{additive}$), and a typical $\gamma \sim \sigma$ curve is shown as insert in Fig. 5.23. The detailed composition of the pastes are listed in Table 3.3.

The thixotropic agent forms a robust, sample spanning structure due to thermal activation under high shear and high temperature during organic medium preparation [34]. The structure is further reinforced by the added ZnO particles. This network increases the overall viscosity and σ_y, thus avoiding bulk phase separation and guaranteeing long shelf life [69].

On the other hand, ethyl cellulose is molecularly dissolved in Texanol, resulting in a strong increase in viscosity and also introducing weak shear thinning. Compared to a pure polymer solution, the suspension with added ZnO particles has a yield stress and shear thinning properties due to the attractive van der Waals force and/or depletion interaction among particles.σ_y linearly increases with increasing $C_{additive}$ for both sample series. But at a given $C_{additive}$, the Thixatrol Max samples exhibit a higher σ_y than those based on ethyl cellulose (see Fig. 5.23).

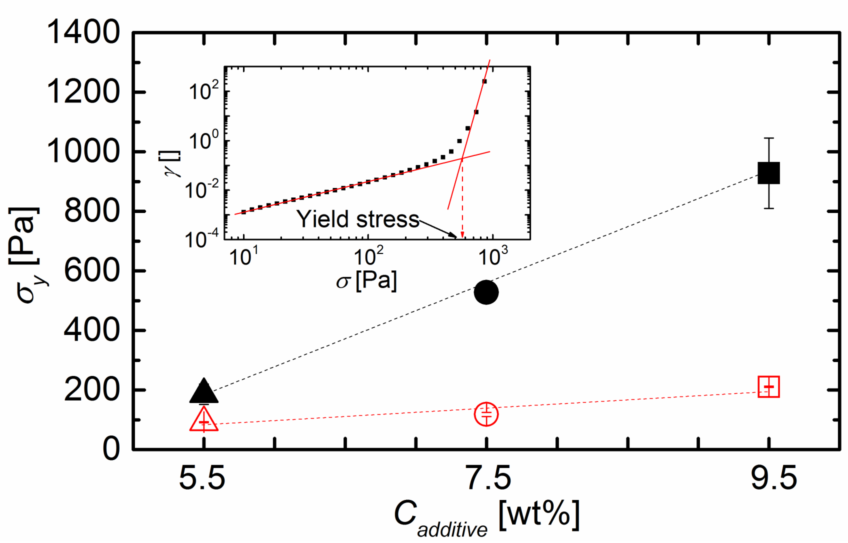

Figure 5.23: Yield stress versus Thixatrol Max (solid points) and ethyl cellulose (open points) concentration (in the prepared medium), respectively. The inserted figure is a typical $\gamma \sim \sigma$ curve for yield stress determination based on the tangent intersection method.

Flow curve

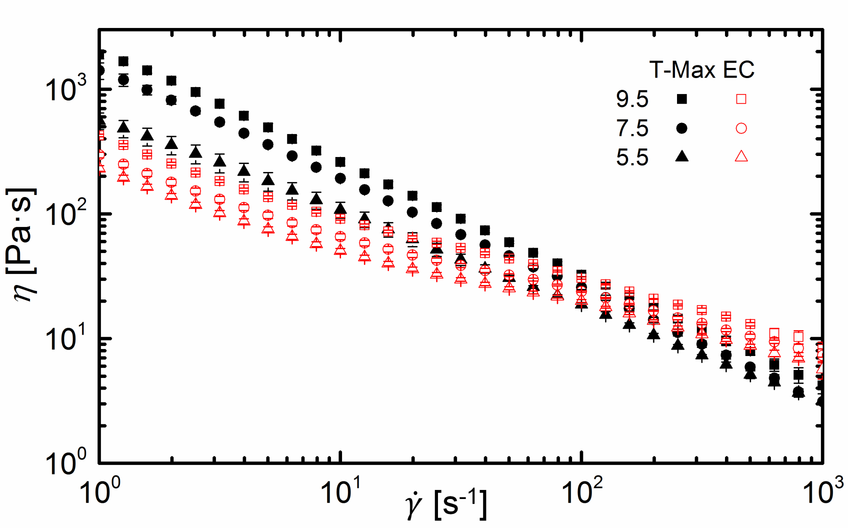

Figure 5.24: Flow curves for six pastes with Thixatrol Max (solid points) and ethyl cellulose (open points) concentrations, respectively.

The viscosity of the six pastes, η, with different types and concentrations of additives was measured between 1 to 1,000 s^{-1}. All pastes show an evident shear thinning characteristics (see Fig.5.24). The degree of the shear thinning can be indicated by the slope of the curves $\eta \sim \dot{\gamma}^{n-1}$ (as listed in Table 5.5). The exponent n is obtained from fitting the above power-law relationship to the experimental data shown in Fig. 5.24. Corresponding values for the six investigated samples are listed in Table 5.5 together with other rheological parameters. The pastes with Thixatrol Max show more pronounced shear thinning ($n < 0.25$) than the pastes with ethyl cellulose ($n \sim 0.50$).

This distinctly different signature of flow curves can be rationalized as follows: the sample spanning network provided by Thixatrol Max results in a high viscosity at the low shear rate but rapidly breaks down under moderate external forces. In contrast, the ethyl cellulose dissolved on a molecular level preserves a high viscosity level even under high shear. The flow curves of the two series cross with each other in the range between 75 to 150 s^{-1}.

Three Intervals Thixotropic Test (3ITT)

Structural and viscosity recovery of the pastes after high shear was characterized using the 3ITT with 1, 500 and 1 s^{-1} for 120, 2 and 360 s. The pastes viscosity gradually recovers after the cessation of the high shear.

This viscosity recovery in the 3rd interval of the test can be described by an exponential equation: $\eta_3(t) = \eta_f + A \cdot exp(-t/\tau)$ (see the inserted figure in Fig. 5.25), where the time constant τ characterizes the recovery rate (see Fig. 5.25). For both additives, the structure recovers faster at higher $C_{additive}$, and generally the recovery is faster for the ethyl cellulose system than for the Thixatrol Max system.

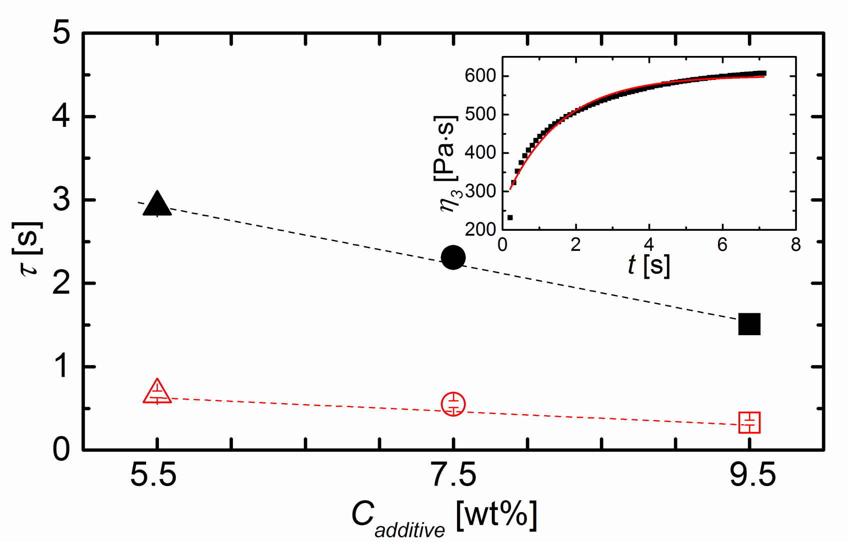

Figure 5.25: Time constant τ versus Thixatrol Max (solid points) and ethyl cellulose (open points) concentration. The inserted figure is a typical viscosity recovery curve after cessation of high shear in the 3rd interval. The red line is the fitted curve using an exponential equation:$\eta_3(t) = \eta_f + A \cdot exp(-t/\tau)$.

Moreover, the 3ITT revealed that the structure irreversible changes during exposure to high shear in the 2nd interval. This effect is characterized by the ratio of the viscosities obtained in the 3rd and 1st intervals. These values are summarized together with other characteristic rheological data in Table 5.5. For both additives, viscosity recovers to a higher extent at lower $C_{additive}$ and generally pastes recovery is more pronounced for the ethyl cellulose system than for the Thixatrol Max system. The damage of the network formed by the thixotropic agent is obviously not completely reversible, at least on a technically relevant time scale ∼ 1 hour. The viscosity in the 2nd interval under 500 s^{-1} is also recorded and values are summarized in Table 5.5.

Finally, it should be mentioned that due to hard- and software constraints of our commercial rheometer, it takes at least 400 ms to reach a steady shear rate in the 3rd interval and this test may not be appropriate to characterize fast printing and spreading processes as will be discussed Section 5.3.2.

Table 5.5: Summary of rheological data of ZnO model pastes

	T-Max 9.5	T-Max 7.5	T-Max 5.5
Yield stress σ_y $[Pa]$	928 ± 118	528 ± 22	186 ± 34
Power-law index n []	0.11 ± 0.03	0.19 ± 0.02	0.23 ± 0.22
Viscosity η_{low} at 1 s^{-1} $[Pa \cdot s]$	1550 ± 80	1017 ± 19	573 ± 24
Viscosity η_{high} at 500 s^{-1} $[Pa \cdot s]$	7.1 ± 0.5	5.3 ± 0.1	4.5 ± 0.3
Ratio of viscosity in 3rd over 1st interval η_f/η_{low} divided by 100	45.0 ± 1.7	48.0 ± 0.5	54.0 ± 4.6
Recovery time constant τ $[s]$	1.51 ± 0.07	2.31 ± 0.09	2.92 ± 0.09
Fracture strain ε []	4.33 ± 0.07	4.41 ± 0.12	5.11 ± 0.07
	EC 9.5	EC 7.5	EC 5.5
Yield stress σ_y $[Pa]$	211 ± 2	118 ± 7	92 ± 2
Power-law index n []	0.46 ± 0.04	0.50 ± 0.03	0.51 ± 0.03
Viscosity η_{low} at 1 s^{-1} $[Pa \cdot s]$	334 ± 3	244 ± 2	161 ± 2
Viscosity η_{high} at 500 s^{-1} $[Pa \cdot s]$	14.8 ± 0.6	12.3 ± 0.2	9.0 ± 0.8
Ratio of viscosity in 3rd over 1st interval η_f/η_{low} divided by 100	62.6 ± 2.7	84.9 ± 1.0	89.9 ± 0.1
Recovery time constant τ $[s]$	0.33 ± 0.03	0.55 ± 0.04	0.67 ± 0.04
Fracture strain ε []	9.03 ± 0.22	8.78 ± 0.30	7.00 ± 0.19

Tack or sticky behavior

The tack or sticky behavior of the pastes was characterized using the oscillatory shear test. All pastes show linear viscoelastic (LVE) region under low shear stress. The storage and loss modulus G' and G" increase with the concentration of the additive in each series (see Fig. 5.26). Due to the limit of the measured shear stress, there is no trend of the cross between G' and G" for the paste with highest concentration of Thixatrol Max. Besides, the pastes, especially those with Thixatrol Max, are not homogeneous under microscopic view. Therefore, the measured data, especially G" data, are with very large variation. At the same additive concentration, the pastes with Thixatrol Max (Fig. 5.26 (a) - (c)) show higher or similar storage modulus but lower or similar loss modulus than those with ethyl cellulose (Fig. 5.26 (d) - (f)). The higher storage modulus in the series of T-Max pastes is the result of the 3D structure formed by the thixotropic agent. While the higher loss modulus in the series of EC pastes is the result of the dissolved ethyl cellulose in the solvent, making the liquid phase more viscous.

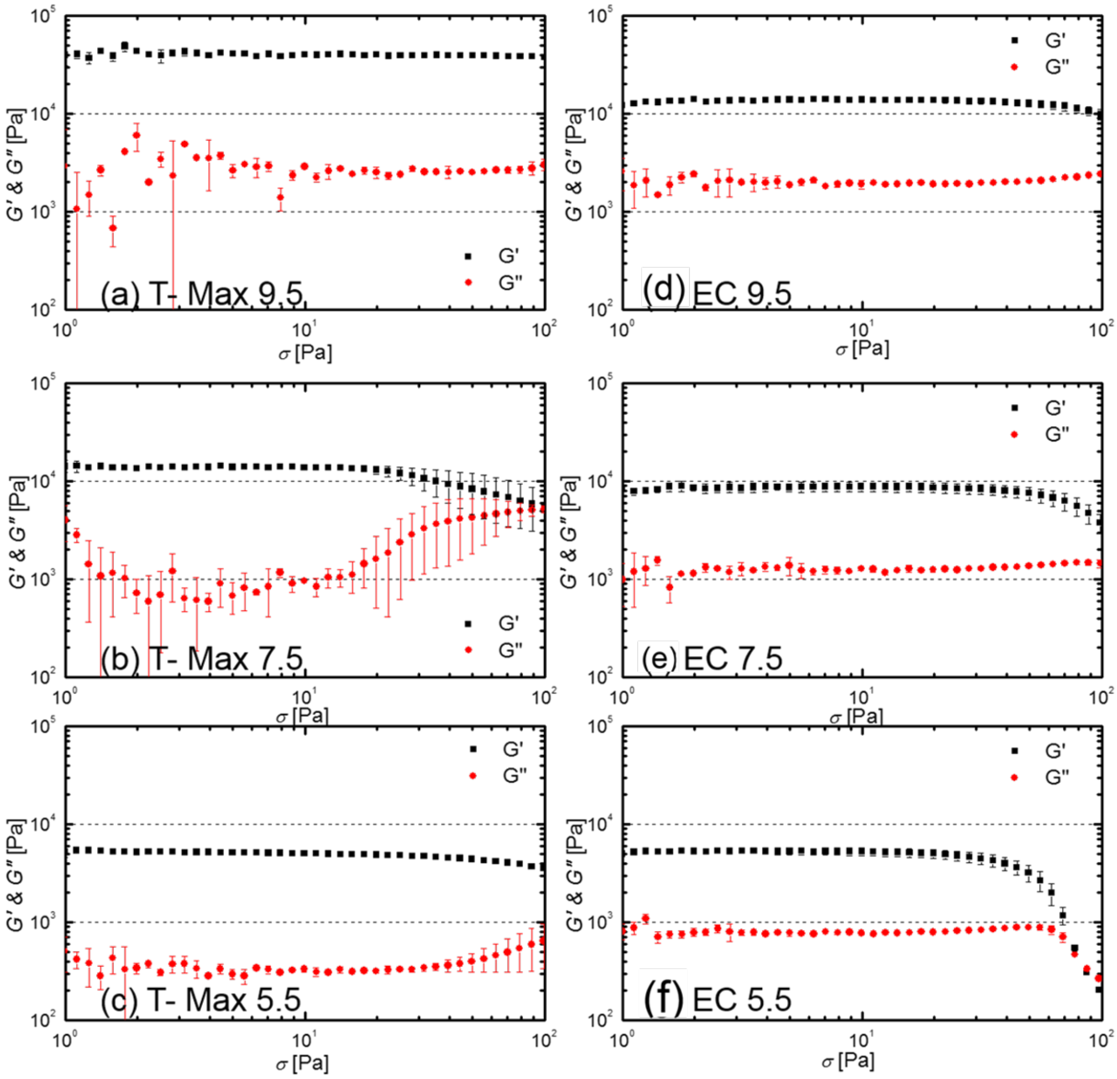

Figure 5.26: Storage and loss modulus of the pastes with different additive concentrations.

The loss factor $\tan\delta$ calculated as $G"/G'$ seems to be independent of the additive concentration but is distinctly higher for the samples modified with ethyl cellulose than for those including T-Max (see Fig. 5.27). The higher loss factor of the pastes containing ethyl cellulose, which is close to the medium range ($\tan\delta \approx 1$), indicate higher tackiness or stickiness compared to the pastes containing Thixatrol Max, due to the increased viscosity of the liquid phase.

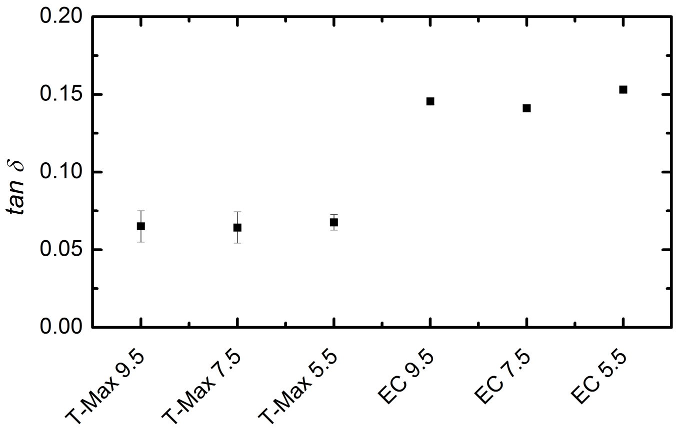

Figure 5.27: Storage and loss modulus of the pastes with different additive concentrations.

Elongational breakup of pastes

The paste stickiness prevents the screen leaving from the substrate after the squeegee has passed. Filament stretching test has been performed to simulate the paste break up at the snap-off point. The stain where break-up or fracture happens ε in this experiments is defined as $\varepsilon = (h_f - h_0)/h_0$, where h_0 is the initial gap, and h_f is the gap at which the filament breaks as observed from the video.

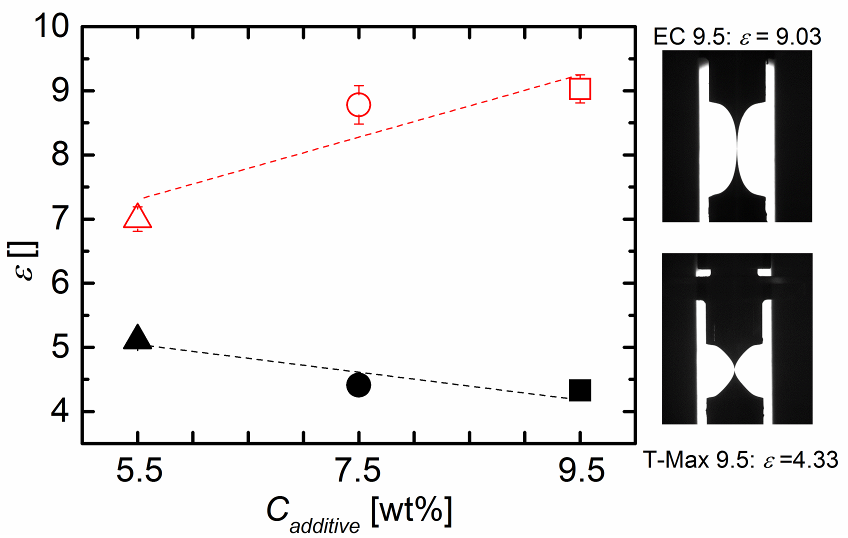

Figure 5.28: Fracture strain ε versus Thixatrol Max (solid points) and ethyl cellulose (open points) concentration, respectively. The inserted figures illustrate the filament break-up for pastes EC 9.5 (upper figure) and T-Max 9.5 (bottom figure), respectively. The initial gap is 1 mm and the displacement speed of the upper plate is 2 mm/s.

The pastes with ethyl cellulose show higher ε than the pastes with the thixotropic agent (see Fig. 5.28). The fracture strain ε increases with C_{EC} but decrease with C_{T-Max}. The dissolved ethyl cellulose increases continuous phase viscosity and paste cohesion thus stabilizing the stretched filament and resulting in a larger ε. This effect increases with increasing C_{EC}. In contrast, the pastes which contain thixotropic agent exhibit weak internal cohesion and brittle failure, receiving their elasticity from a sample spanning network formed due to thermal activation but immediately breaking down upon elongation.

Fig.5.28 exemplarily shows the broken filaments for pastes EC 9.5 and T-Max 9.5, respectively. Obviously, the filament formed with ethyl cellulose paste is more extended, similar to a filament formed with a polymer solution in conventional CaBER tests [45]. In contrast, the pastes including Thixatrol Max break with a neck shape, typically for yield stress fluids [46]. Higher ε for EC formulations than T-Max formulations is expected. However, the variation of ε with $C_{additive}$ is not predictable from $\tan\delta$ but only shows up in filament stretching test. Here ε was determined at a separation speed of 2 mm/s. Absolute values of ε change with separation speed but concentration dependence on different characteristics of EC and T-Max modified pastes remain the same.

5.3.2 High-speed camera video

The high-speed camera video is available as the supplementary materials for the publication in the Journal of Coating Technology and Research (DOI: 10.1007/s11998-018-0091-2).

Pre-injection zone

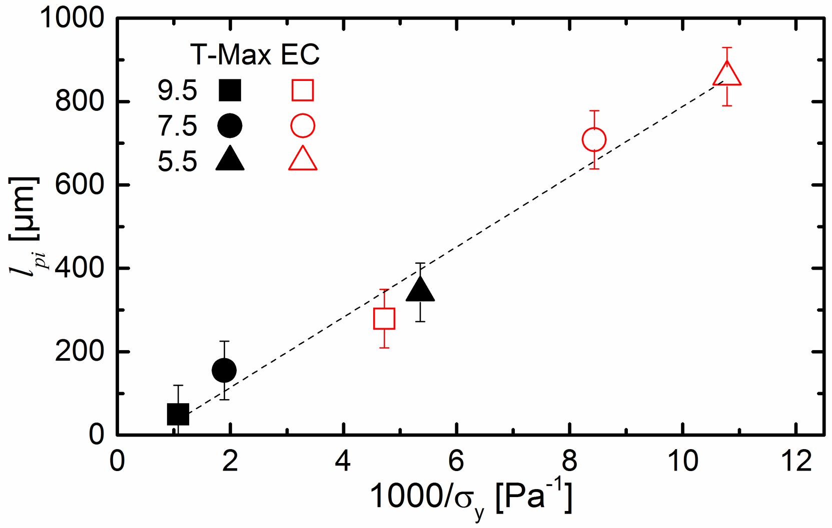

Figure 5.29: Pre-injection length l_{pi} versus the reciprocal of yield stress $1000/\sigma_y$ for six pastes with different concentrations of Thixatrol Max (solid points) and ethyl cellulose (open points). The line indicates the linear relationship between l_{pi} and $1000/\sigma_y$. The error bar is estimated as the half of deformed squeegee width. For paste with T-Max 9.5, the negative value means the paste is pushed on the substrate only precisely under printing squeegee rather than in the paste roll considering the deformation of the squeegee.

The length of the pre-injection zone formed during screen printing was determined from image analysis for all six pastes as described in Section 4.1.6. Obviously, there is a linear relationship between pre-injection length, l_{pi} and the reciprocal of yield stress, $1000/\sigma_y$ (see Fig. 5.29). As mentioned above, the shear stress acting on the paste roll ahead of the printing squeegee has been calculated to decrease reciprocally with the distance to the squeegee assuming Newtonian as well as the shear thinning behavior of the pastes [8, 22, 23].

The paste is squeezed through the screen only when this pressure exceeds σ_y and accordingly l_{pi} increases with $1/\sigma_y$ (in Fig. 5.29 $l_{pi} \sim 1000/\sigma_y$), irrespective of the type and concentration of the rheological additive.

Cling zone

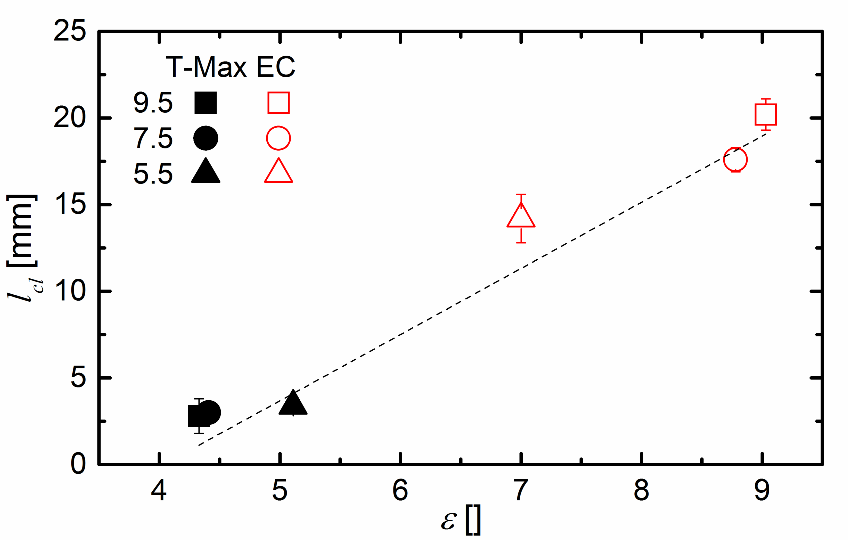

Figure 5.30: Cling zone length l_cl versus fracture strain ε in filament stretching test for six pastes with different concentrations of Thixatrol Max (solid points) and ethyl cellulose (open points). The line indicates the approximately linear relationship between l_{cl} and ε.

As described above, the cling zone length l_{cl} is given by the distance between the nip-contact and the snap-off position and has also been determined from the different pictures in the sequence. The relationship between the cling zone length l_{cl} and fracture strain ε, as obtained from filament stretching experiment is essentially linear irrespective of the type of additive included in the pastes (Fig. 5.30).

l_{cl} increases with C_{EC} but decreases with C_{T-Max}. The pastes including ethyl cellulose exhibit a much longer l_{cl} than the Thixatrol Max modified pastes. The ethyl cellulose polymer dissolved in the continuous phase on a molecular disperse level provides a weak viscoelastic paste behavior with its characteristic internal cohesion and extended stretchability finally holding the screen attached to the substrate for a long time before it snaps off.

On the other hand, the pastes including Thixatrol Max exhibit short breakup length, weak internal cohesion and brittle failure typical for particulate gels, receiving their elasticity from a sample spanning network e. g., of microgel particles

[70]. Such gels fail at low critical deformation and thus release the screen from the substrate easily, hence resulting in a short l_{cl}.

Longer cling zone indicates longer waiting time before snap-off, in which the viscosity increases, resulting higher roughness of the printed features afterwards [8].

Paste spreading

Paste spreading is an important parameter, determining the final geometrical dimensions of a printed pattern. Here, this printing phenomenon is analyzed directly employing high-speed video imaging. Behavior of all six pastes has been investigated at two characteristic positions, namely at the busbar/finger connection area as well as the fine line area.

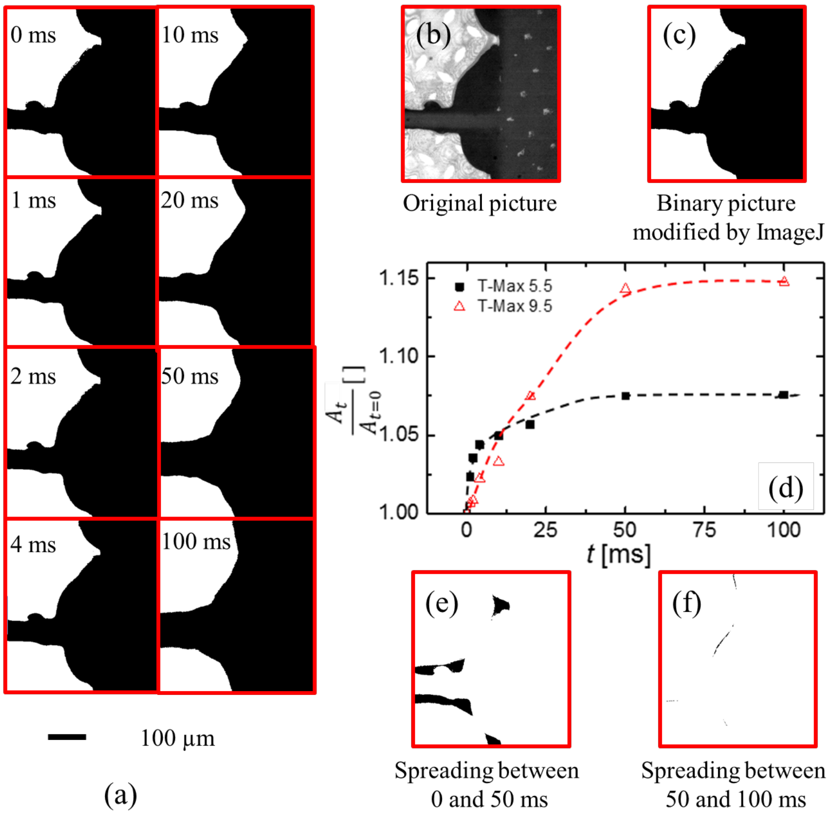

Figure 5.31: Spreading of the paste including 5.5 $wt\%$ Thixatrol Max at the intersection between busbar and fingerline. (a) Image sequence of the observed area (binary pictures). The printing direction is from right to left. Time 0 ms means the squeegee had just passed the observed area. (b) The original image of the observed area at time t = 0 ms used for binarization. (c) The binarized image from the original figure shown in (b). The change in normalized area covered with paste is shown in (d) where $A_{t=0}/A_t$ is plotted versus time. A_t and $A_{t=0}$ refer to the paste covered area at time t and t = 0 ms, respectively. The change of covered area due to spreading can also be seen from the difference between binarized images taken at t= 50 ms and t=0 ms (e) and those taken at t = 100 ms and t = 50 ms (f), respectively.

Exemplarily, spreading of the T-Max 5.5 paste in the busbar/finger connection area is shown in Fig. 5.31. The sequence of binarized images, taken within the first

100 ms after the squeegee had passed the observed area is displayed in Fig. 5.31(a), clearly showing the spreading of the paste. The original images (see Fig. 5.31(b)) are binarized (see Fig. 5.31(c)). The number of black pixels is counted as a measure for the area occupied by the paste. The paste occupied area at time t (A_t) is normalized with occupied area at time t=0 ($A_{t=0}$), where t=0 means that the squeegee had just passed the observed area. The time evolution of this quantity characterizes the spreading kinetics and the data presented in Fig. 5.31(d), clearly demonstrate that paste spreading took place during the first 50 ms and was finished within 50-100 ms. The amount of spreading within the first 50 ms can be directly seen subtracting the binarized images taken at t = 50 ms and t = 0 ms, the black regions visible in Fig. 5.31(e) directly show the wafer area covered due to spreading. Essentially no further increase in silver covered area takes place within the period between t = 50 ms and t = 100 ms, as can be seen when subtracting the corresponding binarized images (Fig. 5.31(f)). Similar results have been obtained for all other pastes investigated here (e.g., T-Max 9.5 in Fig. 5.31(d)), without revealing a clear trend in spreading kinetics depending on type and concentration of additives.

The 3ITT often used to characterize thixotropic and structural recovery of printing pastes is not appropriate for characterization of the screen printing test investigated here. Due to hardware limitation, the first reliable data point in the 3rd interval can be taken not earlier than 400 ms after cessation of high shear. The time constant of recovery, τ, for the pastes investigated here varies between 0.3 and 0.7 s for ethyl cellulose based pastes and between 1.5 and 3 s for the pastes including Thixatrol Max. These long characteristic recovery times accessible with the 3ITT seem not to be relevant for the screen printing process.

On the other hand, no spreading could be observed in the fine finger region within the given range of spatial and temporal resolution of our experimental setup. It seems that the paste stopped moving and the electrode shape was fixed when the squeegee has passed a given position. Finally, it is necessary to mention that some pastes were pushed into the gap between the screen and the substrates. The capillary force may also contribute to paste movement into the gap. After the snap-off process, the paste in the gap was partially brought away (detached) and formed a bleeding area or a fuzzy finger as hypothesized earlier [71].

5.3.3 Printed electrode width estimation

The video image analysis proves that there is no spreading after the printing squeegee has passed in the fine line region. Therefore, the width of the printed electrodes w is determined only in the pre-injection zone.

Six lines are analyzed at different positions on the wafer. ImageJ was used to transfer the original microscopic images to binarized pictures (Fig. 5.32). There are

1600 pixels in the horizontal direction. Therefore, 1600 width data are extracted and averaged from one picture, in total the average width and the standard deviation values discussed below are calculated from 9600 individual data. Due to the periodic change of the screen pattern, the printed electrode width changes correspondingly, resulting in a large standard deviation of width data. However, the average value is still a statistically suitable parameter reflecting the shaded line width on the surface. The average values of the line width data for the 6 pastes are related to rheological properties in the discussion part below.

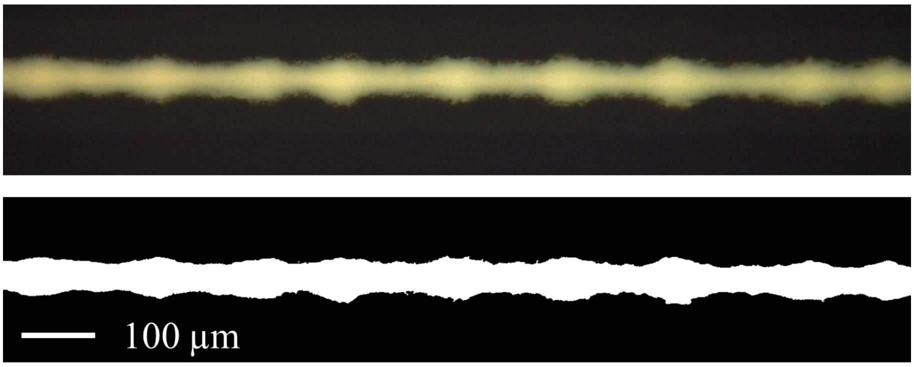

Figure 5.32: The original microscopic (top) and binarized (bottom) images. There are 1600 pixels in the horizontal direction. Therefore, 1600 line width data are collected from one image. The printed electrode width changes due to the influence of the periodic change of the screen mesh.

Higher yield stress σ_y reduces the electrode width w within both series (see Fig. 5.33(a)). The pastes with Thixatrol Max form narrower electrode than the pastes with ethyl cellulose at a given $C_{additive}$. There is, however, no general scaling relating w and σ_y or length of the pre-injection zone l_{pi} valid for both types of additives. Besides σ_y, the higher viscosity at 500 s^{-1} η_{500} is supposed to have an effect on w (see Fig. 5.33(b)). A shear rate of 500 s^{-1} was chosen here because it represents the high shear region mentioned by previous work [32, 33]. For both series, w decreases with increasing η_{500}, i.e., $C_{additive}$. But again, no general correlation between both parameters, holding for both types of rheological control additives is formed. This is not surprising since both additives contribute to the buildup of the σ_y or high η_{500} in a different manner, i.e., based on different physical mechanisms. At a given $C_{additive}$, Thixatrol Max provides a higher σ_y and ethyl cellulose provides a higher η_{500}.

The obtained printed electrodes are always wider than the stencil opening. The paste spreading distance, i.e., electrode width, can be estimated with a simple model: $w \sim \int_0^{t_{pi}} v \; dt$. The v is the paste moving speed under pressure which is inversely proportional to viscosity. t is time under pressure, respectively. t_{pi} is determined by the length of pre-injection zone l_{pi} over printing speed V_{print} ($t_{pi} = l_{pi}/V_{print}$). This simple scaling model outlined above suggests a linear relationship between w

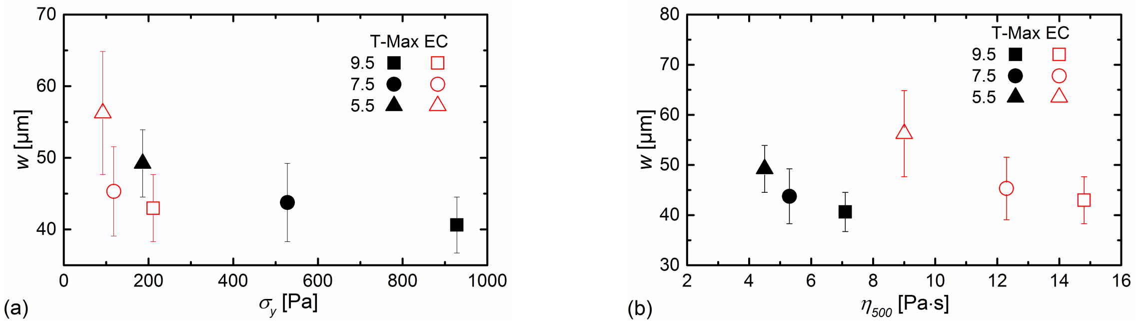

Figure 5.33: Average electrode width w versus yield stress σ_y (a) high shear rate viscosity η at 500 s^{-1} (b) and for six pastes with different concentrations of Thixatrol Max (solid points) and ethyl cellulose (open points).

and $(\sigma_y \cdot \eta_{500})^{-1}$. Replotting the above data accordingly as shown in Fig. 5.34 nicely confirms this crude approximation. Finally, it should be pointed out that both additives contribute to the control of the electrode width based on different physical mechanisms and hence they may be combined in more sophisticated paste recipes to achieve a further reduction of electrode width [53].

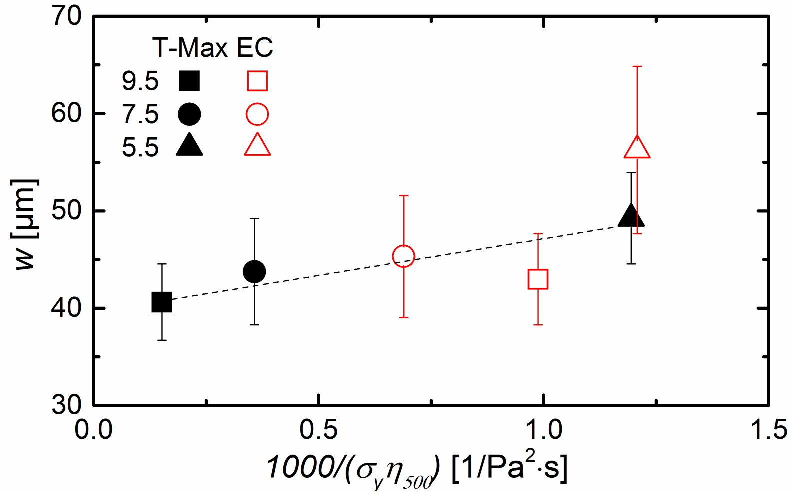

Figure 5.34: Electrode width w versus the reciprocal of product of yield stress and high shear viscosity $1000/(\sigma_y \cdot \eta_{500})$ for six pastes with different concentrations of Thixatrol Max (solid points) and ethyl cellulose (open points). The dashed line corresponds to a linear fit to the experimental data yielding a regression coefficient $R^2 = 0.59$. For comparison: fitting a horizontal line, i.e. assuming that the line width is independent of these rheological data resulted in R^2 =0.15.

Chapter 6

Conclusions

In summary, the first part of this study has shown that the wall slip is beneficial to the fine line screen printing process. The wall slip between the paste and stainless steel network as well as between the paste and capillary film is increased by adding the slip agent in the silver-based screen printable pastes. The slip velocity has been determined using a rotational rheometer equipped with a plate-plate geometry and is independent of the chosen gap size but increases linearly with applied stress.

The pastes have also been printed on mono- and poly-Si wafers. The silver deposit, the residual on the screen, and the busbar/finger connection have been determined using gravimetric and optical methods. The geometry of the printed electrodes has been analyzed using optical microscopy and image analysis. The silver deposit on both types of wafers increased, and correspondingly, the residual silver on the screen decreased with increasing slip velocity. The area of the junction between busbar and finger electrode also strongly decreases with increasing slip.

The theoretical calculation indicates an increase of short-circuit current and fill factor with increased slip velocity due to the change in geometrical parameters. Hence, overall cell efficiency may be controlled by the slip behavior of the wet paste in contact with the printing screen.

Besides, in the second part of this study, ZnO based model pastes with different types (binder and thixotropic agent) and concentrations of rheological additives, have been prepared and their rheological properties have been characterized. The model pastes have been printed on a transparent glass plate and a high-speed camera was used to record the motion of the squeegee, screen and paste. The length of the pre-injection zone, where the paste is pushed through the screen opening, is controlled by the yield stress. Since the stress decreases inversely proportional to the distance from the squeegee, the length over which this stress exceeds the yield stress scales as $l_{pi} \sim 1/\sigma_y$, irrespective of the type of rheological control agent as confirmed by our experimental results. The length of cling zone, where the screen clings to the substrate, increases with paste stickiness, characterized here by the fracture strain determined from filament stretching experiments. A linear relationship $l_{cl} \sim \varepsilon$ is found with the same pre-factor valid for both types of additives.

Paste spreading could be detected at the busbar/finger connection area and turned out to happen very fast within 50 - 100 ms after the squeegee had passed, irrespective of the paste composition. In the fine line area, no significant spreading was detectable with our experimental setup. Accordingly, it is concluded that the width of the electrode is determined in the pre-injection zone.

Chapter 7

Outlook

The effect of wall slip on the fine line screen printing has been proved from the relation between slip velocity and lay down data in the first part of this study. However, no direct observation has been conducted from the side view to judge whether wall slip helps the paste releasing. It is difficult to insert and fix the camera simply between the substrate and screen, considering the distance limit (snap-off distance), which is 1.6 mm in this study. Therefore, the optical path should be carefully designed, changing the direction of the light with mirrors, resulting a reasonable position for installing the camera. With such kind of design, the filament stretching during the snap-off could be investigated with a high-speed camera if sufficient illumination intensity can be provided.

The pre-injection zone, the cling zone and paste spreading have been observed via high-speed camera, based on the model pastes with ZnO. These phenomenon can be different or may even disappear with silver pastes, considering the density differences between silver and ZnO. Therefore, such experiments should be conducted using silver pastes which exhibit very different rheological properties.

For a better understanding of the influence on the rheological properties, the polymer binder (EC 4) and the rheologial modifier (Thixatrol Max) are separated in different series of model pastes. However, in practical formulations, both these two additives contribute to the printing performance. Therefore, future research should consider the interaction between these two additives.

For yield stress fluids, the printing speed could influence the pressure distribution in the paste roll ahead of the squeegee in a non-linear manner. Therefore, its influence on the length of pre-injection zone could be varied accordingly. Filament fracture strain is influenced by the elongational speed. The snap-off distance determines the addition tension to the screen by the downward squeegee action as well as the snap-off speed. The adhesion force between the screen and substrate due to the paste stickiness can be varied by the squeegee pressure. Therefore, variation of the printing parameters and its high-speed camera observation are also topics for further research.

This study focused on the fine line screen printing for front-side metallization of Si solar cells. The pattern is relatively simple compared with the design for other printed devices, e.g. PCB. There are only two cases for the angle between the printed line and printing directions, i.e. 0 and 90 °. In the other designs, this angle can vary, which may influence the spreading phenomena. This is worth for further research regarding fine line screen printing in the other applications.

The substrates used in this study are silicon wafers and window glass. Different substrates are used in different applications, e.g., ceramic for HTCC/LTCC, PET for FPCB, etc. The influence of roughness on fine line screen printing needs a change of printing parameters and paste rheological properties. The spreading of the pastes and/or the phase separation between the solid and liquid phases are affected by the wettability. Therefore, such kind of study is important for fine line screen printing in the other applications. The surface energy of glass can be varied in a wide range in combination with its transparency. The is the ideal substrate for future investigation related to the influence of wetting properties on screen printing performance when lavish adjustment of paste formulation to vary wetting behavior is needed.

Appendix

In this section, the set up of the high-speed camera equipment will be illustrated in details.

Fig. 7.1 shows the picture of high-speed camera set-up. The printing head is kept from the original screen printer. The moving table and optical positioning systems of the screen printer are moved away, leaving the space for the high-speed camera.

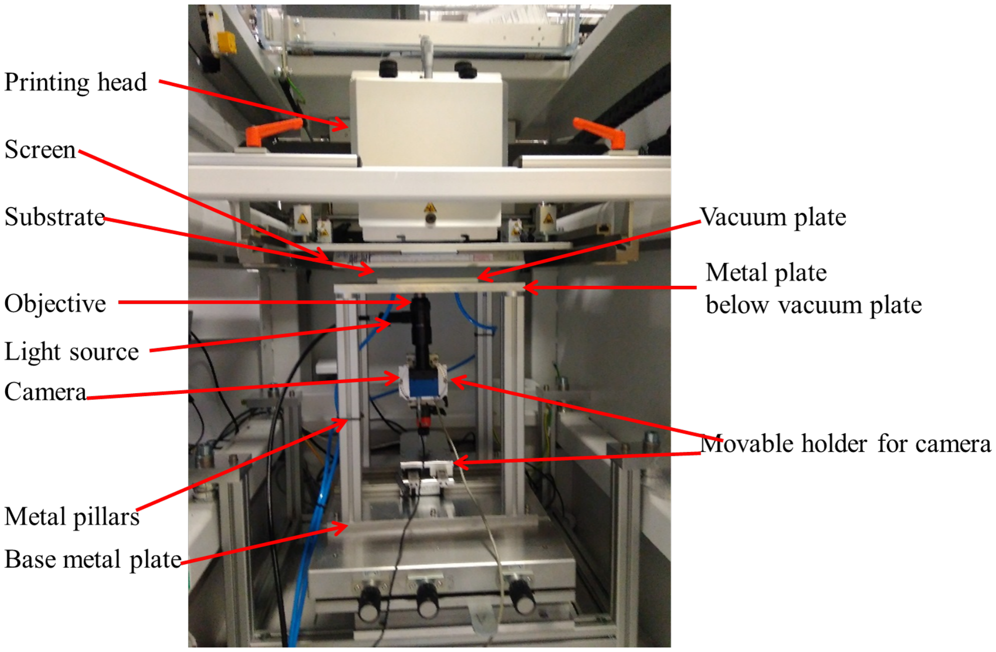

Figure 7.1: High-speed camera set-up.

Fig. 7.2 shows the schematic diagram of the movable table and high-speed camera.

Fig. 7.3 to Fig. 7.6 show the designs of vacuum plate, the metal plate below the vacuum plate, the metal pillar and the base metal plate, respectively, indicated as in Fig. 7.1 and Fig. 7.2.

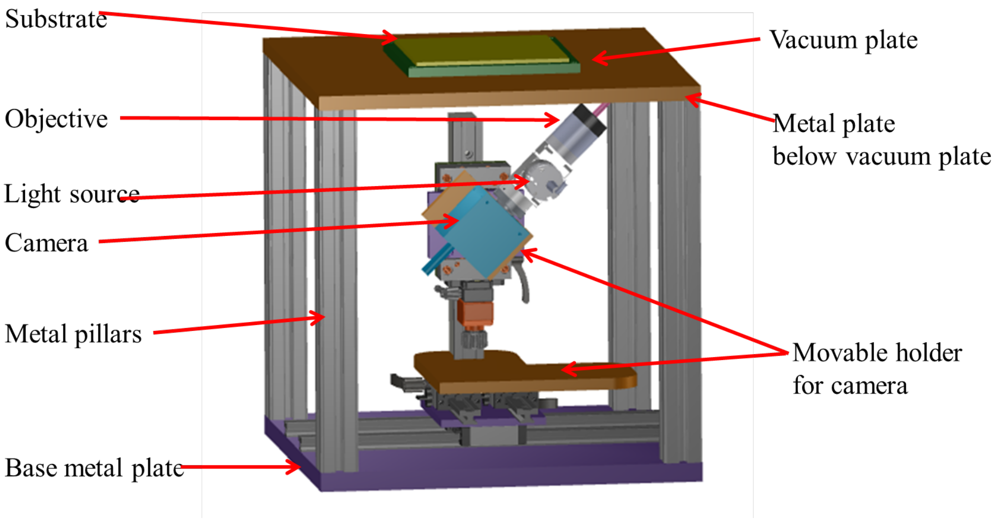

Figure 7.2: 3D schematic diagram of the movable table and high-speed camera.

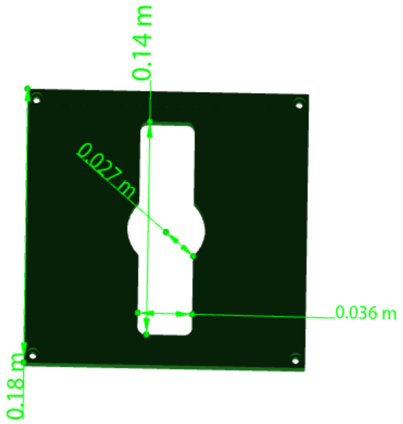

Figure 7.3: The design of vacuum table, which is made of plastic. The thickness is 1 *cm*

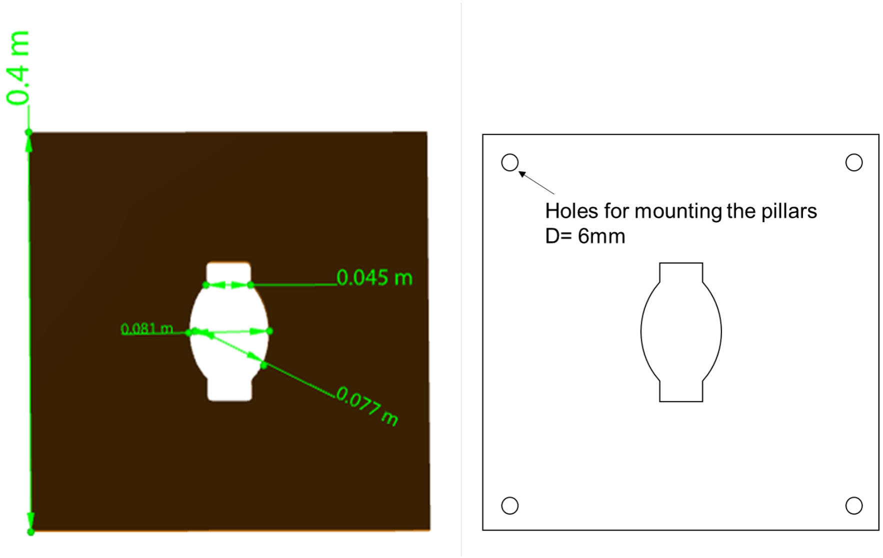

Figure 7.4: The design of metal plate below the vacuum plate. The thickness is 1.5 *cm*

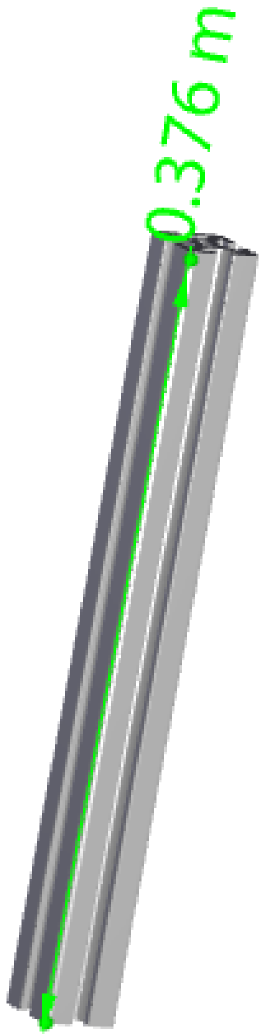

Figure 7.5: The design of metal pillars between the two plates.

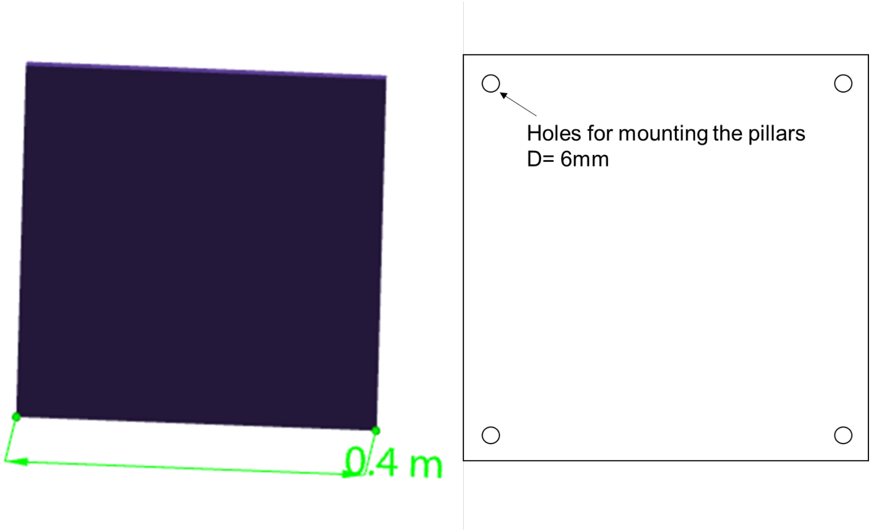

Figure 7.6: The design of metal base plate. The thickness is 1.6 *cm*

List of Figures

List of Tables

References

[1] David Mitzi. *Solution processing of inorganic materials.* John Wiley & Sons, 2008.

[2] Ghaffarzadeh K. Das, R and X. He. Printed, organic & flexible electronics: forecasts, players & opportunities 2017–2027. *Cambridge: IDTechEx*, 2017.

[3] Helmut Kipphan. *Handbook of print media: technologies and production methods.* Springer Science & Business Media, 2001.

[4] Nripan Mathews, Yeng Ming Lam, Subodh G Mhaisalkar, and Andrew C Grimsdale. Printing materials for electronic devices. *International Journal of Materials Research*, 101(2):236–250, 2010.

[5] L Frisson, Ph Lauwers, R Mertens, R Van Overstraeten, and R Govaerts. Screen printed metallization of silicon solar cells. *Active and Passive Electronic Components*, 7(1-3):107–111, 1980.

[6] Dietrich E Riemer. Analytical engineering model of the screen printing process. 1. *Solid State Technology*, 31(8):107–111, 1988.

[7] Dietrich E Riemer. Analytical engineering model of the screen printing process. 2. *Solid State Technology*, 31(9):85–90, 1988.

[8] Dietrich E Riemer. The theoretical fundamentals of the screen printing process. *Microelectronics International*, 6(1):8–17, 1989.

[9] Jaap Hoornstra, Arthur W Weeber, Hugo HC De Moor, and Wim C Sinke. *The importance of paste rheology in improving fine line, thick film screen printing of front side metallization.* Netherlands Energy Research Foundation ECN, 1997.

[10] Michael Neidert, Weiming Zhang, Dong Zhang, and Annette Kipka. Screen-printing simulation study on solar cell front side ag paste. In *Photovoltaic Specialists Conference, 2008. PVSC'08. 33rd IEEE*, pages 1–4. IEEE, 2008.

[11] Monica Schneider, Erin Koos, and Norbert Willenbacher. Highly conductive, printable pastes from capillary suspensions. *Scientific reports*, 6, 2016.

[12] R Durairaj, Lam Wai Man, S Ramesh, Lim Chia Wea, NN Ekere, S Mallik, and A Seman. Investigation of wall-slip behavior in lead-free solder pastes and isotropic conductive adhesives. In *Electronics Packaging Technology Conference, 2009. EPTC'09. 11th*, pages 422–426. IEEE, 2009.

[13] R Durairaj, Lam Wai Man, NN Ekere, and S Mallik. The effect of wall-slip formation on the rheological behaviour of lead-free solder pastes. *Materials & Design*, 31(3):1056–1062, 2010.

[14] Technical information: Kiwomix ra 1750. `http://www.kiwo.de/fileadmin/default/TI_PDF/en/KIWOMIX_RA_1750.pdf`.

[15] Ken Gilleo. Rheology and surface chemistry for screen printing. *Screen Print. Web Httpettrends ComfilespaperuploadsRheology 20and 20Surface 20Chemistry 20for 20Screen 20Print Ing Pdf*, 1989.

[16] Chun-Wen Li, Hui-Chi Chuang, and Sheng-Tun Li. Hedonic analysis for consumer electronics using online product reviews. In *Advanced Applied Informatics (IIAI-AAI), 2016 5th IIAI International Congress on*, pages 609–614. IEEE, 2016.

[17] Tobias Fellmeth, Florian Clement, and Daniel Biro. Analytical modeling of industrial-related silicon solar cells. *IEEE Journal of Photovoltaics*, 4(1):504–513, 2014.

[18] Martin A Green. Solar cells: operating principles, technology, and system applications. 1982.

[19] Minkyu Ju, Youn-Jung Lee, Jonghwan Lee, Bonggi Kim, Kyungyul Ryu, Kyuho Choi, Kyuwan Song, Kyungsoo Lee, Changsoon Han, Youngmi Jo, et al. Double screen printed metallization of crystalline silicon solar cells as low as 30 μm metal line width for mass production. *Solar Energy Materials and Solar Cells*, 100:204–208, 2012.

[20] Dean Buzby and Art Dobie. Fine line screen printing of thick film pastes on silicon solar cells. 2008.

[21] Christopher O Phillips, David G Beynon, Simon M Hamblyn, Glyn R Davies, David T Gethin, and Timothy C Claypole. A study of the abrasion of squeegees used in screen printing and its effect on performance with application in printed electronics. *Coatings*, 4(2):356–379, 2014.

[22] GP Glinski, C Bailey, and KA Pericleous. A non-newtonian computational fluid dynamics study of the stencil printing process. *Proceedings of the Institution*

of Mechanical Engineers, Part C: Journal of Mechanical Engineering Science, 215(4):437–446, 2001.

[23] David J Clements, Marc PY Desmulliez, and Eitan Abraham. The evolution of paste pressure during stencil printing. *Soldering and Surface Mount Technology*, 19(3):9–14, 2007.

[24] Gunnar Schubert, Frank Huster, and Peter Fath. Physical understanding of printed thick-film front contacts of crystalline Si solar cells? Review of existing models and recent developments. *Solar Energy Materials and Solar Cells*, 90(18):3399–3406, 2006.

[25] Sang Hee Lee, Doo Won Lee, and Soo Hong Lee. Review of conductive copper paste for c-Si solar cells. *Korean Journal of Metals and Materials*, 55(9):637–644, 2017.

[26] Z Tehrani, T Korochkina, S Govindarajan, DJ Thomas, J O'Mahony, J Kettle, TC Claypole, and DT Gethin. Ultra-thin flexible screen printed rechargeable polymer battery for wearable electronic applications. *Organic Electronics*, 26:386–394, 2015.

[27] Ivan Švancara, Karel Vytřas, Kurt Kalcher, Alain Walcarius, and Joseph Wang. Carbon paste electrodes in facts, numbers, and notes: A review on the occasion of the 50-years jubilee of carbon paste in electrochemistry and electroanalysis. *Electroanalysis*, 21(1):7–28, 2009.

[28] Howard A Barnes. The yield stress - a review or '$\pi\alpha\nu\tau\alpha$ $\rho\varepsilon\iota$' - everything flows? *Journal of Non-Newtonian Fluid Mechanics*, 81(1):133–178, 1999.

[29] James P Hartnett and Robert YZ Hu. The yield stress - an engineering reality. *Journal of Rheology*, 33(4):671–679, 1989.

[30] Lutz Heymann, Sigrid Peukert, and Nuri Aksel. On the solid-liquid transition of concentrated suspensions in transient shear flow. *Rheologica acta*, 41(4):307–315, 2002.

[31] S Mueller, EW Llewellin, and HM Mader. The rheology of suspensions of solid particles. In *Proceedings of the Royal Society of London A: Mathematical, Physical and Engineering Sciences*, page rspa20090445. The Royal Society, 2009.

[32] Jun Qin, Weijun Zhang, Zhuofeng Liu, and Shuxin Bai. Effects of polymer binder on rheological properties of silver pastes for screen printing front electrode films of solar cells. *International Journal of Modern Physics B*, 29(10n11):1540027, 2015.

[33] Jun Qin, Jun Qin, Shuxin Bai, Shuxin Bai, Weijun Zhang, Weijun Zhang, Zhuofeng Liu, Zhuofeng Liu, Hailiang Wang, and Hailiang Wang. Effects of organic medium on rheological properties of silver pastes for crystalline silicon solar cells. *Circuit World*, 42(2):77–83, 2016.

[34] Inc. Elementis Specialties. *Rheology Handbook: A Practical Guide to Rheological Additives*. 2008.

[35] A. Einstein. Eine neue bestimmung der moleküldimensionen. *Annalen der Physik*, 324(2):289–306, 1906.

[36] Albert Einstein. Berichtigung zu meiner arbeit:Ât'Ât'eine neue bestimmung der moleküldimensionen". *Annalen der Physik*, 339(3):591–592, 1911.

[37] GK Batchelor. The effect of brownian motion on the bulk stress in a suspension of spherical particles. *Journal of fluid mechanics*, 83(1):97–117, 1977.

[38] Irvin M Krieger and Thomas J Dougherty. A mechanism for non-Newtonian flow in suspensions of rigid spheres. *Transactions of the Society of Rheology*, 3(1):137–152, 1959.

[39] D Quemada. Rheology of concentrated disperse systems and minimum energy dissipation principle. *Rheologica Acta*, 16(1):82–94, 1977.

[40] Norbert Willenbacher and Kristina Georgieva. Rheology of disperse systems. *Product design and engineering: Formulation of gels and pastes*, pages 7–49.

[41] R Eisenschitz and F London. Über das verhältnis der van der waalsschen kräfte zu den homöopolaren bindungskräften. *Zeitschrift für Physik*, 60(7-8):491–527, 1930.

[42] Sho Asakura and Fumio Oosawa. Interaction between particles suspended in solutions of macromolecules. *Journal of Polymer Science Part A: Polymer Chemistry*, 33(126):183–192, 1958.

[43] Rita Faddoul, Nadege Reverdy-Bruas, and Joséphine Bourel. Silver content effect on rheological and electrical properties of silver pastes. *Journal of Materials Science: Materials in Electronics*, 23(7):1415–1426, 2012.

[44] R. Rudez, J. Pavlic, and S. Bernik. Preparation and influence of highly concentrated screen-printing inks on the development and characteristics of thick-film varistors. *Journal of the European Ceramic Society*, 35(11):3013–3023, 2015.

[45] Setsuaki Murakami, Kinki Ri, Toshio Itoh, Noriya Izu, Woosuck Shin, Koji Inukai, Yosuke Takahashi, and Yasunori Ando. Effects of ethyl cellulose polymers on rheological properties of (La, Sr)(Ti, Fe)O_3 -terpineol pastes for screen printing. *Ceramics International*, 40(1):1661–1666, 2014.

[46] Koji Inukai, Yosuke Takahashi, Setsuaki Murakami, Kinki Ri, and Woosuck Shin. Molecular weight dependence of ethyl cellulose adsorption behavior on (La, Sr)(Ti, Fe)$O_{\delta-3}$ particles in organic solvent pastes and their printing properties. *Ceramics International*, 40(8):12319–12325, 2014.

[47] M. A. De la Rubia, M. Peiteado, J. F. Fernandez, A. C. Caballero, J. De Frutos, J. Holc, S. Drnovsek, D. Kuscer, S. Macek, and M. Kosec. Processing parameters for ZnO-based thick film varistors obtained by screen printing. *Boletin De La Sociedad Espanola De Ceramica Y Vidrio*, 45(3):154–157, 2006.

[48] M. A. De la Rubia Lopez, M. Peiteado, J. F. Fernandez, A. C. Caballero, J. Holc, S. Drnovsek, D. Kuscer, S. Macek, and M. Kosec. Thick film ZnO based varistors prepared by screen printing. *Journal of the European Ceramic Society*, 26(14):2985–2989, 2006.

[49] M. A. de la Rubia, M. Peiteado, J. de Frutos, F. Rubio-Marcos, J. F. Fernandez, and A. C. Caballero. Improved non-linear behaviour of ZnO-based varistor thick films prepared by tape casting and screen printing. *Journal of the European Ceramic Society*, 27(13-15):3887–3891, 2007.

[50] R. A. Zargar, S. Chackrabarti, S. Joseph, M. S. Khan, R. Husain, and A. K. Hafiz. Synthesis and characterization of screen printed ZnO films for solar cell applications. *Optik*, 126(23):4171–4174, 2015.

[51] HA Barnes and JO Carnali. The vane-in-cup as a novel rheometer geometry for shear thinning and thixotropic materials. *Journal of Rheology*, 34(6):841–866, 1990.

[52] Susanne Elisabeth Wollgarten. Food capillary suspensions. 2015.

[53] Yoko Endo, Ryo Mitta, Takenori Watabe, and Hiroyuki Otsuka. Screen printing plate for solar cell and method for printing solar cell electrode, December 22 2015. US Patent 9,216,607.

[54] C Ballif, DM Huljić, G Willeke, and A Hessler-Wyser. Silver thick-film contacts on highly doped n-type silicon emitters: structural and electronic properties of the interface. *Applied physics letters*, 82(12):1878–1880, 2003.

[55] Jeremy D Fields, Md Imteyaz Ahmad, Vanessa L Pool, Jiafan Yu, Douglas G Van Campen, Philip A Parilla, Michael F Toney, and Maikel FAM Van Hest.

The formation mechanism for printed silver-contacts for silicon solar cells. *Nature communications*, 7, 2016.

[56] Chenhui Xu, Markus Fieß, and Norbert Willenbacher. Impact of wall slip on screen printing of front-side silver pastes for silicon solar cells. *IEEE Journal of Photovoltaics*, 7(1):129–135, 2017. ©2017 IEEE. Reprinted, with permission, from Chenhui Xu, Markus Fieß, and Norbert Willenbacher, Impact of wall slip on screen printing of front-side silver pastes for silicon solar cells, IEEE Journal of Photovoltaics, 2017. Link:https://doi.org/10.1109/JPHOTOV.2016.2626147.

[57] Steven P Meeker, Roger T Bonnecaze, and Michel Cloitre. Slip and flow in soft particle pastes. *Physical Review Letters*, 92(19):198302, 2004.

[58] Steven P Meeker, Roger T Bonnecaze, and Michel Cloitre. Slip and flow in pastes of soft particles: Direct observation and rheology. *Journal of Rheology*, 48(6):1295–1320, 2004.

[59] G Segre. Radial particle displacements in poiseuille flow of suspensions. *Nature*, 189:209–210, 1961.

[60] G Segre and A Silberberg. Behaviour of macroscopic rigid spheres in poiseuille flow part 1. determination of local concentration by statistical analysis of particle passages through crossed light beams. *Journal of fluid mechanics*, 14(1):115–135, 1962.

[61] V Seshadri and SP Sutera. Apparent viscosity of coarse, concentrated suspensions in tube flow. *Transactions of the Society of Rheology*, 14(3):351–373, 1970.

[62] Faezeh Soltani and Ülkü Yilmazer. Slip velocity and slip layer thickness in flow of concentrated suspensions. *Journal of Applied Polymer Science*, 70(3):515–522, 1998.

[63] Jyoti R Seth, Michel Cloitre, and Roger T Bonnecaze. Influence of short-range forces on wall-slip in microgel pastes. *Journal of Rheology*, 52(5):1241–1268, 2008.

[64] Caroline A Schneider, Wayne S Rasband, and Kevin W Eliceiri. Nih image to imagej: 25 years of image analysis. *Nature methods*, 9(7):671–675, 2012.

[65] Johannes Schindelin, Ignacio Arganda-Carreras, Erwin Frise, Verena Kaynig, Mark Longair, Tobias Pietzsch, Stephan Preibisch, Curtis Rueden, Stephan Saalfeld, Benjamin Schmid, et al. Fiji: an open-source platform for biological-image analysis. *Nature methods*, 9(7):676–682, 2012.

[66] A Lorenz, T Strauch, M Demant, T Fellmeth, T Barnes Hofmeister, M Linse, T Dannenberg, J Seiffe, F Clement, D Biro, et al. Impact of texture roughness on the front-side metallization of stencil-printed silicon solar cells. *IEEE Journal of Photovoltaics*, 5(4):1237–1244, 2015.

[67] Ceren Yüce and Norbert Willenbacher. Challenges in rheological characterization of highly concentrated suspensions - a case study for screen-printing silver pastes. *Journal of visualized experiments: JoVE*, (122), 2017.

[68] Chenhui Xu and Norbert Willenbacher. How rheological properties affect fine-line screen printing of pastes: a combined rheological and high-speed video imaging study. *Journal of Coatings Technology and Research*, 15(6):1401–1412, 2018. Reprinted by permission from Springer Nature Customer Service Centre GmbH: Springer Nature, Journal of Coatings Technology and Research, How rheological properties affect fine-line screen printing of pastes: a combined rheological and high-speed video imaging study, Chenhui Xu, Norbert Willenbacher, ©2018. Link: https://doi.org/10.1007/s11998-018-0091-2.

[69] Dirk Sachsenheimer, Bernhard Hochstein, and Norbert Willenbacher. Experimental study on the capillary thinning of entangled polymer solutions. *Rheologica Acta*, 53(9):725–739, 2014.

[70] Ronald G Larson. *The structure and rheology of complex fluids*, volume 150. Oxford university press New York, 1999.

[71] Mari Aoki, Kyotaro Nakamura, Tomihisa Tachibana, Isao Sumita, Hideaki Hayashi, Hideaki Asada, and Yoshio Ohshita. 30μm fine-line printing for solar cells. In *Photovoltaic Specialists Conference (PVSC), 2013 IEEE 39th*, pages 2162–2166. IEEE, 2013.